Grazing Incidence Specular Reflectivity

Theory and Experiment

A. van der Lee [1]
Institute Européen des Membranes / UMR-CNRS 5635
Université de Montpellier II - cc 047
Place E. Bataillon
34095 Montpellier Cedex 5
France

CONTENTS:

Theory - refraction and reflection - Parrat's recursive relation - Born approximation - distorted-wave Born approximation - phase problem - off-specular scattering

Experiment and data analysis - characteristics of reflectivity curves - experiment - modelling

Case studies - growth of silica thin layers - density evolution of hybrid films - *ab-initio* determination of scattering potentials

---

[1] e-mail: avderlee@univ-montp2.fr

Parts of this document have been published in:

- A. van der Lee, *Solid State Sciences* **2** (2000), 257-278 (DOI: 10.1016/S1293-2558(00)00119-9).
- A. van der Lee, *Eur. Phys. J.* B **13** (2000), 755-763 (DOI: 10.1007/s100510050095).
- F. Salah, B. Harzallah, and A. van der Lee *J. Appl. Cryst.* **40** (2007), 813-819 (DOI: 10.1107/S0021889807030403)
- A. van der Lee, F. Salah, and B. Harzallah, *J. Appl. Cryst.* **40** (2007) 820-833 (DOI: 10.1107/S0021889807032207)
- F. Salah, B. Harzallah, T. Mérian, D. Debarnot, A. van der Lee, submitted (2009).

First version: January 2000; updated October 2001, November 2002, April 2007, April 2009

Contents

Chapter 1

Introduction

Materials, whether they are hard or soft, can be characterised by mainly three different categories of techniques: scattering, microscopy and spectroscopy (Fig. 1.1). In addition other techniques such as thermal analysis and magnetic measurements might give valuable information as well. A major difference between scattering techniques on the one hand and microscopy and spectroscopy techniques on the other hand is that especially microscopy is a *local* and *direct* technique, whereas scattering is a *non-local* and *Fourier* technique. Local means that no averaging is done but that local details become available. Direct means that the information gathered can be directly, without ambiguity (apart from experimental uncertainties), calculated from the experimental data. In contrast, a scattering technique gives global, average information that has to be extracted from the experimental data by some kind of inversion procedure. The latter is caused by the fact that the phase of the scattered waves is normally not measured, but only their amplitudes. The divison depicted in Fig. 1.1 is of course not strict, nor are the labels 'local' and 'non-local' or 'direct' and 'Fourier'. The division is useful to show that the three categories of physical techniques yield quite often complementary information, so that the combination of these techniques is more powerful than one technique alone.

Grazing incidence specular reflectivity using X-rays (XR) or neutrons (NR) is - like diffraction and small angle scattering - a scattering technique. The principal objective of an XR or NR experiment is the determination of the one-dimensional scattering potential (SP) perpendicular to the surface of a material. When the material is stratified and its chemical composition is known this information can be related to its chemical profile or atomic structure. Typical parameters that can be deduced from the experiment are the thickness, mass density and interfacial roughness of the individual layers of the stratified medium. The set-up of a reflectivity experiment bears much ressemblence to that of a usual X-ray or neutron diffraction experiment, but usually more attention is paid to the focussing of the beam and the alignment of the goniometer. The principal difference between a reflectivity and a diffraction experiment using monochromatic radiation is that the momentum transfer for the former experiment is typically several orders of magnitude smaller than for the latter experiment in $\Theta/2\Theta$ or Bragg-Brentano geometry. In other words, using for instance Cu-radiation, the Θ range in a reflectivity experiment is typically between 0.0° and about 3.0°, whereas this is for a typical diffraction experiment between 5° and 70°. This is why reflectivity is often called grazing-incidence reflectivity.

Both diffraction and reflectivity are coherent and elastic scattering techniques: there is a definite phase relationship between the impinging and the reflected waves, which have the same energy (wavelength). Due to the different momentum transfer however, the physical reason for eventual constructive or deconstructive interference of the reflected waves

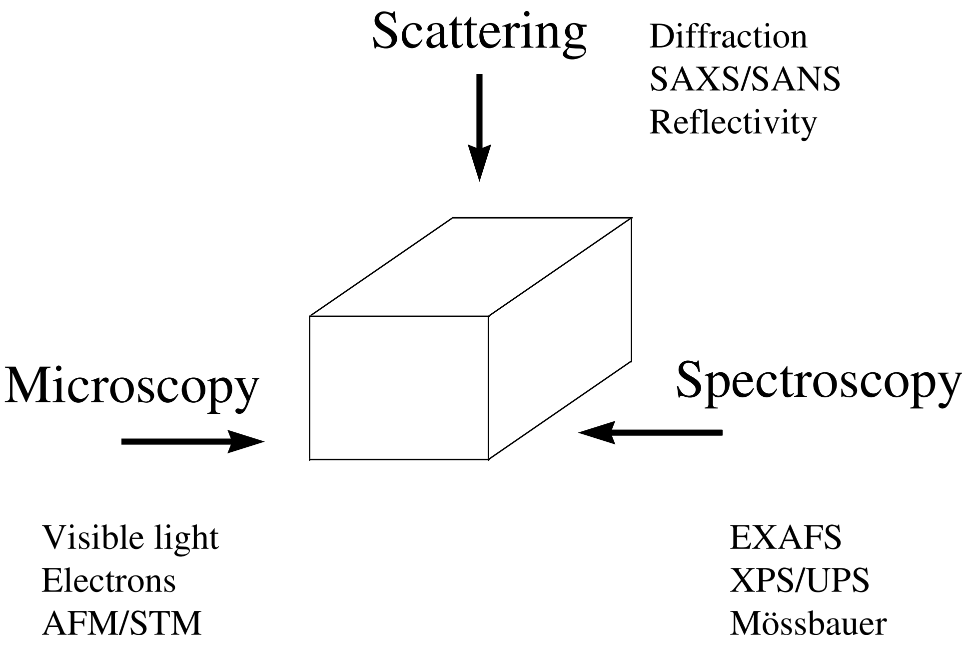

Figure 1.1: Characterisation of soft and hard matter by physical techniques.

is different. For reflectivity a change of the scattering potential (or chemical density) may cause interference, whereas this is for diffraction due to the longe-range (a)periodical order. Reflectivity can be done with liquids or amorphous polymers to extract useful information on the interfaces, whereas diffraction on these materials is much less straightforward. Another important difference between diffraction and grazing incidence reflectivity is that the reference plane for reflection (diffraction) is a physical surface or interface in the case of reflectivity and an atomic lattice plane in the case of diffraction (Fig. 1.2). This lattice plane may be, but is in general not, parallel to a physical surface of the material. The number of lattice planes is in general huge and their orientation with respect to each other is arbitrarily, whereas the interfaces in reflectivity need to be aligned and there number limited. Diffraction thus explores matter in three different directions, but reflectivity only in one direction, the direction perpendicular to the interfaces. Reflectivity can be done with all matter, hard or soft, at the condition that there exists more the less well-defined interfaces. Diffraction is confined to crystalline matter. The differences between diffraction and reflectivity, notably those concerning the long-range order, imply that the reflectivity intensity is continuous, whereas the diffraction signal is discontinuous, *i.e.*, it consists of sharp spots.

The ressemblance between small angle X-ray (neutron) scattering (SAXS and SANS) and XR (NR) is great: both are based on scattering due to density contrast and the scattering angle (defined as the angle between the direct beam and the scatterred beam) is in both cases very small, generally below 3.0° for Cu-radiation. In addition no long-range (a)periodical order is required. Thus the XR (NR) as well as the SAXS (SANS) signals are continuous. The difference is that SAXS (SANS) is due to three-dimensional objects or particles (proteins, aggregates, voids, *etc.*) embedded in an otherwise homogeneous matrix, whereas XR (NR) is due to one-dimensional density contrast. Experimentally, the difference turns out to be a difference between a transmision technique and a reflection technique (Fig. 1.3). It is has to be emphasized that despite the differences between reflectivity on the one hand and small angle scattering and

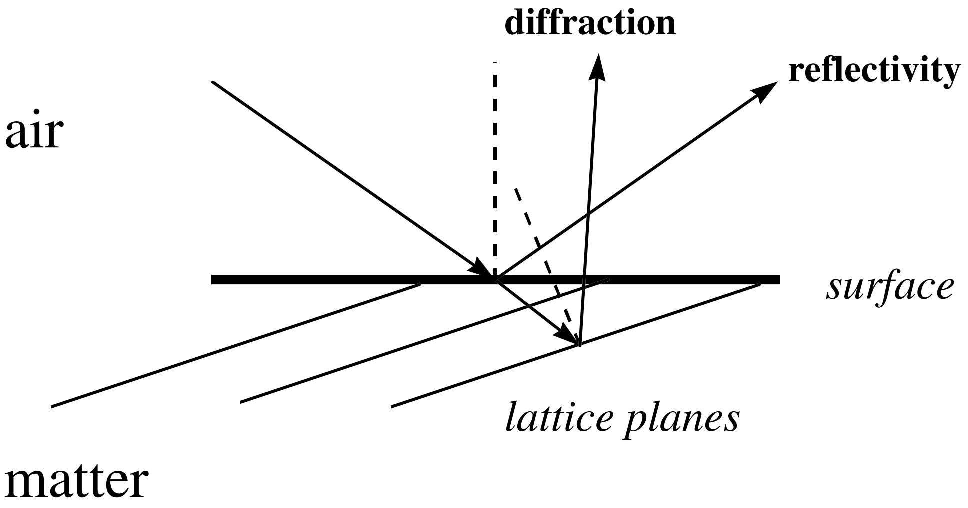

Figure 1.2: Reflectivity *versus* diffraction: surfaces (interfaces) *versus* lattice planes.

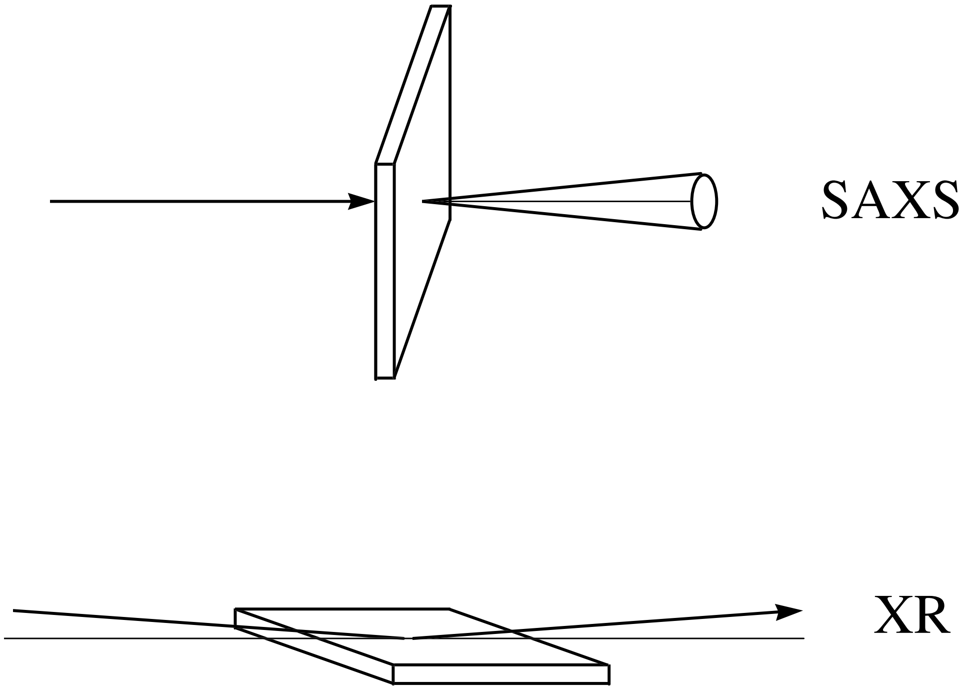

Figure 1.3: Small angle scattering *versus* reflectivity: transmission *versus* reflection .

diffraction on the other hand, the physical origin of these three techniques is of course the same. In all cases there are induced dipole oscillations in the atoms due to the electric field of the incoming wave. Secondary waves are generated that add at large distances (in the far-field approach) to give a scattering amplitude that is detected by a device.

Being mainly developed by physicists, XR and NR become the more and more popular among chemists to explore the surfaces and interfaces of 'soft matter', for instance liquid crystals, microemulsions, proteins, surfactant layers, polymer films, biological membranes, and Langmuir-Blodgett films. Physicists use XR and especially NR to study magnetic profiles of thin films, the reflecting properties of supermirrors or to test advanced theories in inverse quantum scattering or thin film growth.

There exist several review papers that cover either the theory, the experiment or the applications, or a combination of some of these three aspects [1–10]. This work is intended to give a general overview of the technique: the foundations of XR and NR will be reviewed, the set-up of a typical experiment will be discussed, traditional and less-traditional data analysis will be treated, and some of the possibilities of the technique will be given.

Chapter 2

Interaction of electromagnetic waves with matter

When an X-ray beam impinges on a medium it induces, like in the case of diffraction, secondary reradiating dipole centers by the interaction with the individual outer electrons of the atoms that constitute the material. The incoming wave is specularly reflected, *i.e.*, the exit angle θ_e with respect to the reference surface is equal to the impinging angle θ_i ($\theta = \theta_\mathrm{i} = \theta_\mathrm{e}$). This is called the specular condition and it means that the momentum transfer $|q|$ is perpendicular to the reference surface (see Fig. 2.1). Note that this reference surface is the physical surface of the material for reflectivity whereas it is a lattice plane in the case of diffraction. The intensity and phase of the reflected waves as a function of impinging angle depend on the vertical spatial distribution of the electron density in the material. Neutrons interact with the individual atomic nuclei as well as the magnetic induction generated by the spins and orbital motion of the atomic electrons. The intensity and phase of the specularly reflected neutrons waves carry information on the vertical magnetic profile of the material.

In this section the theory underlying specular reflectivity is given. First scattering and refraction are treated to define the majority of symbols of interest for specular reflectivity. The relations connecting the different quantities are given, where appropriate. Next the formula's that exactly describe the reflectance and transmittance of a material are derived. Then two less exact, but useful approaches to reflectivity are treated. Finally the phase problem and non- or off-specular scattering are briefly addressed. It is noted that the symbols that are used throughout this reader can be looked up along with their definitions in the appendix.

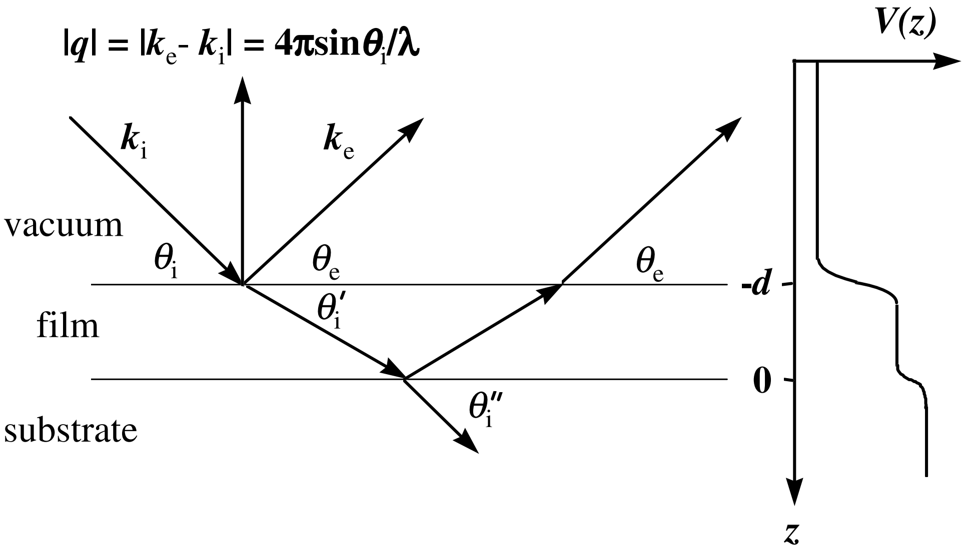

Figure 2.1: Reflectance and transmittance of electromagnetic radiation on a medium with scattering potential $V(z)$. Note that in specular reflectivity using X-rays or neutrons the angles θ_i and θ_e are usually very small, *i.e.*, glancing or grazing.

2.1 Definition of physical quantities relevant to reflectivity

Mathematically, the interaction of the X-ray or neutron beam with the material is governed by the one-dimensional Schrödinger equation:

$$\psi''(k,z) + k^2\psi(k,z) = V(z)\psi(k,z), \tag{2.1}$$

where $\psi(k,z)$ is the wave function for which $k = k_0 \sin\theta = 2\pi \sin\theta/\lambda$ is the vertical component of the $\boldsymbol{k}_i$-vector (Fig. 2.1) and λ the wavelength of the beam; z corresponds to the space coordinate perpendicular to the surface. $V(z)$ is the scattering potential (SP) and is like k^2 expressed in reciprocal square length units, normally nm^{-2}. In reflectivity usually the scattering length density (SLD) $\rho(z)$ is used: $V(z) = 4\pi\rho(z)$. The momentum transfer of the reflectivity process is denoted by q and it is equal to two times the vertical component of the incident wave number ($q = |\mathbf{q}| = 2k = 4\pi\sin\theta/\lambda$). Reflectivity data are collected as a function of momentum transfer q. They are presented likewise (in figures etc.), but quite often k (by theoreticians) or θ (especially in X-ray reflectivity) is taken as the independent variable. The presentation in this reader will switch quite often from k to q and vice versa.

Eq. 2.1 can be rewritten:

$$\psi''(k,z) + k_|^2(z)\psi(k,z) = 0, \tag{2.2}$$

with $k_|^2(z) = k^2 - V(z)$. As usual, a refractive index $n(z)$ can now be defined, which expresses the ratio between the wave number inside the material and the vacuum wave number:

$$n(z) = k_{|}/k = \sqrt{1.0 - V(z)/k^2}. \tag{2.3}$$

It is by the refractive index that the material properties can be defined. It can be derived by calculating the induced field in the material due to the source field. The expression reads for X-ray waves in the nanometer and angström range (this can be found in many textbooks):

$$n(z) = 1.0 - \frac{2\pi r_0}{k_0^2}\rho_\mathrm{n}\sum c_j(Z_j + f_j' - if_j''), \tag{2.4}$$

where ρ_n is the total number density inside the material, *i.e.*, the total number of scattering atoms per unit volume and r_0 is the classical electron radius (Thomson scattering length of the electron): $r_0 = 2.82 \times 10^{-6}$ nm. The sum is over all different elements j inside the material with atomic number Z_j, real dispersion correction f_j' and imaginary dispersion correction f_j''. The coefficient c_j expresses the number of species j in the chemical formula. For instance, in SiO_2, $c_\mathrm{Si} = 1$ and $c_\mathrm{O} = 2$. The sum gives the scattering power of the material, which is in first order proportional (for an material containing only one element) to the number of electrons per atom. The correction factor f_j' is necessary because the electrons are not free but more the less bound to the nucleus, which causes the phase shift beween secondary and primary radiation to deviate from π. Absorption of the primary radiation inside the material is taken into account by the imaginary dispersion factor if_j''. It is related - outside the absorption threshold regions - to the atomic photoabsorption cross section σ_pe by:

$$\sigma_\mathrm{pe} = \frac{4\pi r_0 f''}{k_0}. \tag{2.5}$$

Quite often the photoabsorption cross section *per gram* μ_m (mass attenuation factor) is used: $\mu_\mathrm{m} = N_\mathrm{A}\sigma_\mathrm{pe}/A$, where N_A is the number of Avogadro (= 6.02205×10^{23} mol^{-1}) and A the atomic mass. The linear absorption coefficient μ_l (with usual unity cm$^-$1) is defined in terms of σ_pe and μ_m as follows:

$$\mu_\mathrm{l} = \rho_\mathrm{n}\sum c_j\sigma_{\mathrm{pe},j} = \rho_\mathrm{m}\frac{\sum c_jA_j\mu_{\mathrm{m},j}}{\sum c_jA_j} = \rho_\mathrm{m}\sum x_j\mu_{\mathrm{m},j} = 2\lambda\rho''. \tag{2.6}$$

Here x_j is the mass fraction of species j in the multi-element compound. The physical relevance of the linear absorption coefficient is given by its reciprocal value, *viz.*, the attenuation length, the length after which the intensity is reduced by a factor 1/e. ρ'' is the imaginary part of the scattering length density ρ (see below). For arbitrary l, the intensity reduction is given by $\exp(-\mu_\mathrm{l}l)$. Either σ_pe or the related quantities f_j'', μ_m and μ_l can be found as tabulated values as a function of beam energy for elements and compounds. The mass attenuation μ_m (or absorption) coefficient is sometimes written as $\mu_\mathrm{m} = (\mu_\mathrm{l}/\rho_\mathrm{m})$. Using these definitions, the refractive index n can be expressed in terms of the mass density ρ_m:

$$n(z) = 1.0 - \frac{2\pi r_0}{k_0^2}N_\mathrm{A}\rho_\mathrm{m}\frac{\sum c_j(Z_j + f_j' - if_j'')}{\sum c_jA_j}. \tag{2.7}$$

The refractive index is thus a complex quantity that is quite often formulated as follows:

$$n(z) = 1.0 - \delta + i\beta = 1.0 - \frac{\lambda^2 r_0}{2\pi} N_{\mathrm{A}} \rho_{\mathrm{m}} \frac{\sum c_j (Z_j + f_j')}{\sum c_j A_j} + \frac{i\mu_{\mathrm{l}}\lambda}{4\pi}. \tag{2.8}$$

The relation $\beta = \mu_{\mathrm{l}}\lambda/4\pi$ can be easily derived using the expressions in Eq. 2.5, 2.6 and 2.7. For completeness the relation between the complex dielectric constant $\epsilon = \epsilon' + i\epsilon''$ and δ and β is recalled: $\epsilon' = 1.0 - 2\delta$ and $\epsilon'' = 2\beta$.

From Eq. 2.4 it can be seen - neglecting the dispersion correction factors - that the refractive index can simply be expressed in terms of the electron density ρ_{e}:

$$n(z) = 1.0 - \frac{2\pi r_0}{k_0^2} \rho_{\mathrm{e}}, \tag{2.9}$$

If the notion of electron density is generalized to include the effects of dispersion and absorption, its definition becomes:

$$\rho_{\mathrm{e}} = \rho_{\mathrm{n}} \sum c_j (Z_j + f_j' - i f_j''), \tag{2.10}$$

Finally, the 'material's' definition of n (Eq. 2.9, at zero momentum transfer $k = k_0$) can be connected to the physical definition of n (Eq. 2.3) by:

$$\begin{aligned} n(z) &= \sqrt{1.0 - V(z)/k_0^2} \approx 1.0 - \frac{V(z)}{2k_0^2} = 1.0 - \frac{2\pi r_0}{k_0^2} \rho_{\mathrm{e}} \Rightarrow \\ V &= 4\pi\rho = 4\pi r_0 \rho_{\mathrm{e}}. \end{aligned} \tag{2.11}$$

Thus the scattering length density ρ (unity (length)$^{-2}$) is simply equal to the electron density ρ_{e} (unity (length)$^{-3}$) multiplied by the Thomson scattering length of the electron r_0. The approximation $\sqrt{1-x} = 1 - 1/2x$ holds if $x \ll 1$. This is here the case: x is typically of the order 10^{-4}. Note that the scattering length density ρ, like the generalized electron density ρ_{e} and the scattering potential V, is a complex quantity, the imaginary part including the effects of absorption.

It is emphasized that the function that is directly related to the X-ray reflectivities is the scattering potential $V(z)$, or equivalently, the scattering length density $\rho(z)$, the electron density $\rho_{\mathrm{e}}(z)$, or the refractive index $n(z)$. The mass density $\rho_{\mathrm{m}}(z)$ can only be determined if the chemical composition is known as a function of z.

Looking again at the materials expression for the refractive index (Eq. 2.7) it is seen that it is slightly below unity: $1.0 - n(z) \approx 10^{-5}$ for X-rays. This makes that total external reflection occurs below a certain incident angle, as can be seen from Snell's law:

$$n \cos\theta' = \cos\theta. \tag{2.12}$$

where it is assumed that the interface is between vacuum (index of refraction 1) and a material (index of refraction n). If θ is below a certain critical angle θ_{c} that is defined by:

$$\cos\theta_{\mathrm{c}} = n, \tag{2.13}$$

then total reflection occurs and only an evanescent wave that is exponentionally damped penetrates into the material. This is because the component of the wavevector k' normal to the surface becomes imaginary: $k_z^{'} = k_0 n \sin\theta$. The critical angle θ_{c} can be related to the material properties by the Taylor expansion of the cosine for arguments close to 1.0 ($\cos\theta \approx 1.0 - \frac{\theta^2}{2}$).

$$\theta_{\mathrm{c}}^2 = \frac{4\pi r_0}{k_0^2} N_{\mathrm{A}} |\rho_{\mathrm{m}}| \frac{\sum c_j (Z_j + f_j' - i f_j'')}{\sum c_j A_j} = \frac{4\pi}{k_0^2}|\rho| = \frac{\lambda^2}{\pi}|\rho| = \frac{\lambda^2}{\pi}|\rho_{\mathrm{e}}|. \tag{2.14}$$

Other useful relations are easily derived from Eq. 2.14, such as $q_{\mathrm{c}}^2 = 16\pi|\rho|$ and $k_{\mathrm{c}}^2 = 4\pi|\rho|$.

The direct quantity of interest that is determined by simply measuring the critical angle is the average scattering length density $|\rho|$ but if the chemical composition is known and constant, *e.g.*, for a bulk material, the average mass density $|\rho_{\mathrm{m}}|$ can be determined as well. For (bulk) systems composed of relatively light elements (say with each $Z_j < 16$ and that do not contain a significant number of hydrogens), however, the X-ray critical angle is proportional to the square root of the mass density and becomes composition independent, because for these elements $Z_j \approx A_j/2$ and thus, at fixed wavelength and by neglecting the anomalous dispersion corrections, $\theta_{\mathrm{c}} \propto \sqrt{\rho_{\mathrm{m}}}$. In this case the mass density is related to the critical angle as follows:

$$\rho_{\mathrm{m}} \approx \frac{2\pi\theta_{\mathrm{c}}^2}{\lambda^2 N_{\mathrm{A}} r_0}. \tag{2.15}$$

This is not true anymore for systems containing heavier elements. Typical values for the critical angle are in the range 0.2°-0.6° for X-ray wavelengths around 1.5 Å (thus around that of copper radiation).

The exact penetration depth - defined as the depth (*i.e* distance l perpendicular to the surface) where the intensity is reduced by a factor e - is $\sin\theta/\mu_{\mathrm{l}}$ for angles well beyond the critical angle but can equally well be calculated for incident angles θ below the critical angle θ_{c}:

$$\Lambda = \frac{1}{2k_j''} = \frac{1}{2\mathcal{I}\sqrt{k^2 - V}} \tag{2.16}$$

If $k \ll k_c$ then Λ is equal to $(2k_c)^{-1}$ which is, by use of Eq. 2.14, independent of the wavelength and only dependent on material constants. The formula reads then for a single element bulk material with constant number density ρ_{n}:

$$\Lambda = \left(4\sqrt{r_0 \pi \rho_{\mathrm{n}} Z}\right)^{-1} \tag{2.17}$$

For gold Λ is equal to 12 Å, whereas for a lighter element this is 32 Å. Fig. 2.2 shows the penetration depth for Si (at $\lambda = 0.154$ nm) as a function of angle of incidence θ. Near the critical angle $\theta \approx 0.22^{\mathrm{o}}$ the penetration depth increases drastically from nanometer values to microns. This phenomenon is used in grazing incidence diffraction: by selecting a very small incident angle, only the outermost layers of the material are probed. A weak signal is obtained that is not perturbed by the much more intense signal from the bulk. In this way it can, for example, be determined how a surface reconstructs.

The foregoing formula's are slightly modified in the case of neutrons. The X-ray scattering power $r_0 \sum c_j (Z_j + f_j' - i f_j'')$ is replaced by the neutron scattering power expressed by $\sum c_j b_j$ where b_j the neutron scattering length is, normally expressed in 10^{-13} cm. For neutrons there is no direct relation between the critical angle and the mass density

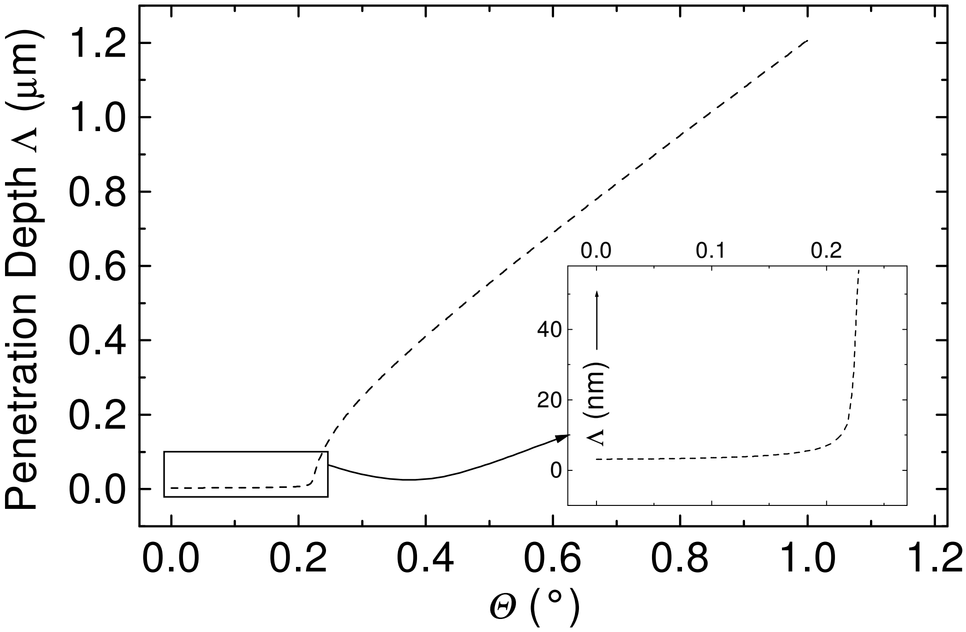

Figure 2.2: Penetration depth of an X-ray beam with wavelength $\lambda = 0.154$ nm as a function of angle of incidence θ for Si.

(as in Eq. 2.15) if the composition is not known.

As an example we can calculate using these formula's the strength of the scattering potential for a homogeneous Si ($Z_{\rm Si} = 14$, $A_{\rm Si} = 28$, $b_{\rm Si} = 4.15 \times 10^{-13}$ cm substrate with density $\rho_{\rm m} = 2.33$ gcm^{-3}. The formula for the X-ray and neutron case are, respectively (neglecting the dispersion corrections):

$$V = 4\pi r_0 \rho_{\rm e} = 4\pi r_0 \rho_{\rm m} N_A Z_{\rm Si}/A_{\rm Si} = 0.0248 {\rm nm}^{-2}, \tag{2.18}$$

$$V = 4\pi b \rho_{\rm n} = 4\pi \rho_{\rm m} N_A b_{\rm Si}/A_{\rm Si} = 0.00260 {\rm nm}^{-2}. \tag{2.19}$$

It is seen that the SP for X-rays is nearly ten times larger than that for neutrons. This means that the critical angle for total reflection for neutrons is shifted towards lower angles compared to that for X-rays. This is a general trend. The neutron SP is in general much smaller than the X-ray SP for the same chemical system. Neutron scattering lengths can even be negative, for instance for hydrogen, manganese, and titanium, such that for quite a lot of systems there does not even exist a critical angle for total external reflection.

Neutron scattering lengths are quite variable throughout the periodic system, whereas for X-rays the scattering power steadily increases with increasing atomic number. An exception must be made for X-ray scattering powers close to the absorption edges of the elements. There the dispersion correction f' can be so important that even the X-ray scattering power becomes negative. The change of the scattering power with wavelength can be used as a powerful tool to determine SP's with less ambiguity than usual (see section 3.3.4). Similarly, in the case of neutrons, isotopic labeling, by for instance deuterium that has a quite large positive scattering length, can be used to characterize with precision the density profiles across interfaces.

information	web address
neutron scattering lengths (ATI)	http://www.ati.ac.at/∼neutropt/scattering/table.html
neutron scattering lengths (NIST)	http://www.ncnr.nist.gov/resources/n-lengths/
atomic (X-ray) scattering factors	http://henke.lbl.gov/optical_constants/
SLD calculator (neutrons, X-rays)	http://www.ncnr.nist.gov/resources/sldcalc.html
X-ray absorption	http://www.ncnr.nist.gov/programs/crystallography/mucalc.html
neutrons: (in)coherent, absorption	http://www.ncnr.nist.gov/programs/crystallography/neutron.html
physical reference data	http://physics.nist.gov/PhysRefData/
DABAX: Data base for X-rays	http://www.esrf.eu/computing/scientific/xop2.1/function.html
specular reflectivity calculations etc.	http://sergey.gmca.aps.anl.gov/TER_sl.html
non-specular reflectivity calculations	http://sergey.gmca.aps.anl.gov/TRDS_sl.html
neutron scattering information links	http://www.neutron.anl.gov/
synchrotron and neutron facilities	http://ww1.iucr.org/cww-top/rad.index.html
periodic table of elements	http://www.webelements.com/index.html

Table 2.1: WWW ressources for X-ray and neutron related scattering information

There are several useful ressources on the World Wide Web for finding information on scattering factors, neutron scattering lengths, photoabsorption cross sections and so on for all elements (Table 2.1). The Table also contains addresses where *in-situ* reflectance and transmittance calculations can be done as well as calculations of the penetration depth and refractive index for compound materials and other useful sources of information.

2.2 Mathematical description of reflectivity

The exact derivation of the transmission and reflection coefficients follows nearly exactly the lines developed in optics. The Fresnel formula (section 2.2.1) is valid for any wavelength from the visible to the X-ray range. It is because of the near to one coincidence of the refractive index of materials for wavelengths in the nanometer and ångstrom range that X-ray and neutron reflectivity are very different from visible light reflectivity. The Fresnel formula and Parrat's recursive relations (section 2.2.2) are exact for homogeneous stratified media, *i.e.*, they give exact solutions to the wave equations. The Fresnel formula is easy to handle, but holds only for a material with a constant scattering potential. Parrat's recursive relations hold for a general SP, but are quite difficult to be used if the SP become too complex. They are, however, together with the formula's derived from the Born approximation for scattering, the basis of nearly all modern fitting techniques that try to modelise the SP from experimental specular reflectivity data.

2.2.1 The Fresnel formula

Consider a plane wave $\psi(z) = \exp(ikz)$ with unit amplitude, incident from air onto the medium with constant SP V_s and corresponding refractive index n_s and wave number $k = 2\pi\sin\theta/\lambda$ (Fig. 2.3). The interface between air and medium is at $z = 0$, and z is positive inwards the material. There will be a transmitted wave with amplitude T travelling in the same direction as the incident wave: this wave is characterized by the wave function $\psi(z) = T\exp(in_\mathrm{s}kz) = T\exp(ik_\mathrm{s}z)$. There is also a specularly reflected wave with amplitude R travelling in the opposite direction as the incident wave characterized by the wave function $\psi(z) = R\exp(-ikz)$. The wave number k_s inside the medium is according to Eq.

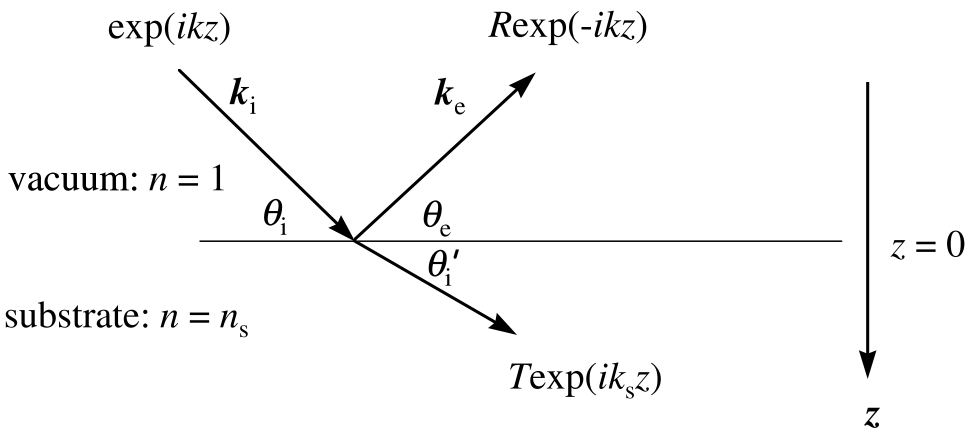

Figure 2.3: Reflectance and transmittance of electromagnetic radiation on a substrate.

2.3 equal to:

$$k_\mathrm{s} = n_\mathrm{s} k_0 \sin\theta'. \tag{2.20}$$

Using Snell's law

$$\sin\theta' = \sqrt{\sin^2\theta - (1-n_\mathrm{s})^2/n_\mathrm{s}^2}, \tag{2.21}$$

Eq. 2.20 becomes

$$k_\mathrm{s} = \sqrt{k_0^2\sin^2\theta - k_0^2(1-n_\mathrm{s})^2} = \sqrt{k^2 - V}. \tag{2.22}$$

T is the transmission coefficient or transmittance and R is the reflection coefficient or reflectance. The wave equations to be solved are (see Eq. 2.2):

$$\psi''(z) + k^2\psi(z) = 0, \quad z \le 0 \quad \text{in air,} \tag{2.23}$$

$$\psi''(z) + k_\mathrm{s}^2\psi(z) = 0, \quad z \ge 0 \quad \text{in medium,} \tag{2.24}$$

subject to the boundary conditions at the interface $z = Z = 0$:

$$\psi(Z^+) = \psi(Z^-), \tag{2.25}$$

$$\psi'(Z^+) = \psi'(Z^-), \tag{2.26}$$

where (Z^+) indicates the positive side and (Z^-) the negative side of the interface at $z = Z$. The two boundary conditions reflect the continuity of the parallel magnetic and electric field components across the interface. The general solutions of the wave equations are thus:

$$\psi(z) = \exp(ikz) + R\exp(-ikz), \quad z \leq 0 \text{ in air}, \tag{2.27}$$

$$\psi(z) = T\exp(ik_s z), \quad z \geq 0 \text{ in medium}, \tag{2.28}$$

Using the boundary conditions (Eq. 2.25) it is readily found that:

$$1 + R = T, \tag{2.29}$$

$$k(1-R) = k_s T, \tag{2.30}$$

This set of equations with two unknowns can be solved to give:

$$R = \frac{k - k_s}{k + k_s}, \tag{2.31}$$

$$T = \frac{2k}{k + k_s}. \tag{2.32}$$

The expression for the reflectivity becomes by dividing through k_0:

$$R = \frac{\sin\theta - n_s \sin\theta'}{\sin\theta + n_s \sin\theta'}. \tag{2.33}$$

For incident wave numbers k smaller than the critical wave number $k_c = \sqrt{V_s}$ the wave number inside the medium k_s becomes imaginary (Eq. 2.22), and the reflectance and transmittance become complex quantities. Normally only the squared modulus of the reflectance $|R|^2$ can be measured in a reflectivity experiment. Eq. 2.31 can be rewritten in terms of the reduced wave vector $\kappa = k/k_c$:

$$R = \frac{\kappa - \sqrt{\kappa^2 - 1}}{\kappa + \sqrt{\kappa^2 - 1}} = \frac{1 - \sqrt{1 - \kappa^{-2}}}{1 + \sqrt{1 - \kappa^{-2}}}. \tag{2.34}$$

Using the Taylor expansion of the square root in the vicinity of $x = 0$ ($\sqrt{1-x} \approx 1 - x/2$) it is found that $|R|^2$ falls rapidly off with $(k_c/2k)^4$ for large k. It can equally well be proved that for $k < k_c$ $|R|^2 = 1$. The exact behaviour of the reflectance will be considered in section 3.1.

It is noted that the reflectance and transmittance given in Eq. 2.31 are strictly speaking only valid for s-polarisation, *i.e.*, the electric field **E** of the incoming X-rays perpendicular to the plane of incidence. It can be shown, however, that Eq. 2.31, is also valid to a high degree of accuracy for p-polarisation (*i.e.*, the electric field **E** of the incoming X-rays parallel to the plane of incidence) for very low angles [5]. For higher angles, one should take into account the effects of polarization as is done in, *e.g.*, diffraction and ellipsometry. In this case an average value of the proper expressions for s- and p-polarisation should be taken if unpolarized X-rays are used (which is normally the case.

2.2.2 Parrat's recursive relation

The concepts in the foregoing section may be used to derive the exact formula to describe the reflectivity (and transmission) from a single layer on a substrate, two different layers on a substrate, or more general a multilayer on a substrate.

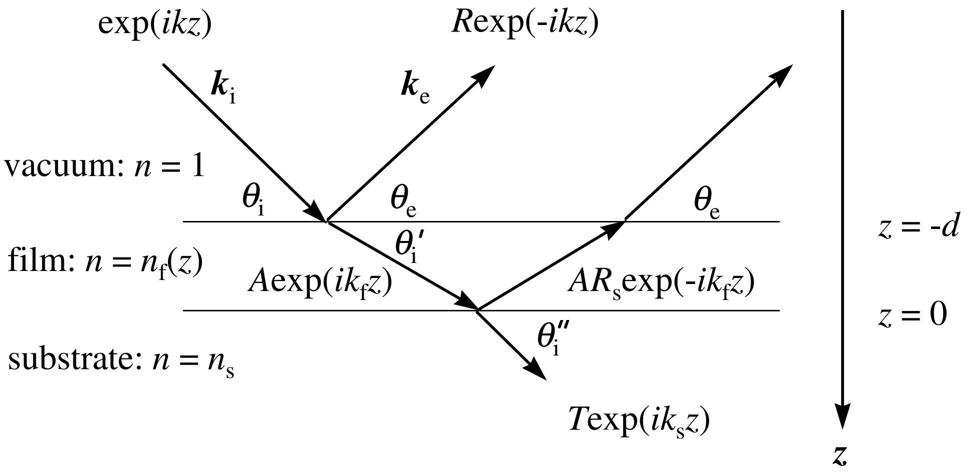

Figure 2.4: Reflectance and transmittance of electromagnetic radiation on a substrate plus single layer with homogeneous scattering length density.

If the thickness of the individual layers becomes infinitesimal small, the reflectivity from a general SP profile can be calculated by iteratively applying the following formula's. For X-rays the general case was first formulated by Parrat [11].

First we derive the reflectance of a single layer on a substrate (Fig. 2.4). The definitions are similar as in the foregoing section: the substrate surface is at $z = 0$ and the film surface (interface film/air) at $z = -d$. There are now three different wave equations:

$$\psi''(z) + k^2\psi(z) = 0, \quad z \leq -d \quad \text{in air,} \tag{2.35}$$

$$\psi''(z) + k_\mathrm{f}^2\psi(z) = 0, \quad -d \leq z \leq 0 \quad \text{in film,} \tag{2.36}$$

$$\psi''(z) + k_\mathrm{s}^2\psi(z) = 0, \quad z \geq 0 \quad \text{in substrate.} \tag{2.37}$$

The solutions of these equations can be written as:

$$\psi(z) = \exp(ikz) + R\exp(-ikz), \quad z \leq -d \quad \text{in air,} \tag{2.38}$$

$$\psi(z) = A[\exp(ik_\mathrm{f}z) + R_\mathrm{s}\exp(-ik_\mathrm{f}z)], \quad -d \leq z \leq 0 \quad \text{in film,} \tag{2.39}$$

$$\psi(z) = T\exp(ik_\mathrm{s}z), \quad z \geq 0 \quad \text{in substrate,} \tag{2.40}$$

where k_s is as defined before (Eq. 2.20), and

$$k_\mathrm{f} = \sqrt{k^2 - V_\mathrm{f}}. \tag{2.41}$$

The amplitudes R (the reflectance to be looked after), A, R_s, and T (the transmittance) are to be determined by applying the boundary conditions (Eq. 2.25) to the two interfaces at $z = -d$ and $z = 0$, respectively. Only the expression for the

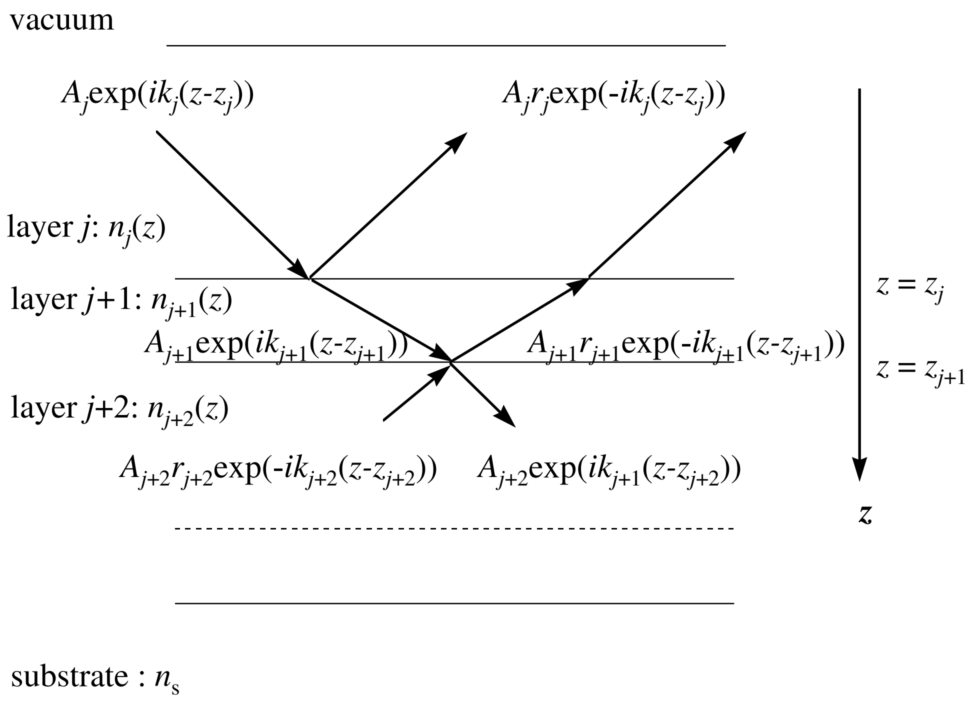

Figure 2.5: Reflectance and transmittance of electromagnetic radiation through a single layer within a stack of N layers.

reflectance, the only physical quantity of experimental interest, will be given here:

$$R = \frac{R_\text{f} + R_\text{s}e^{2ik_\text{f}d}}{1 + R_\text{f}R_\text{s}e^{2ik_\text{f}d}}e^{-2ikd}, \tag{2.42}$$

where R_s and R_f can be considered as the Fresnel reflectances for the substrate and the film, respectively (*cf.* Eq. 2.31):

$$R_\text{s} = \tfrac{k_\text{f}-k_\text{s}}{k_\text{f}+k_\text{s}}, \tag{2.43}$$
$$R_\text{f} = \tfrac{k-k_\text{f}}{k+k_\text{f}}. \tag{2.44}$$

Having developed the machinery for the bare substrate and for a single layer on a substrate it is not difficult anymore to derive the equation for a general multilayer of N uniform layers stacked along the z-axis with individual layers of thickness Δz_j and wave numbers $k_j = \sqrt{k^2 - V_j}$ with constant SP V_j. The interface between layer j and layer $j+1$ is at $z = z_j$. The wave functions in layer $(j+1)$ are now (Fig. 2.5):

$$\psi_{j+1}(z) = A_{j+1}\big[\exp(ik_{j+1}(z - z_{j+1}) + r_{j+1}\exp(-ik_{j+1}(z - z_{j+1})\big], \tag{2.45}$$
$$\psi'_{j+1}(z) = ik_{j+1}A_{j+1}\big[\exp(ik_{j+1}(z - z_{j+1}) - r_{j+1}\exp(-ik_{j+1}(z - z_{j+1})\big]. \tag{2.46}$$

Applying again the boundary condition at $z = z_j$ it is found that:

$$R_j = \frac{F_{j+1} + R_{j+1} e^{2ik_{j+1}\Delta z_{j+1}}}{1 + F_{j+1} R_{j+1} e^{2ik_{j+1}\Delta z_{j+1}}}, \tag{2.47}$$

where the F_j are the Fresnel coefficients for each individual layer j defined in a similar way as Eq. 2.43. If the k_j and Δz_j are given for $j = 1, 2, 3, ..., N$, R_j can be calculated for all j by starting at the layer adjacent to the substrate $j = N$. Note that in the first step ($j = N$) $R_{N+1} \equiv 0$ since there is only transmittance within in the substrate. Thus $R_N = F_{N+1} = (k_N - k_s)/(k_N + k_s)$, the Fresnel reflectance of the substrate. The reflectance of the complete system is given by R_0. The reflectance R in this particular coordinate system, *i.e.*, with the substrate/film interface located at $z = 0$ is obtained by writing the wave in air as:

$$\psi(z) = \exp(ikz) + R\exp(-ikz), \qquad z \leq -d \quad \text{in air}, \tag{2.48}$$

and equating this to the wave function in layer 0 at $z_0 = -d$ (see Eq. 2.45). It is obtained that

$$R = R_0 \exp(-2ik_0 d). \tag{2.49}$$

The reflectivity r (the quantity that is measured) is then given by the squared modulus $|R|^2$. If the substrate/film interface is given to be located at $z = d$, then Eq. 2.49 simplifies to $R = R_0$, but the final reflectivity remains, ofcourse, the same. In other words, the reflectivity is not affected by a change of the origin, but the reflectance is. 2.47 is called Parrat's recursive relation, since in order to calculate the final reflectance it has to be applied recursively.

The solution Eq. 2.47 is not valid whenever $k_{j+1} = 0$. This happens when the free wave vector k is equal to the critical wavevector of layer $(j + 1)$: $k = \sqrt{V_{j+1}}$. It can be shown that the denominator in Eq. 2.47 becomes zero. The reflectance R_i for this case can be found by solving the wave equations for the wave functions in Eq. gensolutionsparratN with $k_{j+1} = 0$. It is found that $R_i = 1$.

For an arbitrary SP Δz_{j+1} has to go to zero in order to describe the most general profile, and N, the number of stacks goes to infinity. In practice, however, the finite resolution of the experiments puts an upper limit on the number of stacks that can be taken. The sampling theorem in fact imposes that no structural features can be resolved which are larger than $1/(4k_{\max})$ where $k_{\max}$ is the maximum wave number up to which the experimental data have been collected. So this value puts a lower limit on the thickness of an individual layer and un upper limit on the number of stacks that has to be taken to analyze the data.

2.2.3 The Born approximation for reflectivity

Although Parrat's recursive relation (Eq. 2.47) is an exact formula to calculate the reflectivity of a general SP, it is quite cumbersome to use. In addition, there is no apparent way how to invert this recursive formula. That is to say, if the complex reflection coefficient R is known, Eq. 2.47 cannot be used to derive the SP, *i.e.*, the set of values $\{\Delta z_j, k_j\}$. This is of course the very intention of the reflectivity experiment: the determination of the SP. In practice however, Eq. 2.47 is routinely used to fit the experimental data if it is presumed that the SP is not too complicated, *e.g.*, in the case of a single or double layer on a substrate. Then starting parameters for $\{\Delta z_j, k_j, j = 1, 2, V_s\}$ (and roughness parameters as is shown later) are guessed and the reflectivity is calculated by Eq. 2.47 as a function of the wave number k. The

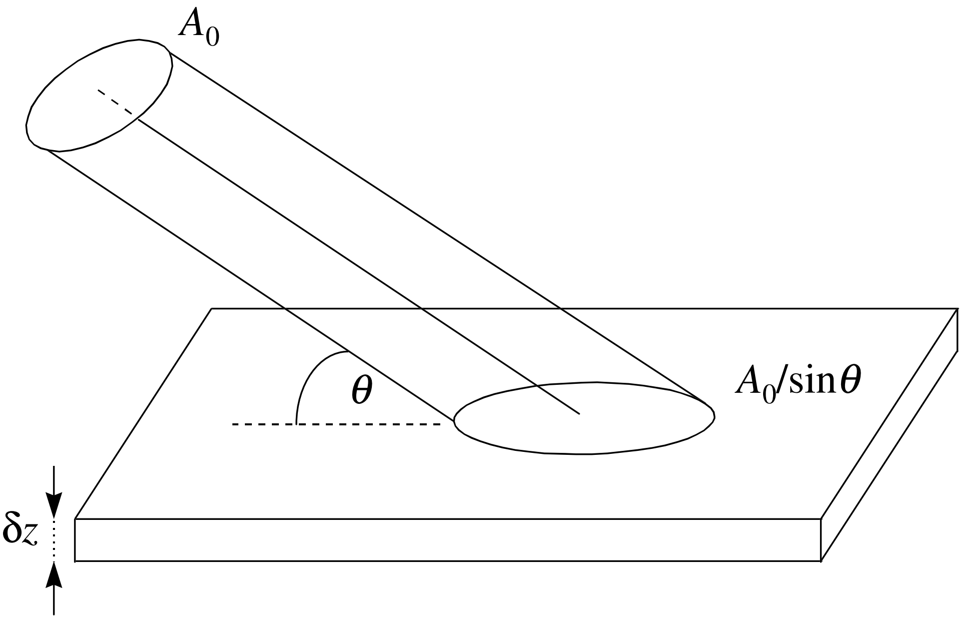

Figure 2.6: Geometry used in deriving the specular reflectivity within the Born approximation.

calculated reflectivities are compared with the experimental data and the starting parameters can be adjusted by some optimising procedure, such as non-linear least-squares. It will be clear that this fitting procedure becomes impossible if the SP becomes too complicated. Therefore the need arises for a closed-form expression of the reflectivity which can be more easily inverted to get the SP. The Born approximation for scattering provides such a formula at the cost of several inaccuracies. It is noted that the Born approximation is sometimes called the kinematic approximation.

The essential point of the Born approximation (BA) is that the incident photons (or neutrons) are scattered only once, whereas this is certainly not true in the vicinity of the critical angle for total reflection. Therefore the Born approximation is only true for wave numbers that are about three times as large as the critical wave number. Then the wave function inside the medium is very close to the incident wave function. To get the scattered wave function the complete SP is treated as a perturbation on the unperturbed wave function. Here only a rough sketch of the derivation is given. Consider an infinitesimal thin layer with thickness δz and a wave incident under angle θ (Fig. 2.6). Then the number of scattering centers per unit area of incoming beam is $\rho_{\mathrm{e}}\delta z/\sin\theta$ (or, for neutrons $\rho_{\mathrm{n}}\delta z/\sin\theta$). To get the equivalent scattering power this has to be multiplied by the Thomson scattering length of the electron r_0 (or the coherent scattering length of the nuclei b). The specular reflectivity ΔR of the thin sheet is then obtained (since this is a dimensionless quantity) by multiplying this by the wavelength λ and taking into account the phase shift of 90$^{\mathrm{o}}$:

$$\delta R = i\lambda r_0 \rho_{\mathrm{e}} \delta z/\sin\theta = 2\pi i r_0 \rho_{\mathrm{e}} \delta z/k \tag{2.50}$$

This formula can be rewritten by virtue of Eq. 2.14:

$$\delta R = ik\frac{4\pi}{2}\frac{|\rho|}{|\rho|}\frac{\rho\delta z}{k^2} = \frac{1}{4}\frac{k_c}{k}^2 2ik\frac{\rho}{|\rho|}\delta z \tag{2.51}$$

because the squared critical wave number $(k_c)^2 \approx k_0^2\theta_c^2 = 4\pi|\rho|$. By integrating Eq. 2.51 and taking into account all phase shifts when going from one infinitesimal layer to another (layer has to be crossed twice!), the next expression is obtained:

$$R = \frac{i}{4|\rho|}(\frac{k_{\mathrm{c}}}{k})^2 2ik \int \rho e^{2ikz} dz \tag{2.52}$$

The prefactor k in front of the integral can be suppressed by integration by parts:

$$\int\limits_{-\infty}^{\infty} \rho(z)e^{2ikz}dz = \frac{1}{2ik}\left(\rho(z)e^{2ikz}\right)|_{-\infty}^{\infty} - \frac{1}{2ik}\int\limits_{-\infty}^{\infty}\frac{d\rho}{dz}e^{2ikz}dz \tag{2.53}$$

The first term on the right hand sight becomes zero because $\lim \rho(z) \to 0$ if $z \to -\infty$ (in fact $\rho(z) \equiv 0$ for $z < 0$) and

$$\lim_{z\to\infty} \rho(z)e^{2ikz} = \lim_{z\to\infty} \rho(z)e^{2ik^r z}e^{-2k^i z} = 0, \tag{2.54}$$

i.e., it is tacitly assumed that each wave vector k contains a small absorptive part $k = k^r + ik^i$. Thus Eq. 2.52 can be written:

$$R = -\frac{1}{4}(\frac{k_c}{k})^2\frac{1}{|\rho|}\int\frac{d\rho}{dz}e^{2ikz}dz = \frac{-\pi}{k^2}\int\frac{d\rho}{dz}e^{2ikz}dz = \frac{-4\pi}{q^2}\int\frac{d\rho}{dz}e^{iqz}dz \tag{2.55}$$

Thus the scattering length density gradient $d\rho(z)/dz$ is employed rather than the scattering length density ρ itself. To get the reflectivity r, which can be compared with the experimental data, the squared modulus has to be taken of Eq. 2.55:

$$r = \frac{\pi^2}{k^4}\Big|\int\frac{d\rho}{dz}e^{2ikz}dz\Big|^2 = \frac{16\pi^2}{q^4}\Big|\int\frac{d\rho}{dz}e^{iqz}dz\Big|^2 = \Big(\frac{4\pi\rho_\infty}{q^2}\Big)^2\Big|\frac{1}{\rho_\infty}\int\frac{d\rho}{dz}e^{iqz}dz\Big|^2 \tag{2.56}$$

This equation can be short-cut by replacing the asymptotic form of the Fresnel formula $(4\pi|\rho|/q^2)^2$ (see below Eq. 2.14 and Eq. 2.34) by the Fresnel formula itself:

$$r = r_{\mathrm{F}}(k)|F(k)|^2 = r_{\mathrm{F}}(q)|F(q)|^2 \tag{2.57}$$

Thus the reflectivity in the Born approximation is equal to the Fresnel reflectivity r_{F} (*i.e.*, the reflectivity of a bare substrate with a sharp interface) multiplied by a structure factor term $|F(q)|^2$, which takes into account the structural characteristics perpendicular to the surface. The scattering length density term $|\rho|$ is the average scattering length density of the system but is often taken as ρ_∞, the substrate SLD. This is normally a constant that is known beforehand. The structure factor term $F(q)$ sometimes does or does not include the substrate or average SLD. Another important modification is to replace q in the argument of the exponent and in the prefactor of the integral in Eq. 2.56 by $q_{\mathrm{f}} = \sqrt{q^2 - q_{\mathrm{c}}^2}$. This means that the wave vector within the film with respect to the average scattering length density is used for summing up the waves inside the film. In other words: refractive effects are approximately taken into account. This leads in general to a better approximation compared to the reflectivity calculated from Parrat's formalism[3].

It is clear that Eq. 2.55 and Eq. 2.56 are easier to handle than Eq. 2.47, because it is suitable for any general SP. On the other hand it is equally well clear that Eq. 2.56 can not be correct for low k-values, since it diverges as $k \to 0$, whereas the reflectivity must go to 1 below the critical angle.

As an example, the reflectivity of an arbitrary multilayer with N sharp interfaces at $z = z_j$ is calculated within the Born approximation. The scattering length density gradient can accordingly be written as:

$$\frac{d\rho}{dz} = \sum_{j=1}^{N} \Delta\rho_i \delta_j(z - z_j), \tag{2.58}$$

where $\delta_j(z - z_j)$ represents the delta dirac function at $z = z_j$ that is exactly the density derivative of a sharp interface. $\Delta\rho_j$ is the amplitude of the jump between two succesive layers and can be either negative or positive. To get the structure factor $F(q)$ the Fourier Transform of Eq. 2.58 has to be calculated, thus:

$$F(q) = \int \sum_{j=1}^{N} \Delta\rho_i \delta_i(z - z_i) e^{iqz} dz = \sum_{j=1}^{N} \Delta\rho_i e^{iqz_i} \tag{2.59}$$

The last equality follows from the properties of the Dirac delta function. The reflectivity r is obtained by taking the squared modulus of the product of the structure factor $F(q)$ and the Fresnel reflectivity for a material with average SLD $|\rho|$:

$$r(q) = \frac{16\pi^2}{q^4} \Big| \sum_{j=1}^{N} \Delta\rho_i e^{iqz_i} \Big|^2 \tag{2.60}$$

Thus an equation in closed form is obtained, in contrast with to the recursive formula Eq. 2.47.

2.2.4 The Distorted-wave Born approximation

The Born approximation treats the interaction potential as a perturbation on the potential in the absence of the sample [12]. Alternatively, the distorted-wave Born approximation (DWBA) can be utilized, in which a known reflectivity of a sharp surface is taken as the zero-order approximation and the difference between the corresponding potential and the actual potential as the perturbation. The fundamental difference between the BA and the two different DWBA's that are treated in this section is illustrated in Fig. 2.7. Usually the known potential is that of the substrate, since the substrate and its Fresnel reflectivity are known exactly. The expression for the reflectance becomes then:

$$R = R_{\mathrm{F}} + \frac{2\pi}{ik} \int_{-d}^{0} (e^{ikz} + R_{\mathrm{F}} e^{-ikz})^2 \rho(z) dz, \tag{2.61}$$

where R_{F} is the Fresnel reflectance given by Eq. 2.31. The advantage of this formula is that it can be evaluated, like the BA expression (Eq. 2.57), for general scattering length density. It is in addition more accurate than the BA, especially in the vicinity of the critical angle. The disadvantage of Eq. 2.61 is that it can not easily be inverted, *i.e.*, calculating the SLD $\rho(z)$ when the reflectance R is known.

It is also possible to develop the DWBA by taking the potential for a thin film on a substrate as the zeroth order approximation. This approach finds practical applications in experimental X-ray reflectivity and is therefore mentioned

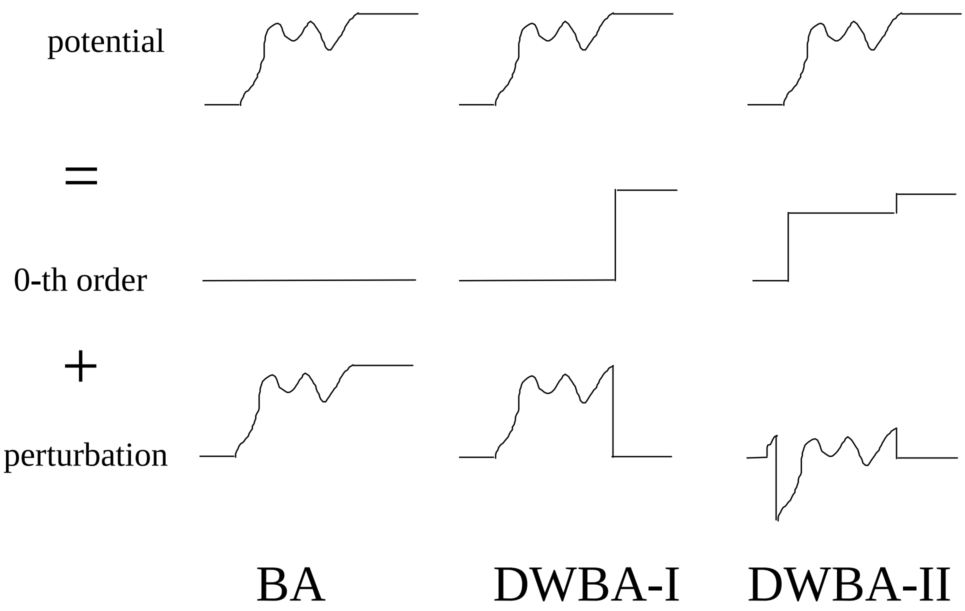

Figure 2.7: Illustration of the differences between the Born approximation and two different distorted-wave Born approximations

here. The expression for the reflectance is now:

$$R = iR_0 + \frac{2\pi r_0}{k}(a^2(k)\Delta\rho(q) + b^2(k)\Delta\rho^*(q)), \tag{2.62}$$

where $\Delta\rho(q)$ is the Fourier transform of $\Delta\rho(z)$ (and $\Delta\rho^*(q)$ its complex conjugate), the deviation with respect to the zeroth-order approximation, and R_0 the reflectance of the zeroth-order approximation. $a(k)$ and $b(k)$ are the transmittance and the reflectance in the film of constant density, respectively. It is shown in sections 3.3.3 and 3.3.4 how this formula can be used to determine the SLD.

2.3 The phase problem in reflectivity

An essential point that has not been discussed hitherto and that applies to both the exact Parrat description and the Born approximation is the phase problem. Eq. 2.55 can only be inverted (by an inverse Fourier transform) to get $d\rho/dz$ if the reflectance R is known rather than the reflectivity r. This is the phase problem. The phase is normally not measured in reflectivity and thus must it be obtained by other means, *e.g.*, fitting. Note that this is ressemblant to the situation in crystallography. There a similar phase problem exists. Approaches to tackle the phase problem in crystallography are for instance Patterson methods and direct methods. A method in reflectivity that is related to the Patterson method in crystallography inverts Eq. 2.56 rather than Eq. 2.55 since the former equation is based on the measured quantities. Then the 'difference vectors' between the structural quantities of interest in the one-dimensional scattering length density profile are obtained. This method is especially of interest in the case of a limited number of otherwise homogeneous layers on a substrate (section 3.3.1).

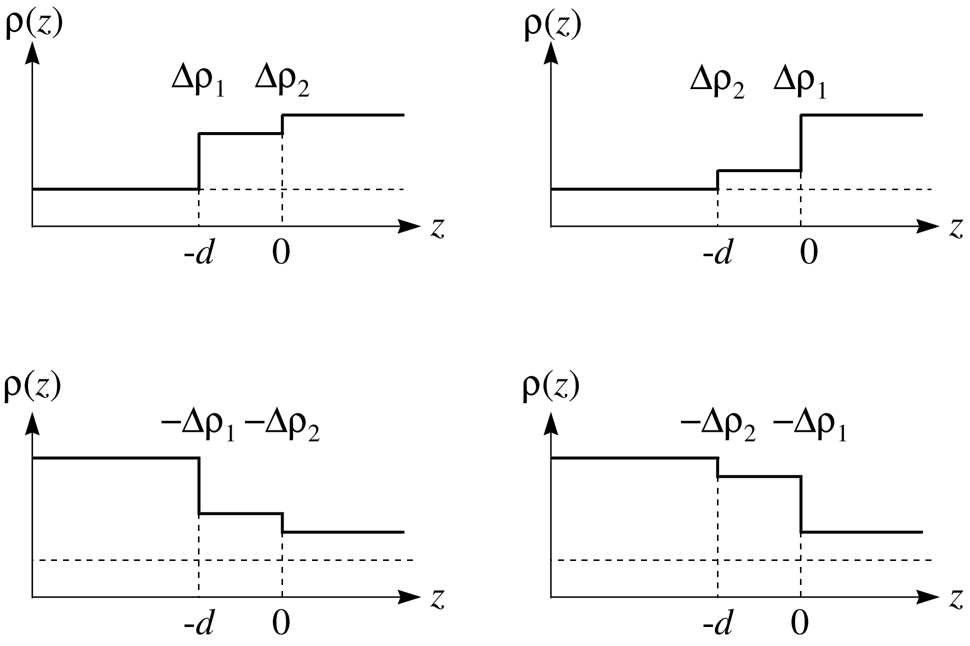

Figure 2.8: Four different scattering length density profiles that give the same reflectivity with the Born approximation.

Methods exist to measure indirectly the phase of the reflected waves [13–16]. They employ in general a reference layer with known scattering potential that is deposited in top of the system to be studied. Two measurements have to be performed: one without the reference layer, and the other with the reference layer. From the two datasets the phase set belonging to the data set for the system to be studied can be calculated. The data set, *i.e.*, amplitude set, plus the phase set constitute the reflectance set - amplitude plus phase - that can be used to calculate the scattering potential using either the Born approximation (Eq. 2.55 - inverse Fourier transform), or very sophisticated mathematical techniques to invert Parrat's recursive relations (Eq. 2.47). The latter techniques are not yet very often used, since they are still being developped. They are preferable from a theoretical point of view, because the BA contains phase ambiguities that do not allow to discriminate between SP's that are widely different. That is to say, widely different SP's could have equal reflectivities. The exact formulation, that of Parrat, contains only phase ambiguities within the resolution of the experiment.

To see how this phase ambiguity arises, the reflectivity of a single layer with thickness d on a substrate is calculated within the Born approximation. The monolayer is at $\Delta\rho_1$ with respect to the vacuum and the substrate is $\Delta\rho_2$ with respect to the layer. The (squared) structure factor $|F(k)|^2$ is (Eq. 2.59):

$$|F(k)|^2 = |\Delta\rho_1 + \Delta\rho_2 e^{ikd}|^2 = \Delta\rho_1^2 + \Delta\rho_2^2 + \Delta\rho_1\Delta\rho_2\cos(2kd), \tag{2.63}$$

and the reflectivity becomes:

$$r(k) = r_{\mathrm{F}}(k)|F(k)|^2 = \frac{\pi^2}{k^4}(\Delta\rho_1^2 + \Delta\rho_2^2 + \Delta\rho_1\Delta\rho_2\cos(2kd)). \tag{2.64}$$

There are four different SLD's that give the same reflectivity according to Eq. 2.64: $\Delta\rho_1$ and $\Delta\rho_2$ may be interchanged and their signs may be changed without modifying the resulting $r(k)$. Thus the very different SLD's of Fig. 2.8 all give the same reflectivity profile within the BA, *i.e.* for wave numbers larger than about three times the critical wave number k_c. For wave numbers between k_c and about $3k_c$ the reflectivity is different and this permits to differentiate between the four different cases if an analysis method based on Parrat's recursive relations is used. It is noted that the difference becomes smaller with smaller d. Thus for very thin layers (say several nanometers), the experimental resolution inhibits to differentiate between the four different cases of Fig. 2.8, even if Parrat's recursive formula is used. In conclusion if the analysis method that is used is based on the BA, attention must be paid that the SP might be very different from the one obtained by the analysis method. The phase problem is less problematic if the exact formulism is used, but will anyhow hamper a proper analysis of the reflectivity data.

2.4 Off-specular reflectivity

Although the topic of this reader is *specular* reflectivity, it is anyhow of interest to see what happens if the specular condition is relaxed, *i.e.*, if the incident angle is not equal to the exit angle [17, 18]. This is called off-specular or diffuse reflectivity or scattering. Specular reflectivity probes structural information perpendicular to the surface, since the momentum transfer vector is normal to the surface. On the other hand, if the incident angle θ_i is not equal to the scattering angle, the momentum transfer vector q gets a component parallel to the surface (Fig. 2.9). At least two different off-specular scans can be distinguished: the detector scan keeps the incident angle θ_i constant and the rocking

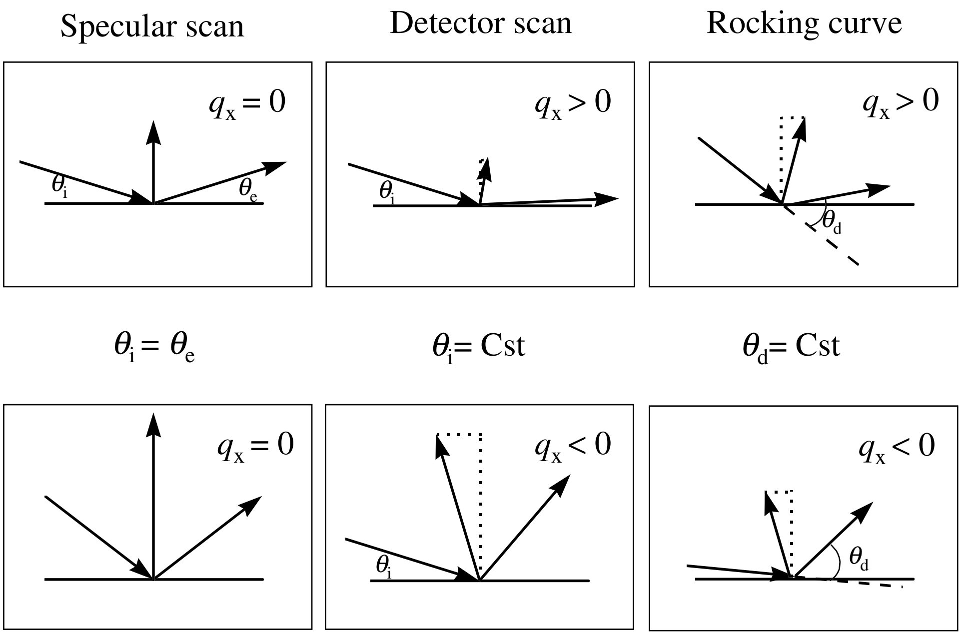

Figure 2.9: Diagrams showing the geometry of momentum transfer for specular and off-specular reflectivity scans. It should be noted that all scans are performed under grazing incidence angles with respect to the surface, but that the angles in this figure have been chosen larger for sake of clarity.

curve the detector angle θ_d, whereas the sample is rotated. Thus structural information parallel to the surface becomes available. In this way global statistical information about surfaces and interfaces over an enormous range of length scales - ångstroms to microns - is obtained. This is to be compared with surface information obtained using the atomic force microscope or the scanning tunneling microscope. Using these techniques a direct image of the surface can be obtained, in constrast to the indirect Fourier image of X-ray or neutron off-specular scattering, on length scales ranging from 100 ångstroms to microns. Thus lateral structural inhomogenieties at a scale lower than 100 ångstrom cannot be detected by AFM or STM, whereas off-specular scattering can. In addition, AFM and STM only probe the surface, whereas information from buried interfaces is equally well seen by the scattering technique. The theory of off-specular reflectivity is mathematically complicated, whereas the diffusely reflected waves are of weak intensity. It is, however possible to detect off-specular scattering with laboratory equipement, but the counting times are in general long.

Chapter 3

Reflectometry

The experimental technique to determine the reflectivity of a material is called reflectometry. It is very similar to diffractometry, the technique to determine the diffraction of a material. The set-up of an reflectivity experiment requires the knowledge of general features of the behaviour of the reflectivity for different types of materials and different structural features. This point will be addressed first. Next the experimental environment of a reflectivity experiment will be discussed. Finally the data reduction and analysis will be treated.

3.1 Characteristics of specular reflectivity curves

The ultimate goal of a reflectivity experiment is the determination of the scattering potential perpendicular to the surface of the sample. This goal is in general quite difficult to reach. Quite often a model of the system is set up using a limited number of stacks or layers and it is tried to determine the SP in terms of layer thickness, roughness, and (constant) density values. It is easiest to discuss the reflectivity in terms of these parameters, since then general trends of the variation of the reflectivity with the variation of these parameters can be defined.

3.1.1 Influence of scattering potential strength

If a bare substrate is considered with SLD ρ_s then, by virtue of Eq. 2.14, the critical angle θ_c shifts to larger values when the SLD becomes larger (Fig. 3.1). The reflectivity can be considered as Fresnel reflectivity (see section 2.2.1). For negative SLD's there is no critical angle, for instance for hydrogen in the case of neutron reflection. The critical angle θ_c can be read off from the data as the point where the reflectivity starts to deviate from unity. In practice, especially when there is finite absorption, the experimental critical angle is read off as the value where the reflectivity is dropped to 50% of its value at the plateau of external reflection. In this case the absorption makes that the sharp corner that occurs for absorptionless media becomes rounded (Fig. 3.2). This practice might slightly overestimate the real critical angle.

These considerations are equally well true for composite systems, such as multilayers on top of a substrate. The critical angle is then a non-analytical function of the composition of the complete systems. Two cases should be considered: one for real SP's and the other for complex SP's. If for an absorptionless medium, in the case of a single layer on a substrate, the SLD ρ_f of the layer is less than that of the substrate (thus with film medium critical angle $\theta_{\mathrm{c}1}$ smaller

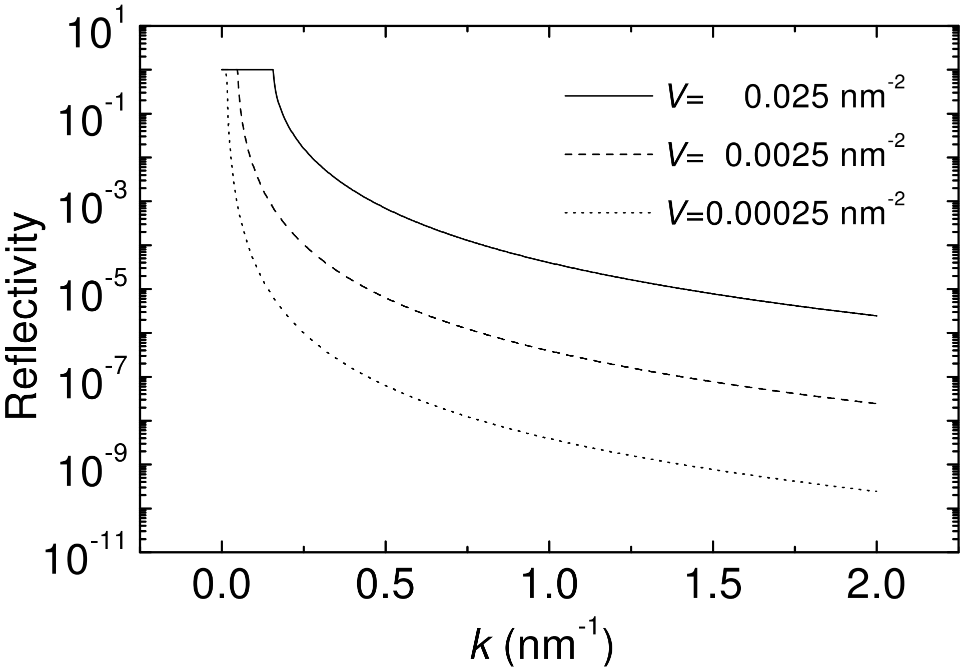

Figure 3.1: Reflectivity of bare absorptionless substrates. The critical angle of total reflection shifts with the magnitude of the scattering potential.

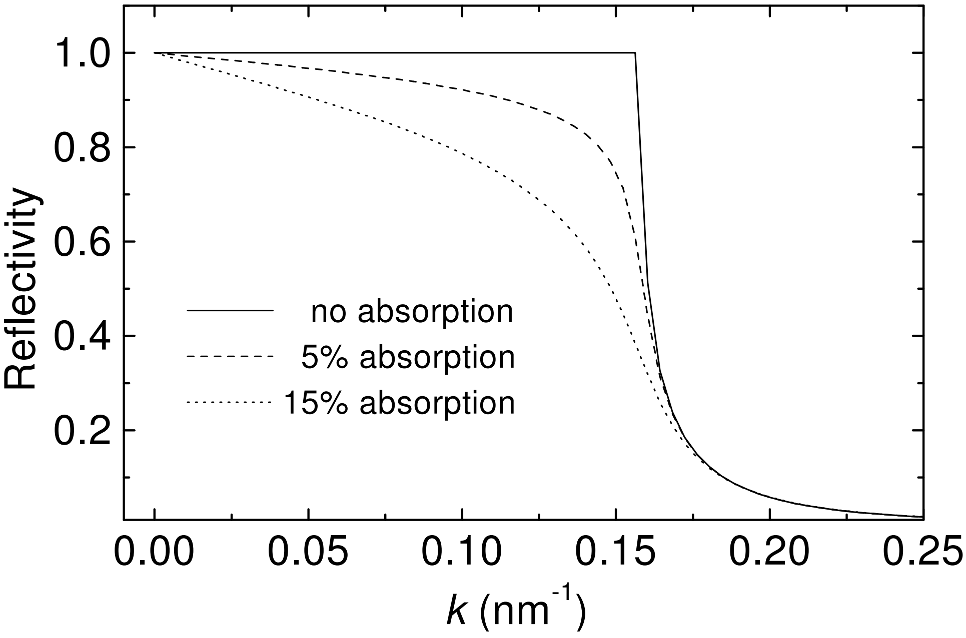

Figure 3.2: Influence of absorption on the reflectivity of a bare substrate with constant scattering potential ($V_{\rm s} = 0.025\ {\rm nm}^{-2}$).

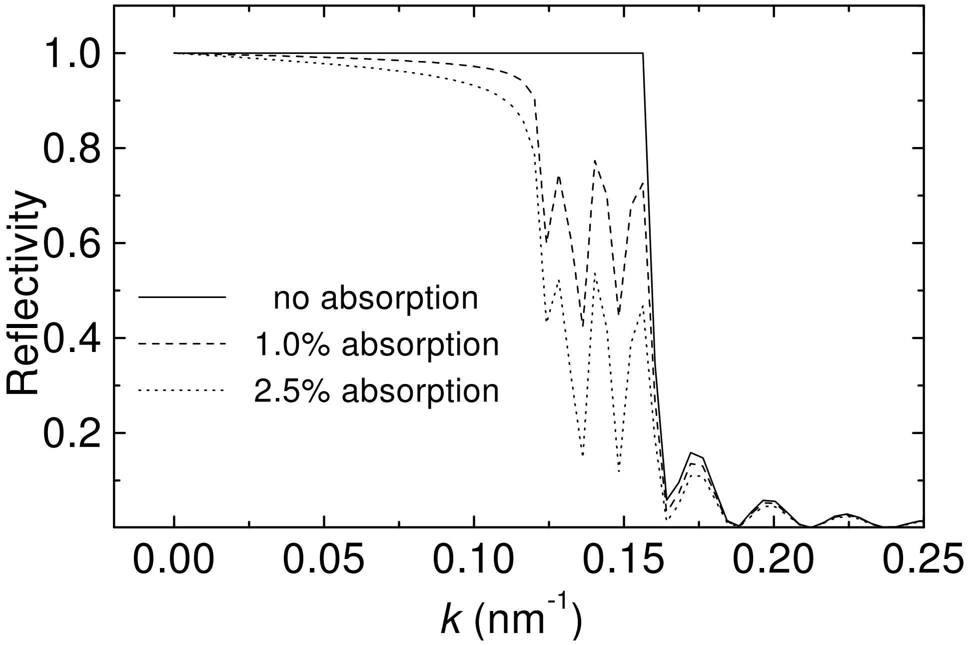

Figure 3.3: Influence of absorption on the reflectivity of a substrate ($V_s = 0.025$ nm^{-2}) plus single layer ($V_f = 0.015$ nm^{-2}) of thickness $d = 100$ nm.

than the substrate medium critical angle θ_{c2}) , then the critical angle θ_c of the complete system is always equal to the critical angle of the substrate. Beyond the film critical angle θ_{c1}, a part of the incident beam is transmitted but anyhow totally reflected at the film/substrate interface. Only beyond the substrate critical angle θ_{c2} a part of the incident beam will penetrate into the material and the reflectivity starts to drop.

If, on the other hand, the media are absorptive, the reflectivity starts to fall as soon as the incident angle becomes larger than the film critical angle θ_{c1}. Much of the intensity will be anyhow reflected and the reflectivity tends to level off untill the second critical angle film critical angle θ_{c2} is reached. Then the wave penetrates also into the substrate. This holds only for rather thick layers or for strong absorption. For very thin layers never two critical angles will be observed. Fig. 3.3 shows that already quite small absorption (imaginary part of the SP equal to 1% of that of the real part) makes that the first (film) critical angle shows up for a 100 nm thick thin film, whereas it is completely absent if the film and the substrate would be absorptionless. Fig. 3.4 shows that for the same system with 1% absorption the first critical angle shifts towards the real film critical angle if the film gets thicker. The two critical angles can hardly be resolved for a 10 nm thick film.

If $\rho_f > \rho_s$ then a similar situation occurs, at the exception that never two distinct critical angles are observed, regardless if the medium is absorptive or not. The critical wave number is jointly determined by the SLD's of the film and the substrate:

$$\sqrt{4\pi\rho_s} \leq k_c \leq \sqrt{4\pi\rho_f} \tag{3.1}$$

For thick films k_c is close to the right hand side of Eq. 3.1, whereas for thin films it is close to the left hand side. There

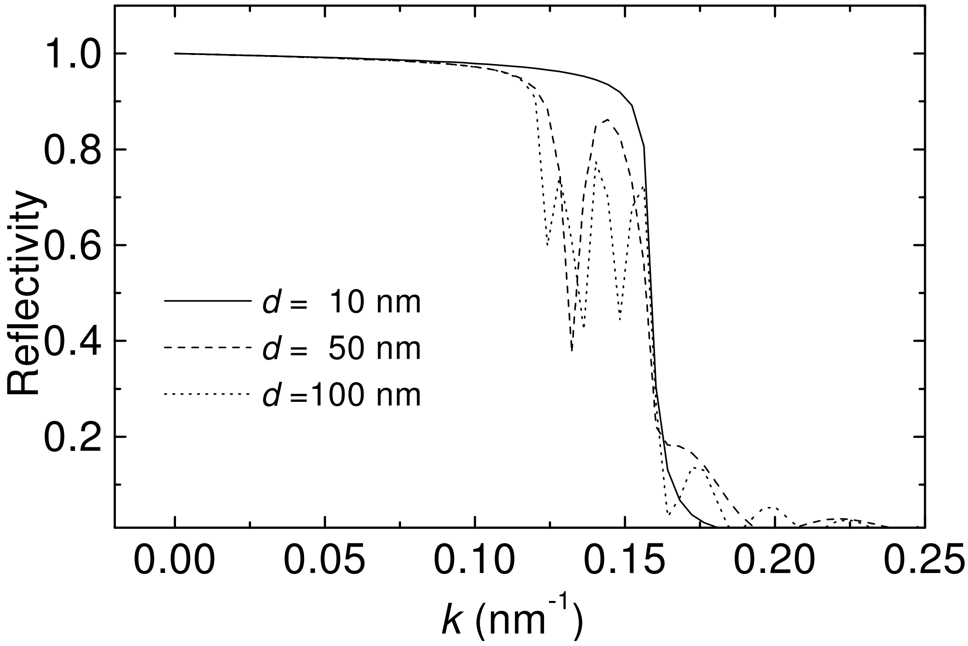

Figure 3.4: Influence of 1.0% absorption on the reflectivity of a substrate ($V_\mathrm{s} = 0.025$ nm^{-2}) plus single layer ($V_\mathrm{f} = 0.015$ nm^{-2}) for different values of the thickness.

is also a dependency on the magnitudes of the SLD's of film and substrate, respectively.

The determination of the average SP of a (multi)film from the value of the critical angle is thus quite tricky if the total layer thickness is too thin. If it is known, however, that the layer is thick, then it could be a safe and fast procedure.

3.1.2 Influence of layer thickness

When a film with uniform density is deposited on top of a substrate, the normal Fresnel reflectivity of a bare substrate becomes modulated by oscillations due to the interference of waves reflected at the air/film surface and waves reflected at the film substrate interface (see also section 3.3.1 and the equations 2.42 and 3.13). These oscillations are called Kiessig fringes after the man who has discovered them in the thirties [19]. The period of the fringes is inversely proportional to the thickness of the layer: the thicker the film the smaller the oscillation period (Fig. 3.5). Due to the finite resolution of the experiment, there is an upper limit on the layer thickness that can be detected by reflectometry. Oscillations will be smoothened out by the instrumental resolution function if its period becomes too small. Other reasons for the disapparance of Kiessig fringes include a macroscopic curvature of the sample or lateral inhomogeneities (*i.e.*, thickness variations). The instrumental smearing is taken into account by convolving the theoretical (unsmeared) reflectivity with a convolving operation, normally a gaussian function with width σ_v.

$$r_\mathrm{CV}(k) = P[r_\mathrm{DC}(k)] = \int_{-\infty}^{\infty} r_\mathrm{DC}(k-\kappa) IPF(\kappa) d\kappa \qquad (3.2)$$

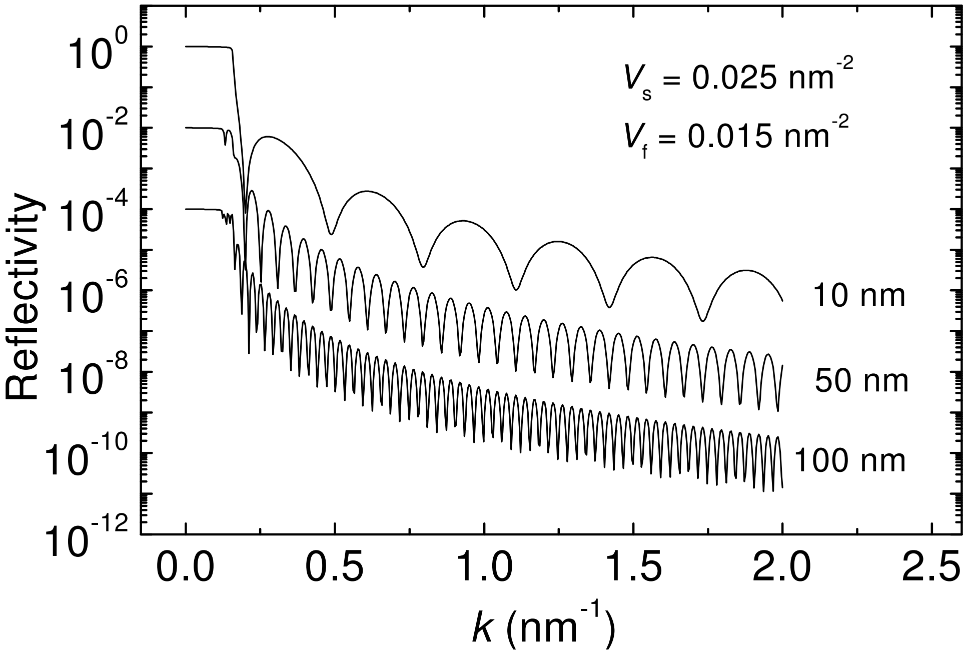

Figure 3.5: Reflectivity of monolayers of different thickness deposited on a substrate. 1% absorption is included in the calculations.

where r_{DC} is the unsmeared reflectivity function, r_{CV} the reflectivity after smearing, P the convolution operator, and IPF the instrumental resolution function.

$$IPF(k) = \frac{1}{\sqrt{2\pi}\sigma_{\mathrm{v}}} e^{-\frac{k^2}{2\sigma_{\mathrm{v}}^2}} \tag{3.3}$$

The gaussian width (variance of the distribution) σ_{v} itself is the sum of two contributions:

$$\sigma_{\mathrm{v}}^2 = \sigma_{\lambda}^2 k^2 + \sigma_{\mathrm{c}}^2, \tag{3.4}$$

where σ_λ is the width due to the wavelength distribution $\Delta\lambda$:

$$\sigma_\lambda = \frac{\Delta\lambda}{\lambda} \frac{1}{\sqrt{2\ln 2}}. \tag{3.5}$$

The factor $1/\sqrt{2\ln 2}$ relates the variance of the gaussian distribution σ_λ to the full width at half-maximum (FWHM) of the relative wavelength distribution $\Delta\lambda/\lambda$. The latter quantity can be more easily determined than the variance. The variance σ_{c} in Eq. 3.4 is related to collimation effects. In the X-ray case it is quite often taken to be related to the FWHM of the direct beam in the absence of the sample in a similar way as in Eq. 3.5 [20]. In the neutron case the determination of σ_{c} is more difficult [21].

Fig. 3.6 shows the effect of instrumental smearing on the amplitude of the oscillations. If the oscillations are much wider than the effective half width of the incident beam then there is hardly any difference between the smeared and

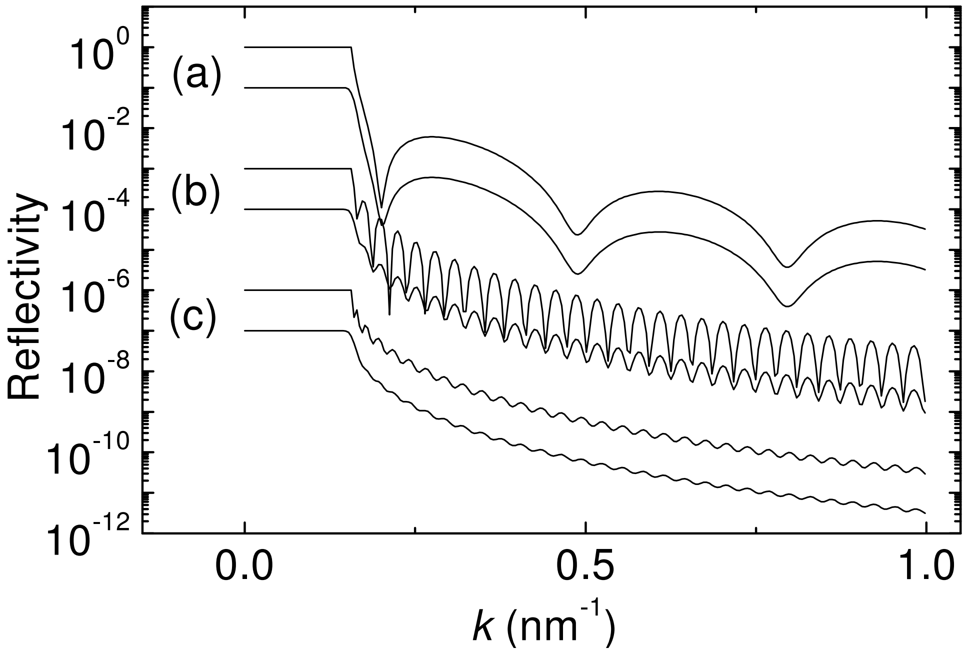

Figure 3.6: Reflectivity of monolayers of different thickness deposited on a substrate. A realistic smearing function is taken into account. (a) $V_s = 0.025$ nm^{-2}, $V_f = 0.015$ nm^{-2}, $d = 10$ nm; (b) $V_s = 0.025$ nm^{-2}, $V_f = 0.015$ nm^{-2}, $d = 100$ nm; (c) $V_s = 0.025$ nm^{-2}, $V_f = 0.023$ nm^{-2}, $d = 100$ nm. The upper curve for each entry is the unsmeared reflectivity and the lower curve the smeared one.

unsmeared curve (Fig. 3.6a; the upper curve is the unsmeared reflectivity and the lower curve the smeared one). If, however, the layer becomes thicker, and consequently the fringe period smaller, then the instrumental smearing might considerably affect the experimental reflectivity (Fig. 3.6b). If the unsmeared constrast is already low, the oscillations might get lost due to the instrumental smearing. The lowest curves of Fig. 3.6 show that this might easily happen. There is equally well a lower thickness limit that can be detected because the oscillations may not be visible anymore if its period depasses the upper limit of the interval of data collection. For laboratory equipment these two limits are approximately 350 and 3 nm, respectively. In some cases fringes of thicker films (up to 450 nm) can be resolved at the condition that the surface is extremely flat on a macroscopic scale and that the film is both laterally and vertically homogeneous. Recently thickness determinations up to 1000 nm has been reported in the literature [22]. In this case extremely good X-ray optics (four-bounce germanium [220] monochromator in the incident beam and a channel cut Ge [220] crystal in the reflected beam) and a flat surface are required. The amplitude of the oscillations depends on both the wave number and the density contrast between film and substrate. The larger the contrast the larger the oscillation amplitude. Here again the contrast is modified, *viz.* diminished, by the effects of the instrumental smearing, but also by absorption. This makes that there is an under limit to the contrast that can be detected by reflectivity. Guide lines are difficult to give, since the flatness of the surface, interfacial roughness, and lateral inhomogeneities are intervening factors as well, that could give an additional smoothening effect. Using copper X-ray's, the interference fringes of a sufficiently flat silica film with mass density 2.20 gcm^{-3} on top of a silicon substrate with mass density 2.33 gcm^{-3} can be made visible. Fig. 3.7 shows this case for layer thicknesses of 5, 50, 250 nm, respectively. It is seen that the

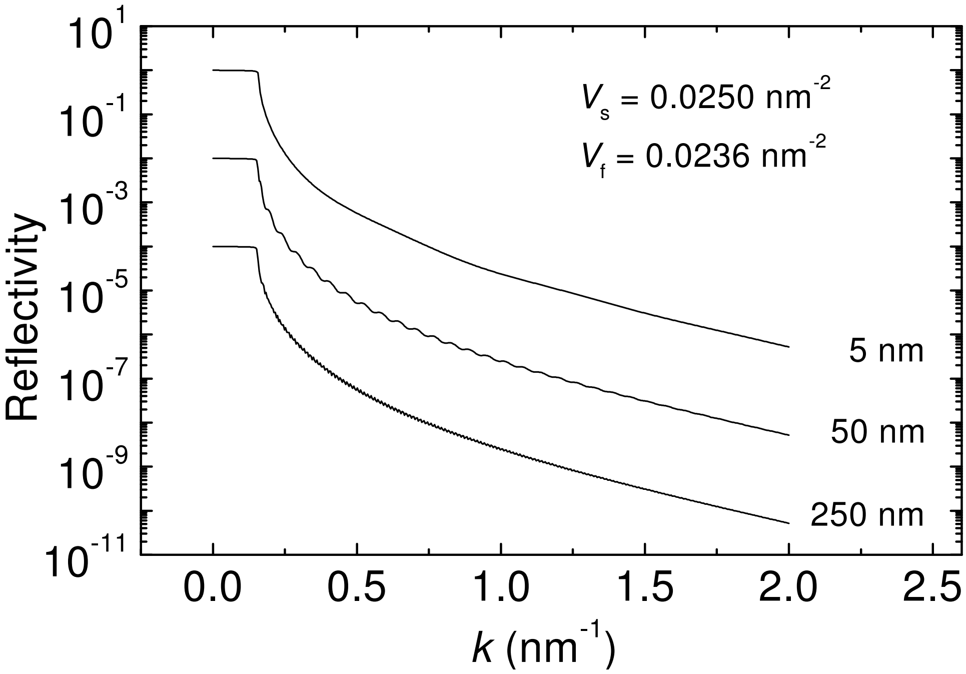

Figure 3.7: Reflectivity of monolayers of different thickness deposited on a substrate. A realistic smearing function is taken into account and 1% absorption is included in the calculations, as well as realistic values for the interfacial roughness.

oscillation due to the 5 nm layer are not discernable, because of the very low contrast and the finite interval. The 50 nm oscillations are visible, but are damped for larger k-values due to absorption and interfacial roughness. Finally, the 250 nm oscillations are not visible anymore, because the density contrast is too low between film and substrate. This shows that the aforementioned lower and upper thickness limit that can be detected by XR or NR also depends on the effective contrast between film and substrate density.

For multilayers, like bi- and trilayers, more oscillation periods might be visible in the reflectivity curve, if the different layer thickness values are sufficiently distinct, and if the different SP's are sufficiently distinct. For more complicated cases it can be very difficult to resolve the different periods. Fig. 3.8 shows reflectivity examples for a double layer (a) and a triple layer (b) on top of a substrate. In (a) the small rapid oscillations due to the thickest layer of 50 nm can be readily distinguished, whereas the strong and slow oscillations correspond to the 12 nm surface layer. In (b) it is not so easy anymore to disentangle the different periods. The oscillations due to the thinnest and thickest layers are quite easily found, but the oscillations due to the 50 nm thick layer get lost in the interference pattern of the two others. The reflectivity is given by the squared absolute value of Parrat's recursive relation Eq. 2.47.

3.1.3 Influence of interfacial roughness

Interfacial roughness is a parameter that is only used if the model that is used to fit the reflectivity data consists of a distinct number of stacks of uniform density and sufficient thickness. If for instance the Born approximation, Eq.

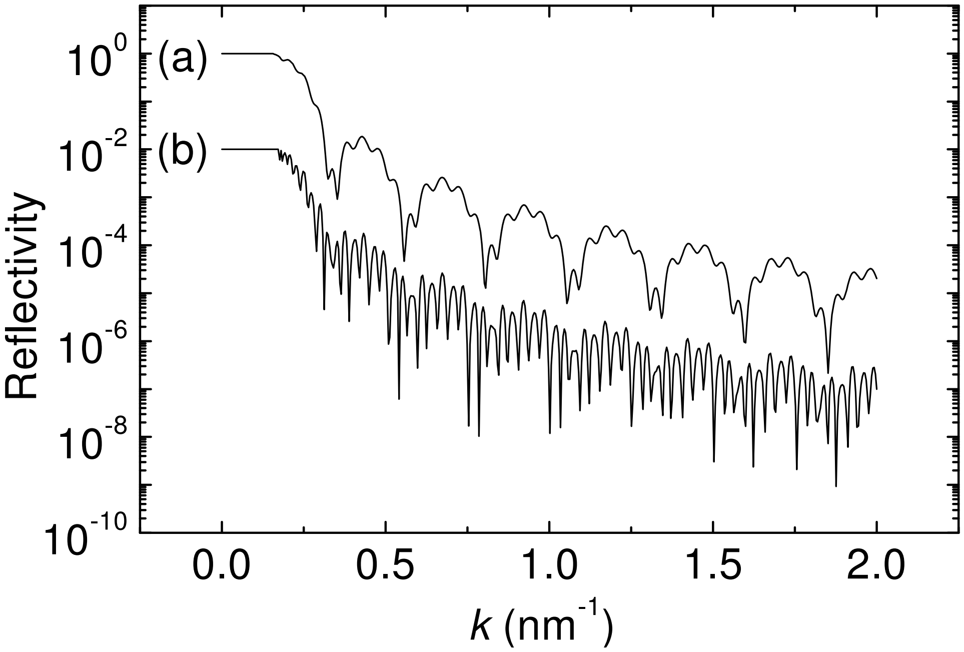

Figure 3.8: Reflectivity of a double layer (a) and a triple layer on top of a substrate. Parameters: (a) $V_\mathrm{s} = 0.025$ nm^{-2}, $V_\mathrm{l1} = 0.047$ nm^{-2}, $d_1 = 12$ nm, $V_\mathrm{l2} = 0.015$ nm^{-2}, $d_2 = 50$ nm; (b) $V_\mathrm{s} = 0.025$ nm^{-2}, $V_\mathrm{l1} = 0.030$ nm^{-2}, $d_1 = 87$ nm, $V_\mathrm{l2} = 0.047$ nm^{-2}, $d_2 = 12$ nm, $V_\mathrm{l3} = 0.015$ nm^{-2}, $d_3 = 50$ nm.

2.57, is used to analyze the reflectivity data, then roughness is a parameter that is implicitly present in the resulting SP. Roughness, however, is a structural parameter that is very often used in other surface and thin film analysis techniques, notably in atomic force and scanning tunneling microscopy (AFM and STM, respectively). It is in addition a parameter that is very important in many modeling theories of thin film growth. The roughness σ is defined as the mean-square amplitude of density fluctuations with respect to a reference level z_0:

$$\sigma = \sqrt{< z - z_0 >^2}. \tag{3.6}$$

If the fluctuations follow gaussian statistics then it can be shown that the reflectivity of a substrate is reduced by an exponential factor that incorporates the roughness parameter σ [17, 23]:

$$r'(k) = r(k)e^{-4kk_\mathrm{s}\sigma^2} \tag{3.7}$$

This equation shows that the reduction of the Fresnel reflectivity is more pronounced at large k than at small k. Other formula's are changed likewise. For instance, in the Parrat formula (Eq. 2.47) the Fresnel coefficients R_i have to be multiplied by an exponential of the form $\exp(-2k_{i-1}k_i\sigma_i^2)$.

In the case of a single layer on top of a substrate two roughness parameters can be defined: one for the air/film interface (σ_1) and one for the film/substrate interface (σ_1). If the roughness values are not too large - say below 2.0 nm - then the overall fall-off of the reflectivity curve is determined by the value of σ_1. σ_2 has the effect of an additional

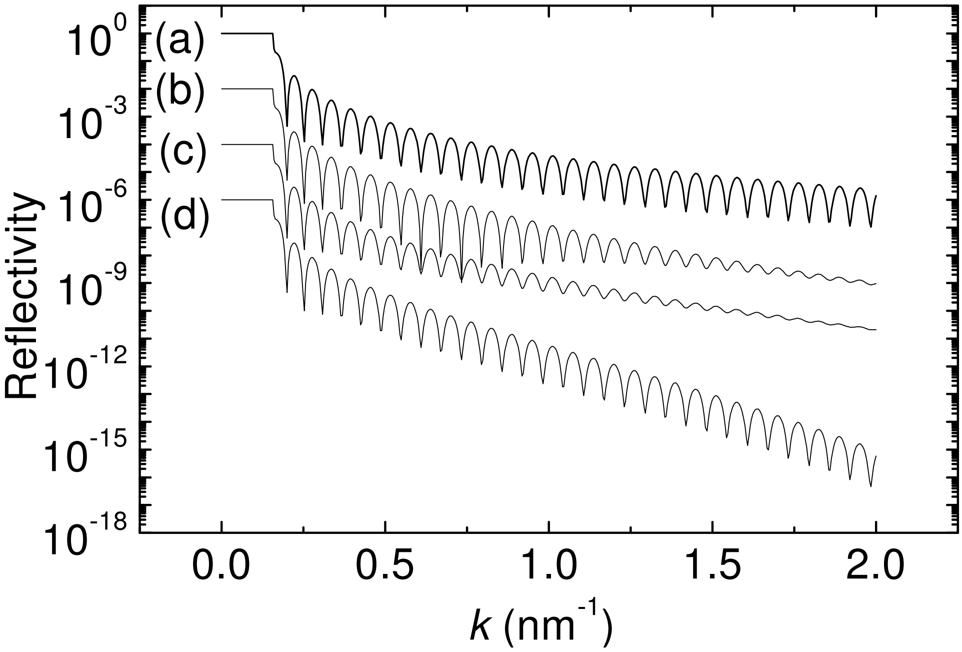

Figure 3.9: Influence of interfacial roughness on reflectivity of a 50 nm thick monolayer. $V_{\rm f} = 0.015$ nm^{-2} on top of a substrate $V_{\rm s} = 0.025$ nm^{-2}. Parameters (with σ_1 the surface roughness and σ_2 the interfacial roughness): (a) $\sigma_1 = 0.0$ nm, $\sigma_2 = 0.0$ nm; (b) $\sigma_1 = 0.7$ nm, $\sigma_2 = 0.3$ nm; (c) $\sigma_1 = 0.3$ nm, $\sigma_2 = 0.7$ nm; (d) $\sigma_1 = 0.7$ nm, $\sigma_2 = 0.7$ nm.

smoothening that increases with increasing k. Smoothening does not occur if the value of σ_1 happens to be approximately similar to that of σ_2. Then the reflected waves at the two interfaces are reduced by approximately the same amount and the coherence between the waves is conserved (Fig. 3.9).

The foregoing discussion assumes that the rough surface can be approximated by a gaussian distrubution of valleys and peaks, a requirement that is not always met in practice. Equally well, the diffuse scattering from a rough surface may be important and is not included in the foregoing model. The theory described by Sinha *et al.* [17] (see also Palasantzas *et al.* [24] and Filies *et al.* [25]) gives a much better description for a general surface, whether it is a step surface or a fractal surface. In addition it separates the diffusive and the specular contribution of the reflectivity within the framework of the distorted-wave Born approximation.

3.2 Experiment

The experimental requirements can be classified according to the requirements concerning the sample and those for the technical set-up. First the requirements for the samples are discussed and accordingly the experimental set-up. Proper alignment and selection of the data collection parameters are of crucial importance for a high-quality reflectivity data set. These will be treated lastly.

3.2.1 Sample requirements

All sort of samples can be used, whether crystalline, amorphous, or liquid-like, as long as their surfaces are sufficiently flat on a macroscopic scale (see also the next section). The sample holder should of course stay horizontal if liquids are used. The tube and detector move then in what is called θ/θ geometry. The size of the surface depends on the experimental environment to be used. If the surface is not macroscopically flat a large-area sample has no use. Special cells can be constructed if the sample is volatile, or if its surface reacts with air, or if reflectivity is to be measured as a function of temperature.

3.2.2 Equipment and setup

In reflectometry normal goniometers can be used combined with the normal optics for X-rays and neutrons, at the condition that special care is paid to the alignment of the apparatus, notably the centering of the surface of the sample into the beam. It is advantageous to be able to cut the beam height by, *e.g.*, a knife edge, in order to reduce the surface area to be probed for very low angles. This surface area varies with $1/\sin\theta$. For very low angles, this area is thus very large and deviations from planeity might easily affect the resulting reflectivity. If a knife edge is used to cut the beam height and thus to reduce the effective irridiated area, spatial inhomogenities are likely to disturb to a lesser extent. In addition to this beam cutting it may be necessary to attenuate the beam intensity by either a controlled reduction of the generator power, or by inserting an absorbing foil inside the beam. The latter is preferable, because by changing the anode power the zero settings of the goniometer might change slightly. The reduction of the beam intensity is necessary, because below the critical angle, the sample acts as a mirror for X-rays (or neutrons): 100% of the intensity of the incident beam is reflected. Beyond the critical angle, the intensity of the reflected beam rapidly falls off. For a homogeneous substrate this fall-off goes with the fourth power of the reduced wave number k_c (Eq. 2.56). To be able to measure as far as possible, a rotating anode might be used. Another solution is to use synchrotron radiation. It has to be emphasized, however, that nowadays ordinary laboratory equipment is of sufficient quality to measure reflectivities over a range of nearly 8 decades, even without a rotating anode. This is sufficient in most of the experimental cases. With synchrotron radiation one could measure 10 decades, and with a resolution which is superior to that of laboratory equipment.

The normal safety considerations that hold for a diffraction experiment should be taken into account when performing a reflectometry experiment. It should, however, be remembered that a 100% redirection of the incident beam intensity could take place when working at glancing incidence angles, a situation that normally never occurs in ordinary powder diffraction.

3.2.3 Alignment of the goniometer

The alignment of the goniometer is normally identical to that for ordinary diffraction, and is thus specific for each apparatus. The determination of the zero point of the θ angle, normally the sample holder angle, is - however - a bit different for reflectometry. Once the zero of the 2θ scale and the center of the goniometer have been determined, the sample is placed into the beam and subject to the irradiation at a glancing angle that is slightly below the critical angle, say 0.15°. The detector is set at 0.3°, which is exact because the 2θ scale has already been set. Next the sample is rotated over a small interval, normally 0.1°-0.15° while keeping the detector at the same position (the sample is 'rocked' and a 'rocking curve' of the sample is obtained, see also section 2.4). The intensity of the rocking curve is maximum at the specular condition $\theta = 2\theta$. If the maximum of the intensity is found at, say 0.145°, the θ scale should be reset by 0.005°. This procedure can be repeatively reproduced to obtain a stable zero setting of the θ axis.

The profile of the rocking curve gives some indications on the planeity of the surface. If its width (FWHM for instance) is comparable to that of the direct beam then the surface is flat on a macroscopic small. If the FWHM is much larger, or if two peaks can be discerned, then the surface is not flat on a macroscopic scale, and the resulting reflectivity will be an incoherent superposition of several reflectivity curves from different parts of the surface that are slightly inclined with respect to each other. Thus details in the reflectivity will be smoothened out. This smoothening is in addition to the smearing due to the instrumental resolution function, *viz.*, due to the divergence and wavelength spread of the beam.

3.2.4 Selection of measuring parameters

Once the sample and the goniometer are properly aligned, the data collection parameters have to be determined. There are ofcourse several ways to do this. Here a personal point of view is given. Parameters that are given are for a typical X-ray reflectivity experiment performed using laboratory equipement. They should be adjusted for a fixed-wavelength neutron experiment or one using synchrotron radiation. Parameters are very different in the case of a Time of Flight (TOF) neutron experiment.

First a rapid $\theta/2\theta$ scan is performed from 2θ=0.0° to just beyond the critical angle. This can be done with a wide step and a small counting time because the intensity is large. If the alignment has been properly performed a small peak of about one half of the intensity at the plateau of total external reflections is visible at very small angles $< 0.1^\circ$ (see Fig. 3.10). This peak is due to the fact that the sample masks half of the incident beam so that its center is no longer at 2θ=0.0°, although it was perfectly centered in the absence of the sample. The center is therefore shifted to $2\theta = 0.5w$ with w the half width at half maximum of the direct beam in the absence of the beam. If this small peak is not seen, it means that either the zero of the 2θ scale is not correct, or that the surface is not properly aligned with the goniometer axis. For larger angles the intensity increases at a rate that depends on the effective width of the incident beam. For a certain angle the footprint of the beam on the sample becomes smaller than the sample and the reflectivity reaches its steady state value at the plateau of total external reflection (PTER). Just below the critical angle, the intensity starts to fall off rapidly. The presence of a well defined PTER is the signature of planeity of the surface on a macroscopic scale and of a well-chosen beam width. Of course, this holds only if the critical angle θ_c is far enough from the origin. Especially for neutron reflection the absence of a nice PTER is not dramatic.

If the reflectivity curve around the critical angle is satisfactory an idea has to be obtained on the intensity for larger angles in order to define the counting times for each step. As a rule of thumb, one should have about 1000 counts for each step to ensure good statistics. Thus if for a certain angle the intensity is found to be 200 counts per second, the step time for the final data collection should be taken to be 5 seconds for that angle. In this way the whole range can be scanned and divided into intervals with fixed step times. The step size should be chosen according to the details that are seen in the reflectivity curve. If there are no fringes, then the step size can be chosen rather large: 0.02°- 0.03° in 2θ is not exceptional large in that case. However, it is in general a good idea to choose the step size rather small (say between 0.002° and 0.006° in the vicinity of the critical angle, because of the extreme rapid fall-off of the intensity. This ensures an accurate determination of the critical angle and thus the average scattering length density of the material to

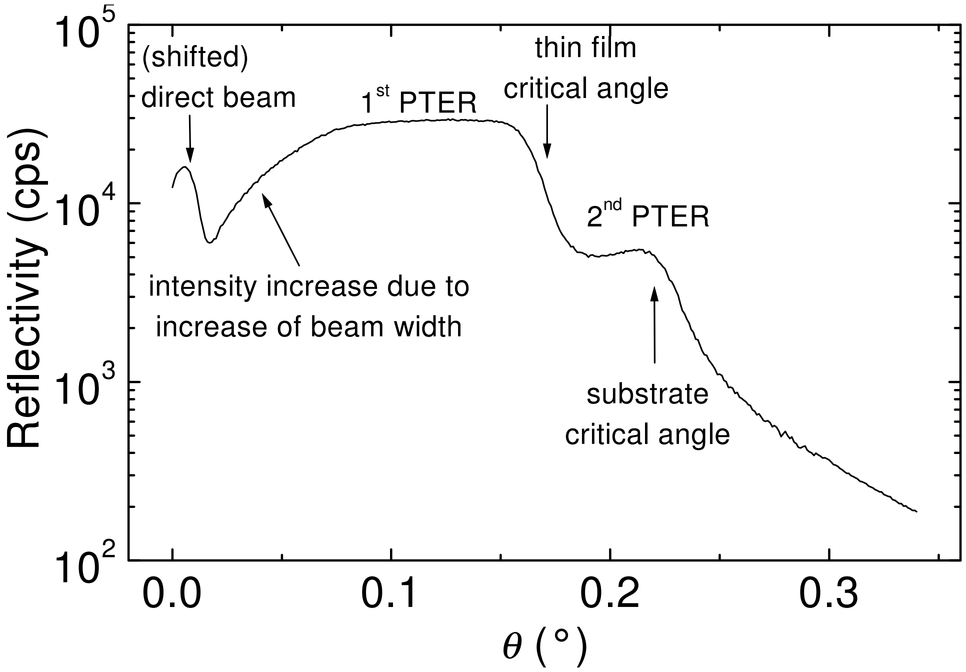

Figure 3.10: Experimental X-ray reflectivity curve of a hybrid inorganic/organic thin film on top of a Si-substrate. Typical features due to the geometry of the reflectivity experiment are indicated by arrows. PTER refers to the plateau of total external reflection; the appearance of two plateaus is discussed in section 3.1.1.

be studied. If there are fringes visible in the reflectivity curve, then a step size can be selected on the basis of the period of the fringe. In order to well describe the fringe, the step size should be taken as one tenth of the period of the fringe.

Using the in this way determined set of step sizes and step times the total time of the data collection can be determined. The largest angle for which intensity data can be collected is determined by the total time one wants to spend on the data collection. The objectives of the data collection should also be taken into mind. If the data collection only serves to determine the average scattering length density, then it is of no use to go to very large angles. Data collection up to two or three times the critical angle is sufficient in that case. It is then unlikely that more than 10 minutes have to be spent on the data collection, even with very small step sizes. If however accurate values of the roughness are required, data have to be collected as far as possible. Runs of more than 12 hours are in the latter case no exception using normal laboratory sources. They require that the zero settings of the goniometer remain stable over that period.

When the data collection is finished, the data are to be scaled. Scaling between the different intervals can be done on the base of the different step times: intensities are to be compared. Another possibility is to measure the data twice in a small overlap region, using the step times on either side of the interval boundary. The data can then be properly compared and a scaling factor can be determined. Finally the so-called ’dead current’ of the detector has to be subtracted from the intensity data. The dead current is the intensity that is recorded by the detector when the shutter of the X-ray tube is closed. The reflectivity at the PTER is by definition equal to unity in the absence of absorption. Therefore all data can be normalized to the intensity at the PTER. This practice is subject to errors if there is significant absorption or if the PTER is not completely flat. Normalizing to unity should therefore be done sometimes by hand, *i.e.*, by inspecting the actual data at the PTER using a graphical program.

If the step size is variable over the data collection interval, it can be advantageous for computational purposes to redefine the data set for a constant step size. This can be simply done by parameterizing the experimental data points by, *i.e.*, cubic B-splines, and then to recalculate the reflectivity for an arbitrary fixed step size. This gives good results as long as the initial step sizes have been well chosen, *i.e.*, that the experimental points sample well the actual reflectivity.

3.3 Analysis of specular reflectivity data

The final stage of the reflectivity experiment is the judicious analysis of the data to find a model which is compatible with the experimental data. Some structural data can be extracted directly from the intensity data, but in order to find a general SP that corresponds to the reflectivity data one should rely on trial-and-error in conjunction with least-squares refinement of the model parameters. Finally some model-independent methods to analyze the data are discussed.

The data analysis consists of several steps that are schematized in Fig 3.11. The left part shows the analysis that is typical for the classical methods that are described in the sections 3.3.2 and 3.3.3, whereas the right side of the figure is typical for the direct determination methods of section 3.3.4. Common to the two approaches is the treatment of the raw data $I(k)$, *viz.*, scaling and noise subtraction (step I in the figure), which has been described in section 3.2.4, to get the normalized (and convolved) data r_{CV}. When using least-squares or iterative methods, a potential $V(z)$ is assumed, from which the theoretical reflectivity r_{DC} is calculated (step III on the left of Fig. 3.11). These data are to be convolved with an instrumental resolution function (step IV) in order to be compared with the experimental data (steps II and V). The model potential can then be adjusted by least squares or iteration (step VI) to reduce the difference between the experimental data r_{CV} and the calculated data r'_{CV}. Steps $III - VI$ are repeated until good agreement between experimental and calculated data is obtained. The direct methods (right side of Fig. 3.11) on the other hand involve only four steps. In the second step the experimental data are *deconvolved* and in the third step the phase is determined using either mathematical means or data from a second measurement. Finally (step IV) the potential $V(z)$ is calculated from the complex reflectance.

3.3.1 Direct determination of structural parameters

In quite a number of cases simple means can be used to determine structural parameters like density and layer thickness in a straightforward and fast way. This is especially true for the system that is composed of a substrate and a single layer. The forementioned two parameters can be derived from the position and period of the fringes that are due to the interference of waves that are reflected at the surface and those that are reflected at the interface between film and substrate. This is not immediate clear when inspecting the formula's that describe the reflectivity for such a system: Eq. 2.64 using the Born approximation or Eq. 2.42 using the exact Parrat formalism. It can however, be visualized very well by a derivation that is nearly identical to the one that leads to Bragg's law for diffraction.

Consider a thin layer of thickness d on top of a substrate (Fig. 3.12). The refractive indices are n_{f} and n_{s} for the thin layer and the substrate, respectively. It is assumed that the fronting medium of the thin layer is air or vacuum with refractive index equal to unity. The X-ray wave is incident under an angle θ (which is exaggarated in Fig. 3.12 for sake of visibility; normally it is about 0.2°-0.5°). At the surface the transmitted wave is reflected in O and transmitted in A'. The transmitted wave is not only transmitted but also refracted, because of the difference in refractive index for fronting

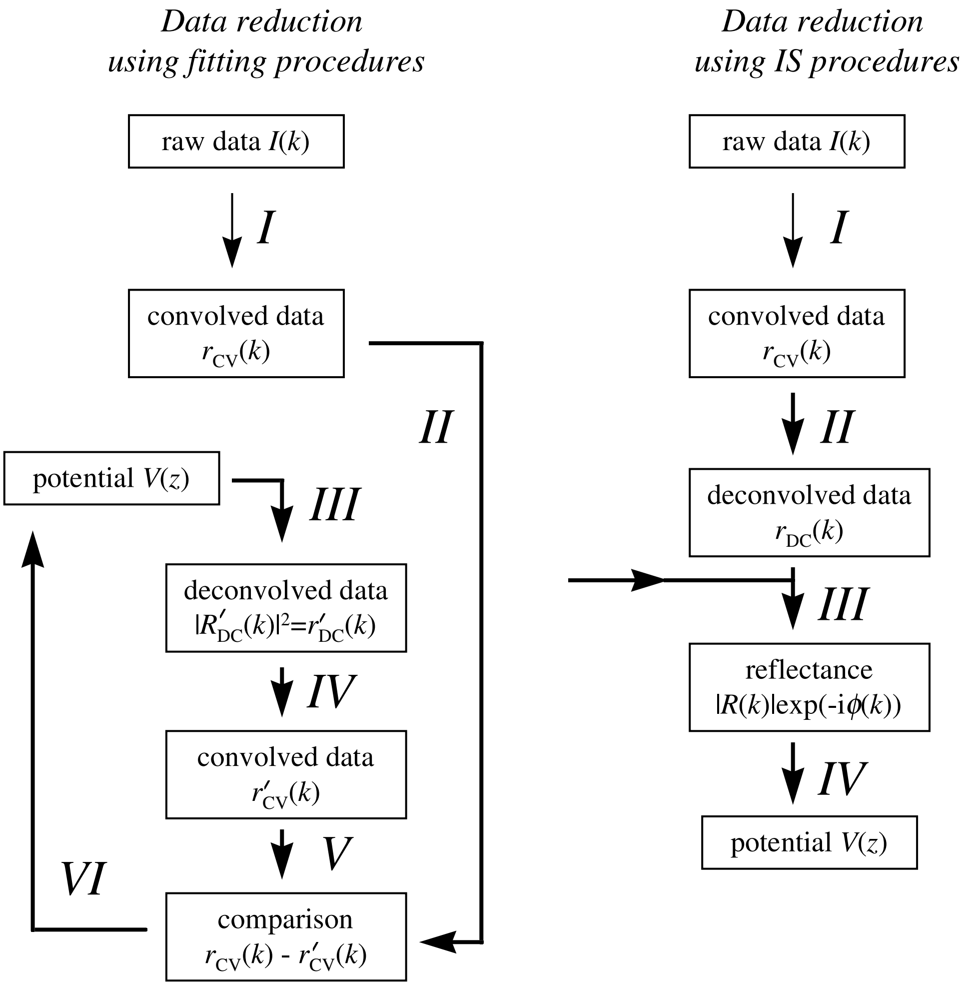

Figure 3.11: Flow diagrams showing the consecutive steps in the data analysis using least-squares (left) and inverse scattering methods (right).

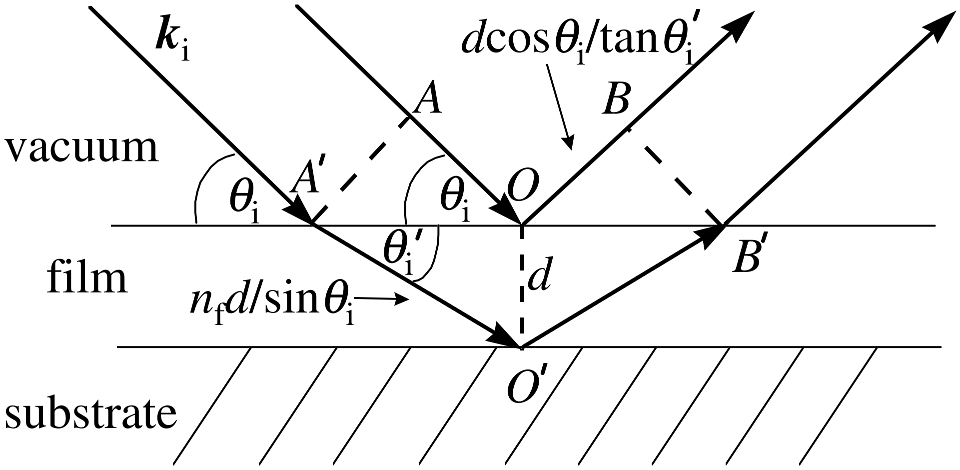

Figure 3.12: Geometry of reflectivity on a thin layer used for derivation of the extended Bragg's law.

medium and that of the film. The transmittance angle θ' can be calculated using Snell's law:

$$\cos\theta = n_\text{f}\cos\theta'. \tag{3.8}$$

The transmitted wave is reflected (and transmitted) in O' at the interface between substrate and film. The reflected wave is transmitted (and reflected) again at the surfacial interface at B'. The two exit waves can either interfere constructively or destructively (as in the derivation of Bragg's law), dependent on their phase difference that is determined by the difference in optical path length:

$$\Delta = A'O'B' - AOB. \tag{3.9}$$

If $\Delta = m\lambda$ with m an arbitrary integer, then constructive interference takes place. The difference with the derivation that leads to Bragg's law is that now the refraction is taken into account. Eq. 3.8 can be rewritten as:

$$\sin^2\theta' = 1 - \frac{\cos^2\theta}{n_\text{f}^2}, \tag{3.10}$$

whereas the critical angle is defined in terms of the refractive index as (Eq. 2.13):

$$\sin^2\theta_\text{c} = 1 - n_\text{f}^2. \tag{3.11}$$

For constructive interference we have (Eq. 3.9):

$$\begin{aligned}
\Delta &= A'O'B' - AOB = m\lambda = 2d\Big(\frac{n_\text{f}}{\sin\theta'} - \frac{\cos\theta}{\tan\theta'}\Big) \Rightarrow \\
\frac{m^2\lambda^2}{4d^2} &= \frac{n_\text{f}^2}{\sin^2\theta'}\Big(1 - \frac{\cos^2\theta}{n_\text{f}^2}\Big)^2 = n_\text{f}^2\Big(1 - \frac{1-\sin^2\theta}{n_\text{f}^2}\Big) \\
&= n_\text{f}^2 - 1 + \sin^2\theta = \sin^2\theta - \sin^2\theta_\text{c}
\end{aligned} \tag{3.12}$$

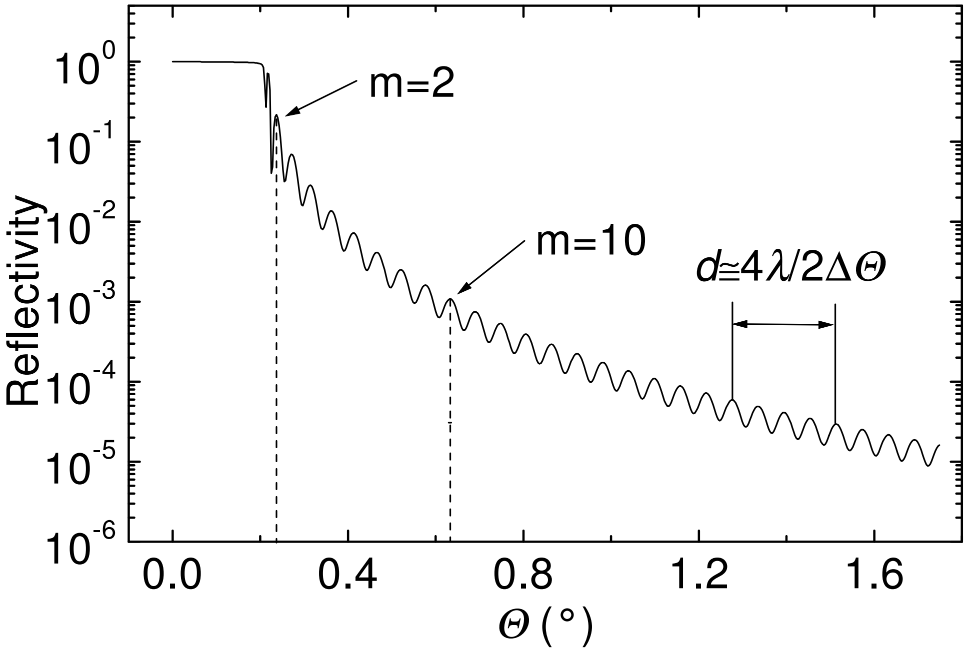

Figure 3.13: Attribution of fringe number to maxima in reflectivity interference pattern.

The third and the fifth step in this derivation follow by substitution of Eq. 3.10 and Eq. 3.11, respectively. Using Eq. 2.14 and 2.11, this can be finally rewritten as:

$$\sin^2\theta = \frac{m^2\lambda^2}{4d^2} + \sin^2\theta_c = \frac{m^2\lambda^2}{4d^2} + \frac{\lambda^2 r_0\rho_e}{\pi} \tag{3.13}$$

For angles $\theta \gg \theta_c$ the squared sine of the critical angle term can be neglected compared with the first term and we end up with the usual form of Bragg's law:

$$2d\sin\theta = m\lambda \tag{3.14}$$

Thus Bragg's law can be considered as a limiting form of the more general form represented by Eq. 3.13. If now the fringe number m (see Fig. 3.13) is plotted against $\sin^2\theta_m$, where θ_m is the position of the m-th maximum, a straight line should be observed with slope equal to $\lambda^2/(4d^2)$ and y-axis abscissa $\lambda^2 r_0\rho_e/\pi$ [26, 27]. From these two values the thin film parameters d and ρ_e can be calculated (see Fig. 3.14). It may be quite difficult to assign the proper index m to the observed intensity maxima, since especially the first maxima are obscured by the extremely rapid fall-off just beyond the critical angle.

A somewhat easier, but less accurate method to determine the layer thickness d is to use Bragg's law (Eq. 3.14) for intensity maxima well beyond the critical angle. Thus if the distance between two adjacent maxima is equal to $\Delta\theta$, then the layer thickness follows from:

$$d \approx \frac{\lambda}{2\Delta\theta} \tag{3.15}$$

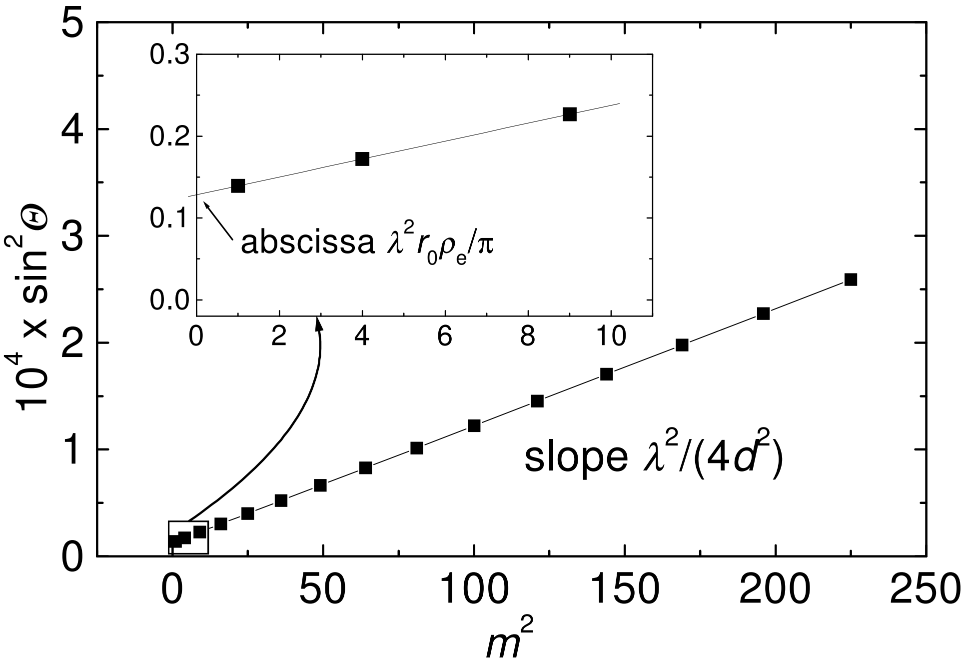

Figure 3.14: Plot of fringe position $\sin^2\theta_m$ versus the squared fringe number m^2.

A somewhat better estimation can be obtained by taking several fringes and dividing $\Delta\theta$ by the number of fringes (see Fig. 3.13). In this way no information about the electron density can be obtained but that information is approximately available by determining the critical angle (Eq. 2.14). Care should be taken in interpreting the electron density that is calculated from the value of the critical angle, since it represents some loosely defined average value of the electron density of the film and that of the substrate if the film thickness is too small (see section 3.1.2).

In more complicated cases, *e.g* multilayers, one has to rely on trial and error and/or least- squares. There is however still another method that can give some information on layer thicknes that may be used as starting parameters in the leas-squares analysis. This method is based on the Born approximation (Eq. 2.57) and is called the Fourier transform technique. What is in fact done is calculating the autocorrelation (or Patterson) function $P(z)$ of the derivative of the scattering length density profile:

$$P(z) = \int_{-\infty}^{\infty} \rho'(z')\rho'(z'-z)dz' = \int_{-\infty}^{\infty} \frac{r(k)e^{-ikz}}{r_F(k)}dk \tag{3.16}$$

where $\rho'(z)$ is the derivative of the SLD $\rho(z)$, and $r_F(k)$ the Fresnel reflectivity of the substrate. Thus the peaks of $P(z)$ at $z = z_i$ indicate the values of the layer thickness ($d_i = z_i$). It is noted that in general also the harmonics at $z_j = lz_i$ and sums of different harmonics $z_j = lz_i + mz_n$ with i, j, l, m, n integer are present, which could make the analysis difficult. In addition the peaks are not in good order; it is not known *a-priori* which d_j is adjacent to the substrate, for example.

3.3.2 Least-squares analysis

Least-squares analysis based on Parrat's recursive formula (Eq. 2.47) is still the mostly used method to determine the scattering potential from specular reflectivity data. Since Eq. 2.47 is highly non-linear, a non-linear minimalization routine has to be used, for example the Levenberg-Marquardt algorithm. Such an algorithm mimimizes a χ^2 merit function such as the sum of the squares of the differences of experimental and calculated reflectivities:

$$\chi^2 = \sum_{j=1}^{N} \Big[r_{\mathrm{exp}}(k_j) - r_{\mathrm{cal}}(k_j; S) \Big]^2, \tag{3.17}$$

where N is the number of data points k_j, $r_{\mathrm{exp}}(k_j)$ the experimental reflectivity at k_j, and $r_{\mathrm{cal}}(k_j; S)$ the calculated reflectivity at k_j using the set S of parameters that defines the model. The use of a non-linear minimalization routine implies that a starting set of parameters S_1 has to be defined, whose values are refined in the consecutive cycles of the algorithm. The starting set of parameters $S_1 = \{d_l, \sigma_l, \rho_l, l = 1..N+1\}$ is in general composed of N thickness, $N+1$ roughness and $N+1$ (scattering length, mass, electron or nuclei) density parameters, respectively for N layers with $N = 0, 1, \ldots$. The number of layers N to be used is normally not refined, but is fixed at the beginning. The reflectivity curve itself might give a clue of how to define N by visual inspection of the different oscillation periods. Alternatively, the auto correlation function (Eq. 3.16) can be calculated. This might give an *ansatz* for the thickness parameters as well. The density values must be set at some value that is in approximate agreement with what is *a-priori* known about the chemical composition. The roughness parameters are set at some reasonable value, say 0.8 nm.

Eq. 3.17 can be slightly modified to take into account experimental weight factors w_j for each data point j. A different type of weighting can be used to increase the influence of the low intensity data points at large k. This is important because otherwise these points will only contribute marginally to the merit function; their intensity can be 7 to 8 orders of magnitude lower than that around the critical angle. This different weighting is done by taking the logarithm of both r_{exp} and r_{cal}:

$$\chi^2 = \sum_{j=1}^{N} \Big[\log r_{\mathrm{exp}}(k_j) - \log r_{\mathrm{cal}}(k_j; S) \Big]^2, \tag{3.18}$$

After having defined the starting set of parameters S_1 the reflectivity is calculated using Parrat's recursive formula for each k_j and compared with the experimental data (Eq. 2.47). It might be necessary to adjust some of the parameters by hand. It is emphasized that the influence of the different parameters on the calculated reflectivity is not equal in each part of the measuring range. For instance, the influence of a change of the roughness becomes only visible for larger k-values. If the starting set of parameters is not close enough to the final model set, the minimalization routine might fail to converge to this set. For instance the refinement of the thickness parameter of a monolayer plus substrate system might easily fail if it is more than 5% wrong.

The first (and easiest) parameter to be refined or adjusted is in general the surface roughness parameter since this parameter defines the overall fall-off of the reflectivity. Then other parameters may be adjusted and/or refined. If the calculated reflectivity does not come into close agreement with the experimental data it might be necessary to change the number of stacks N_{L} that is used for the model. It is very difficult to give general guidelines how to perform such a change. If the calculated reflectivity drops much faster than the experimental one at the very end of the measuring range, it might be necessary to add a thin surface layer with reduced density compared to that of the bulk of the film.

For another case one might find that the calculated amplitudes of the interference fringes is significantly larger than that is observed experimentally, whereas the calculated and experimental critical angles are in good agreement. Now a thin reduced density layer at the substrate/film interface might be inserted. If this layer is thin enough it will not affect the calculated critical angle, but it may have an appreciable influence on the magnitude of the Kiessig fringes.

Having presented the least-squares procedures based on the exact Parrat formalism, we now give a simple iterative procedure [28–30] that is based on the expression for the reflectivity in the Born approximation (Eq. 2.56). A layer with unknown scattering length density on a substrate is considered. From the auto correlation function (Eq. 3.16) an initial value for the layer thickness is guessed and from the critical angle an average scattering length density (but see the remarks in section 3.1.1!) is obtained. These two parameters plus the SLD of the substrate constitute the model SLD profile, for which the derivative $\rho'_{\mathrm{cal}}(z)$ can be calculated. Using Eq. 2.56 a calculated reflectivity $r_{\mathrm{cal}}(k)$ is obtained. Denoting the real SLD derivative as $\rho'_{\mathrm{exp}}(z)$ and the experimental data as $r_{\mathrm{exp}}(k)$ two equations are obtained:

$$r_{\mathrm{cal}}(k) = \frac{\pi^2}{k^4}|\mathcal{F}[\rho'_{\mathrm{cal}}(z)]|^2, \tag{3.19}$$

and

$$r_{\mathrm{exp}}(k) = \frac{\pi^2}{k^4}|\mathcal{F}[\rho'_{\mathrm{exp}}(z)]|^2. \tag{3.20}$$

By dividing these two expressions, taking the square root, and multiplying the result by the Fourier transform $\mathcal{F}$ of the derivative of the model scattering length density $\rho'_{\mathrm{cal}}(z)$ the Fourier transform of the derivative of the actual electron density $\rho'_{\mathrm{exp}}(z)$ is obtained:

$$\rho'_{\mathrm{exp}}(z) = \mathcal{F}^{-1}\left[\sqrt{\frac{r_{\mathrm{exp}}(k)}{r_{\mathrm{cal}}}}\mathcal{F}[\rho'_{\mathrm{cal}}(z)]\right] \tag{3.21}$$

It is assumed in Eq. 3.21 that the phase corresponding to the actual reflectivity is identical to that corresponding to the model reflectivity. This is not true, ofcourse, and that is why Eq. 3.21 is applied recursively. The scattering length density $\rho'_{\mathrm{exp}}(z)$ obtained by Eq. 3.21 can be used for a new iteration by setting it to $\rho'_{\mathrm{cal}}(z)$, calculating a new reflectivity profile $r_{\mathrm{cal}}(k)$ and then applying again Eq. 3.21. It is hoped that $\rho'_{\mathrm{exp}}(z)$ converges towards the derivative of the real scattering length density $\rho'(z)$.

3.3.3 Model-independent fitting methods

The least-squares methods of section 3.3.2 might easily fail if the starting model is not close enough to the final model. Therefore the need arises for a more model-independent way of determining the scattering potential from the reflectivity data. Different methods have been proposed, based on either the Born approximation, distorted-wave Born approximation, or the exact formalism (Eq. 2.47). They still use least-squares or iterative methods, but the starting point is less essential or more easy to obtain. Their common point is that only one data set is necessary, but that the resulting scattering potential need not be unique, *i.e.* the phase problem is not rigorously solved using these approaches.

Methods that try to modelize a general scattering potential in stead of using a starting set S_1 of material parameters like density, thickness and roughness, expand the SP, or scattering length density, in a series of basis functions [4, 31]:

$$\rho(z) = \sum_{j=1}^{M} a_j f_j(z) \tag{3.22}$$

where the $f_j(z)$ are the basis functions and a_j the coefficients to be determined. The basis functions $f_j(z)$ are chosen as cubic b-splines or sine and cosine functions. Using Eq. 3.22 the reflectivity can be calculated using either the Born approximation (Eq. 2.57), the distorted-wave Born approximation (Eq. 2.61), or the exact dynamic formalism (Eq. 2.47). In the latter case the 'box' is divided into slices of equal thickness in which the scattering length density is taken to be constant. The starting coefficients a_j are usually taken such as to give a constant scattering lenghty density, either equal to that of the substrate or to what can be expected from the chemical composition. The a_j are refined by least-squares. The major advantage of a fitting procedure based on an expansion of the scattering potential compared to that described in section 3.3.2 is that now the number of stacks N is implicitly taken to be variable. Eq. 3.22 can describe any general scattering potential and it is hoped that the coefficients a_j converge such that the calculated reflectivity is in good agreement with the experimental data.

A method that is closely related to this general expansion method is based on an expansion of a variation of scattering length density with respect to a film of constant electron density. Quite often the assumption of a constant density gives a rather good fit to the experimental data, but details in the reflectivity indicate that the density $\rho(z)$ is not really constant, but that small variations $\Delta\rho(z)$ must exist with respect to an otherwise constant ρ_0. The overall scattering length density can thus be written as $\rho(z) = \rho_0 + \Delta\rho(z)$. The Fourier transform of the density variation $\Delta\rho(z)$ can then be written as [32]:

$$\Delta\rho(q) = \int_{-\infty}^{\infty} \Delta\rho(z) exp(iq)dz. \tag{3.23}$$

The thin film is divided in N slices $\Delta\rho_j$ of thickness d, so that Eq. 3.23 is written as:

$$\Delta\rho(q) = \frac{i}{q}\Big\{\Big(\sum_{j=2}^{N}(\Delta\rho_j - \Delta\rho_{j-1})exp(iq(j-1)d)\Big) + \delta\rho_1 - \delta\rho_N exp(iqNd)\Big\}. \tag{3.24}$$

This expression is inserted in the formula for the specular reflectivity in the DWBA, *i.e.* the squared modulus of the DWBA reflectance (Eq. 2.62):

$$r(k) = |iR_0 + \frac{2\pi r_0}{k}(a^2(k)\Delta\rho(q) + b^2(k)\Delta\rho^*(q))|^2. \tag{3.25}$$

The coefficients $a(k)$ and $b(k)$ of the substrate plus supposed constant density film can be calculated using tabulated values of the dispersion correction parameters f_j' and f_j''. Expression 3.25 is then used, along with expression 3.24 to fit, after convolution with the instrumental resolution function, against the experimental data, using the $\Delta\rho_j$ as fit parameters. As a starting point all $\Delta\rho_j$ are taken to be zero. The resulting $\Delta\rho_j$ are accordingly used in Parrat's recursive relation (Eq. 2.47 to calculate the reflectivity that is to be compared with the experimental data. The number N of slices to be taken depend on the resolution of the experiment (see also section 2.2.2). The thickness of the layer L must be known approximately. The number of slices follows then by $N \approx \text{nint}(2q_{max}L)$. Interfacial roughness of the film with constant density ρ_0 is not taken into account in deriving the two coefficients $a(k)$ and $b(k)$. The roughness redefines itself by proper values of the coefficients $\Delta\rho_j$.

3.3.4 Model-independent direct methods

The most modern methods to analyze specular reflectivity data use a completely different strategy than the methods described in the sections 3.3.2 and 3.3.3. They aim to directly calculate the scattering potential from the reflectivities that result from normally two different data sets without any fitting or iteration. The essential difference between these so-called inverse scattering (IS) methods and the traditional fitting methods is that the latter try to circumvent the phase problem (see section 2.3) by postulating either a physical/chemical model (section 3.3.3). or a mathematical model (section 3.3.4) of the SP. The phase and thus the reflectance R can be calculated using these model parameters and adjusted by least-squares or iteration.

IS methods on the other hand normally use a two-step procedure. The first step concerns the determination of the phase, either by performing a second measurement [33, 34] or in some cases by mathematical means (see section 4.3). In the second step the scattering potential is reconstructed from the reflectance data R, using mathematical methods that are deeply founded in one-dimensional quantum scattering theory [35, 36]. Thus no Fourier transform whatsoever is used to calculate the SP, but the SP is instead directly solved from the basic Schrödinger equation (Eq. 2.2): if the reflectance R and accordingly the wave function $\psi(k, z)$ is known, calculate the SP $V(z)$ can be derived in such a way that Eq. 2.2 is satisfied. Several solution methods exist for this problem and it has been proved that they can be applied using experimental data [37, 38].

The way how the phase is determined by performing a second data collection is based on a change in scattering length density contrast that can be created by different means. Either one changes the wavelength across an absorption edge of one of the constituting elements, or one may employ a reference layers whose scattering length density changes by applying or changing (the polarization of) a magnetic field or by simpliy removing it. One can also change the fronting or backing medium of the thin layer to be studied by changing, for instance, the relative concentrations of a H_2O/D_2O mixture [39]. The method is most easily explained for the first case, *viz.* the so-called anomalous X-ray reflectivity method [40].

Consider a thin film with unknown scattering length density profile on a substrate whose scattering lengh density can easily be changed in a known way by tuning the (synchrotron) wavelength to the absorption edge of one of its elements. Two measurements are performed of which one should be performed close to the absorption edge. A substrate that is very suitable is a Ge single crystal substrate whose K-edge is close to 11 keV. The same expression for the specular reflectivity in the DWBA as in section 3.3.3 (Eq. 3.25) is taken to obtain for each k two different reflectivities and two equations (3.25). From this set of equations the real and imaginary part of $\Delta\rho(k)$ can be solved. Finally $\Delta\rho(z)$ can be found from the complete set of $\Delta\rho(k)$ by an inverse Fourier transform.

Another application of anomalous or resonant X-ray reflectivity is the determination of the chemical composition of a thin film [41]. The idea is as follows. The electron density ρ_e can be expressed in terms of partial (atomic) number densities $\rho_{\mathrm{n},j}$ (see Eq. 2.10):

$$\rho_\mathrm{e} = \rho_\mathrm{n} \sum c_j (Z_j + f'_j - i f''_j) = \frac{\rho_\mathrm{m} N_\mathrm{A}}{\sum c_j A_j} \sum c_j (Z_j + f'_j - i f''_j) = \sum \rho_{\mathrm{n},j} (Z_j + f'_j - i f''_j) \tag{3.26}$$

The partial number density $\rho_{\mathrm{n},j}$ depends only on the space coordinate z; the scattering dispersion factors f'_j and f''_j depend only on the X-ray wavelength λ. Thus for two different wavelengths λ_1 and λ_2 two equations can be written:

$$\rho_{\mathrm{e}}(\lambda_1, z) = \sum \rho_{\mathrm{n},j}(z)(Z_j + f'_j(\lambda_1) - if''_j\lambda_1), \tag{3.27}$$

and

$$\rho_{\mathrm{e}}(\lambda_2, z) = \sum \rho_{\mathrm{n},j}(z)(Z_j + f'_j(\lambda_2) - if''_j\lambda_2), \tag{3.28}$$

The two different electron densities $\rho_{\mathrm{e}}(\lambda_1, z)$ and $\rho_{\mathrm{e}}(\lambda_2, z)$ can be determined using, *e.g.*, non-linear least-squares on Parrat's recursive relations. The scattering dispersion factors $f'_j(\lambda)$ and $f''_j\lambda)$ can be looked up, so that in the case of a binary compound AB, the number densities $\rho_{\mathrm{n},A}(z)$ and $\rho_{\mathrm{n},B}(z)$ can be calculated. It is noted that the two Eqs. 3.27 and 3.28 are even overdetermined with respect to the number of parameters to be determined. The equations are complex with a real and imaginary part each. So in fact there are four equations for two parameters to be determined. If it is *a-priori* known or assumed that the density is independent of z, then the chemical formula can be determined in this way. The method is the more accurate the more the two electron densities $\rho_{\mathrm{e}}(\lambda_1, z)$ and $\rho_{\mathrm{e}}(\lambda_2, z)$ are different. For a ternary compound, three different wavelengths should be selected with three distinct electron densities. Electron densities can vary rapidly in the vicinity of absorption edges, so that there the wavelengths should be selected. The drawback is that the dispersion factors $f'_j(\lambda)$ and $f''_j\lambda)$ are much less known, and that they vary as well in a beam with a small wavelength dispersion. A solution is to perform one or more data collections at wavelengths well away from the absorption edges with well-known dispersion factors [41]. In this case dispersion factors can be determined as well.

Chapter 4

Case studies

Three different case studies will be presented that may give an impression of some applications of grazing incidence specular reflectivity. The examples are from the author's laboratory. A good source of state-of-the-art applications in specular reflectivity and related surface scattering techniques can be found in the proceedings of the biannual International Conferences on Surface X-ray and Neutron Scattering that are published as regular volumes of the journal *Physica* [42]. Some highlights will be mentioned here to give an impression of the wide field of applications of XR and NR.

Surfactants and proteins Penfold *et al.* [43, 44] studied the adsorption of (mixed) surfactants at the liquid-solid interface by means of time-of-flight NR. The adsorption of surfactants is important for many technological and industrial applications. The authors were able, by using different isotopic labeling of the surfactant and solvent to determine the structure and composition of mixed cationic and non-ionic surfactant layers at the hydrophilic silicon surface. It was shown how a change in the solution pH drastically changes both the structure and the composition of the surfactant layer and that the surface composition is different from the bulk composition. In another study, the structure was investigated of the milk protein β-casein adsorbed on a chemically modified hydrophobic silicon (111) surface [45]. A two-layer structure of β-casein was proposed to explain the neutron reflectivity curves resulting from solutions with different isotopic compositions. The structure layer adjacent to the surface is dense and 23 Å thick, whereas the layer adjacent to the solution is 35 Å thick and has only 12 percent protein volume fraction. This particular structure can be explained in terms of the charge distribution within the protein.

Polymers Vignaud *et al.* [46] performed specular XR measurement on series of symmetric PS/PBMA diblock copolymers deposited on silicon substrates. It was shown how annealing these films induces a lamellar ordering within the film which in turn leads to the formation of holes or islands at the surface of the film. Apart from the total thickness of the film, the height of the islands could be determined as well. By measuring the thickness values as a function of annealing time information could be found on the kinetics of the ordering. An overview of the use of XR and NR for polymers is given by Russell [47].

Semiconductors Edwards *et al.* studied the 7×7 buried Si(111)-Pb interface by XR and X-ray diffraction [48]. This interface has received much attention because of the discovery that the Schottky barrier height of diodes grown on different Si(111)-Pb interfaces depends on how the silicon surface is reconstructed [49]. It appeared that at low coverages the Pb layers are disordered, but that after a coverage of 6 monolayers the growth Pb grows layer-by-layer according to Pb(111) lattice planes. The difference in Schottky barrier height seems to be related to details in the interfacial structure. It is noted that XR and more general X-ray scattering are the only techniques that give access to the structure of these buried interfaces.

Thin film growth Lee *et al.* used *in situ* fixed angle XR to measure the surface roughness, density and thickness evolution of an amorphous $LaNiO_3$ film as a function of magnetron sputtering deposition time [50]. In this experiment the sample and detector position were held fixed at a certain position, unlike in a traditional fixed-wavelength XR or NR experiment. The intensity at this position was monitored during the deposition process. What was observed was an oscillating intensity as the deposition proceeds. From this oscillation pattern information information could be obtained on the growth mechanism. The mechanism proposed bears some resemblance to the one discussed in section 4.1 (and references therein).

Anomalous X-ray reflectivity By a combined use of neutron and X-ray reflectivity Findeisen *et al.* were able to determine the hydrogen concentration and mass density of diamondlike carbon films. The amount of hydrogen incorporated in this type of films has important impact on the desired physical properties, as hardness and thermal conductivity. Reflectivity is the only accurate non-destructive technique to determine the hydrogen concentration in these films. Normally only the scattering length density or the mass density can be obtained by a single reflectivity data collection (Eq. 2.14). If, however, a second reflectivity experiment is performed for which the elements have a different response to the radiation, then additional information becomes available, like the chemical composition. A different response can be realised by selecting another wavelength (anomalous X-ray reflectivity, see section 3.3.4) or by using neutrons. In the latter case neutrons are the obvious choice. Assuming that the film density was constant throughout the thin film, the authors were able to determine hydrogen concentrations within an accuracy of 1.5%. It is noted that ordinary hydrogen was used in the neutron experiments and not deuterium. The scattering length of deuterium is 0.6674×10^{-12} cm, to be compared with 0.6648×10^{-12} cm for carbon, *i.e.*, there is only a very small contrast between carbon and deuterium. On the other hand, if hydrogen is used (scattering length -0.37409×10^{-12} cm), the contrast is significantly enhanced.

The first two examples that are presented below show how XR can be combined with other microscopic and spectroscopic techniques to obtain a detailed picture of the thin film under study. The last example is on a new and advanced method to extract the scattering potential of a thin film using specular reflectivity data.

4.1 Study of the growth mechanism of Si on SiO_2

This study was undertaken by means of XR in conjunction with atomic force microscopy (AFM) and scanning tunneling microscopy (SEM) to get a better understanding of the growth of Si on SiO_2 [52]. Si was deposited on top of 70-90 nm thick silica layers on Si(001) wafers by LPCVD (Low Pressure Chemical Vapor Deposition), keeping all external reactor conditions fixed except the deposition time. In this way 8 Si layers from 4 to 500 nm were grown. Fig. 4.1 gives the reflectivity of these 8 samples. The first 6 samples show two types of fringes with different oscillation periods. From the oscillation periods values can be deduced for the thickness of the silica and the silicon layer. If the thickness of the two different layers becomes close to each other, *e.g.*, for the 75.5 nm thick Si layer, it might be quite difficult to differentiate with precision between the two layers. For the thickest layers it becomes impossible to determine the exact thickness of the different layers due to the smoothening caused by the instrumental profile function and/or interfacial roughness. In this case one has to rely on the (less precise) values extracted from cross-sectional SEM images.

It is more important in the context of a study of the growth mechanism of thin films to have accurate values for

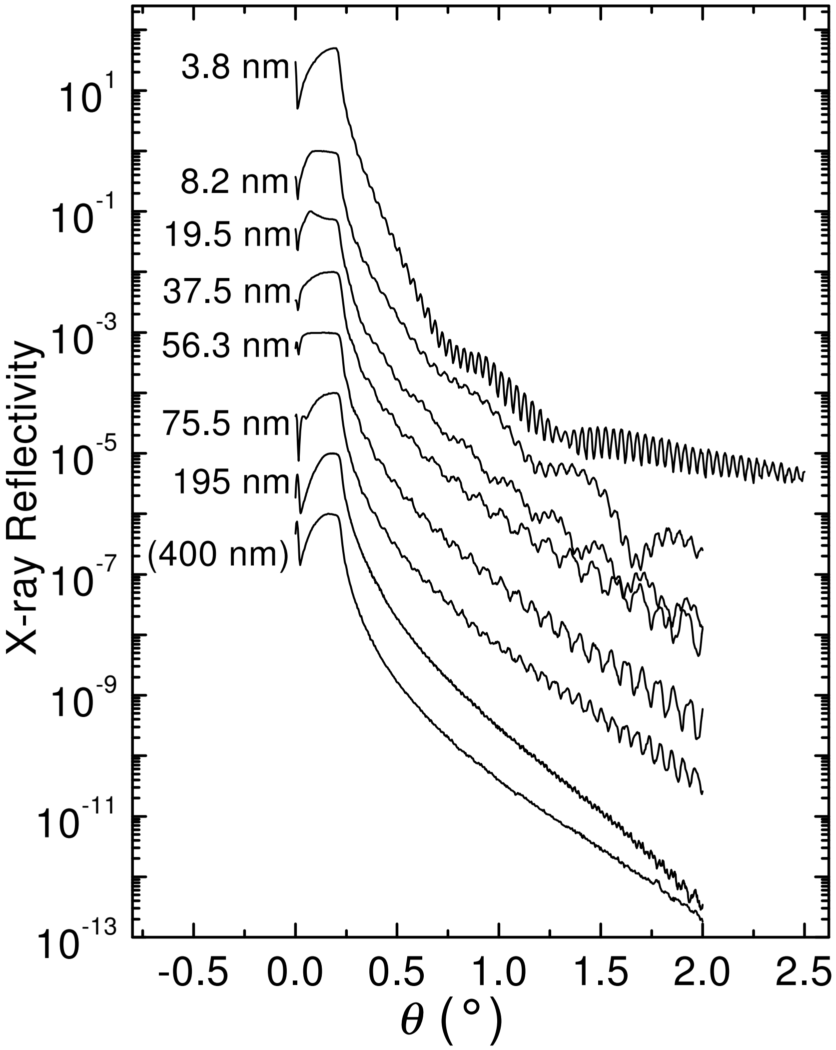

Figure 4.1: Experimental X-ray reflectivity of 8 different Si layers on SiO$_2$/Si substrates.

the surface roughness, since this parameter is very important in many atomic growth theories. In this respect it is very instructive to compare roughness values from XR with those calculated from AFM images. If these values are not the same it gives additional information on the nature of the surface roughness. If the AFM value is smaller than the XR value it might indicate that roughness is predominant on a very short length scale (say below 10 nm), since AFM is not sensitive for lateral variations below the width of the tip [53]. XR is only limited by the wavelength of the radiation, typically 0.15 nm. If on the other hand, the AFM value is larger than the XR value, it might indicate that the surface is rather inhomogeneous. This is immediately detected by a local technique like AFM, whereas the global, averaging nature of XR does not take into account these inhomogeneities. Fig. 4.2 shows the XR and AFM surface roughness as a function of deposition time. It can be seen that the AFM-roughness has a maximum whereas the XR-roughness only decreases. The very pronounced maximum of the AFM roughness is related to spatial inhomogeneities in the form of crystalline silicon islands growing on top of the surface. These islands are approximately as high as the Si layer itself.

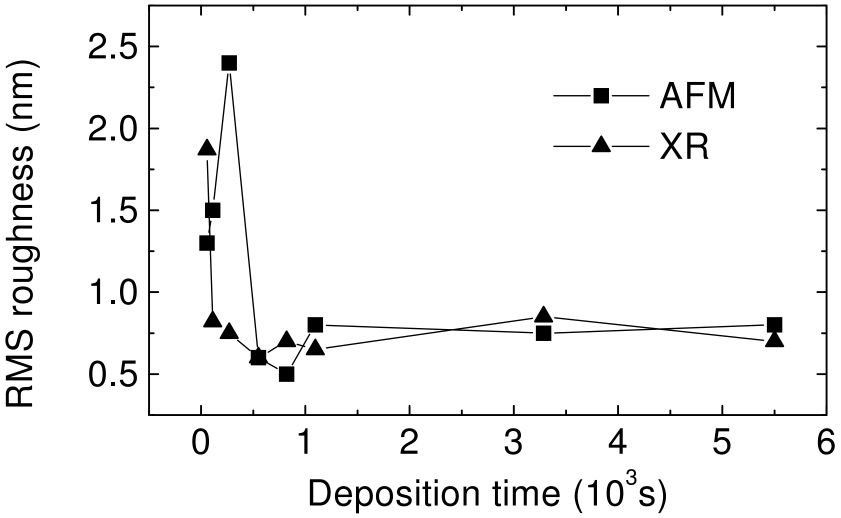

Figure 4.2: AFM- and XR-deduced roughness values for Si on SiO_2/Si substrates versus the deposition time.

The XR-roughness corresponds roughly with a so-called background AFM-roughness that is calculated by discarding the height variations of the islands. It is noted that the islands tend to decrease in height and number density and to increase in width as the deposition proceeds. The actual AFM surface roughness behavior (*i.e.*, a maximum for low deposition times and a levelling-off towards larger deposition times) can be modeled in a qualitative way by a simple nucleation-coalescence model [54].

4.2 Structural changes in hybrid organic/inorganic thin films

The structural evolution of thin films that were prepared using PECVD (Plasma Enhanced Chemical Vapor Deposition) as a function of plasma conditions (mixture of O_2 and TEOS: tetraethoxysilane) was investigated using different characterization techniques like X-ray reflectivity, X-ray photon electron spectroscopy and UV-visible spectroscopic ellipsometry [55]. Fig. 4.3 gives the X-ray reflectivity as a function of the TEOS volume fraction τ in the O_2/TEOS gas mixture. All other reactor conditions were kept the same. The inset shows the evolution of the reflectivity around the critical angle on a linear scale. It is seen that for high τ there are effectively two critical angles. The lower critical angle corresponds to the density of the thin film, whereas the higher critical angle is the signature of the substrate density (silicon). For low TEOS volume fractions there is only one critical angle that roughly corresponds to the substrate density. The fact that there is only one critical angle could be due to either a thinner film with the same low density, or to a higher film density with a equally thick film. The latter is the case as is demonstrated by the period of the interference fringes. It is noted that the presence of two critical angles is a pure absorption phenomenon that would not have been observed in the case of neutron reflectivity (see section 3.1.1). Fig. 4.4 shows the results of a fit using Parrat's recursive algorithm against the experimental data for the $\tau = 0.5$ sample. The merit function that is used in the least-squares procedures is based on the logarithm of the experimental and calculated reflectivity, rather than on the reflectivities themselves, since this gives an increased weight to the data points at large angles and a more equal sensitivity of the

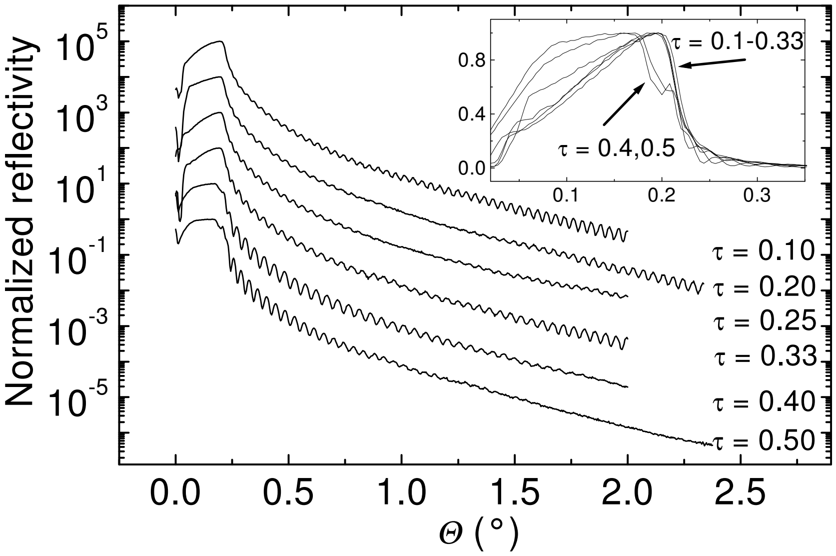

Figure 4.3: Experimental X-ray reflectivity of 6 different TEOS-films on Si substrates.

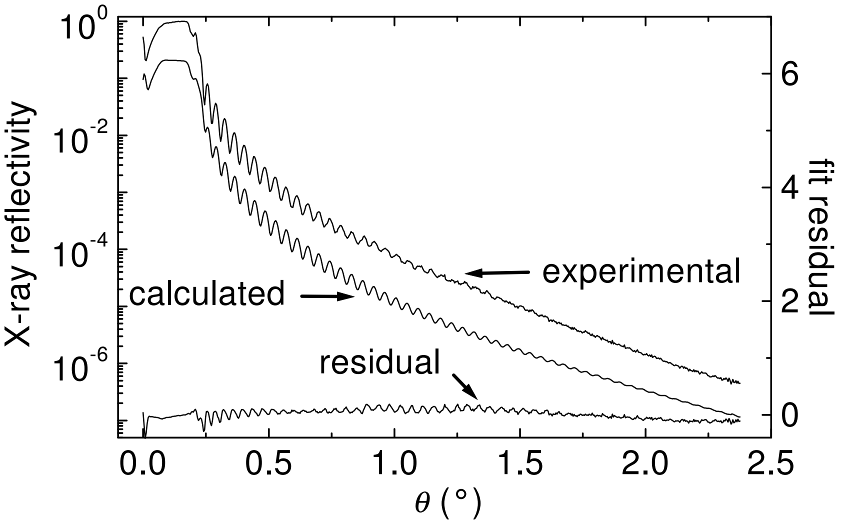

Figure 4.4: Experimental and calculated X-ray reflectivity of the TEOS $\tau = 0.5$ sample along with its fit residual.

minimalization procedure to all parts of the data interval. The lowest curve in Fig. 4.4 gives the residual η_i of the fit: $\eta_i = ^{10}\log r_{\mathrm{exp,i}} - ^{10}\log r_{\mathrm{cal,i}}$.

The rather abrupt decrease of the mass density of the thin film can be correlated with other structural characteristics as evidenced by, *e.g.*, spectroscopic ellipsometry and Rutherford backscattering (RBS). Fig. 4.5 shows the evolution of the film density and the visible light refractive index versus the TEOS volume fraction. The inset shows the carbon content as determined by RBS. All graphs show the same abrupt change for $0.33 < \tau < 0.40$. From this (and

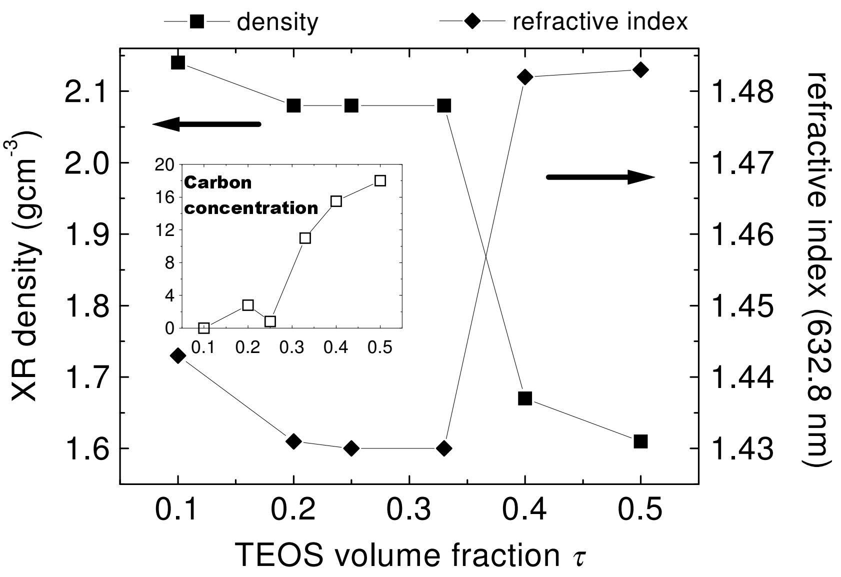

Figure 4.5: Evolution of the density and visible light refractive index versus the TEOS volume fraction τ. The inset shows the carbon concentration (in 10^{21} at/cm^3) as determined by Rutherford backscattering.

additional X-ray photoelectron spectroscopy and Fourier transform infrared spectroscopy measurements [55]) it can be deduced that the structure of the film evolves from a inorganic silica type framework towards a hybrid inorganic/organic framework.

Another way of tuning the structural properties of these thin films is by changing the plasma conditions inside the reactor [56]. The plasma conditions are characterized by the composite parameter $\xi = V/F.M$, where V is the input voltage, F the input gas flow rate, and M the molecular weight of the gas species. The larger ξ, the more energetic the plasma is. Thin films were deposited using different organosilicon precursors like the linear monomer hexamethyldisiloxane (HMDSO) and the cyclic monomer octamethylcyclotetrasiloxane (OMCTSO). The plasma was conditioned by varying the monomer flow rate F. The mass density was determined using XR and the organic character of the thin films notably by Fourier Transform Infrared Spectroscopy (FTIR). Fig. 4.6 shows the evolution of the density and the organic character of the films versus the plasma parameter ξ. The parameter ν characterizing the organic character was defined as the ratio of the intensity of a vibrational peak due to a typical organic group like Si-CH$_3$ and that of the intensity of a peak due to a typical inorganic group like Si-O. It is seen that as the plasma parameter ξ increases, the films become denser and more 'inorganic'. It was shown as well that the gas permeation properties of these films are nicely correlated with the plasma parameter ξ and accordingly with the structural properties as evidenced by XR and FTIR [56].

4.3 *Ab-initio* determination of scattering potentials

It is shown here that logarithmic dispersion relations (LDR's) may be used in a number of cases to calculate the phase belonging to the reflection amplitude without having to rely on a *a-priori* model [57–59]. The scattering potential (SP) is

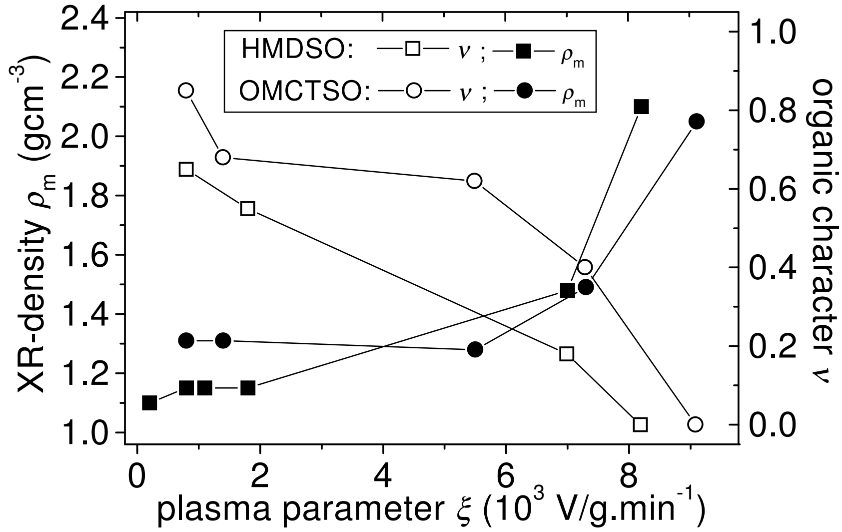

Figure 4.6: Evolution of the density and organic character ν of thin films deposited from the HMDSO and the OMCTSO precursors.

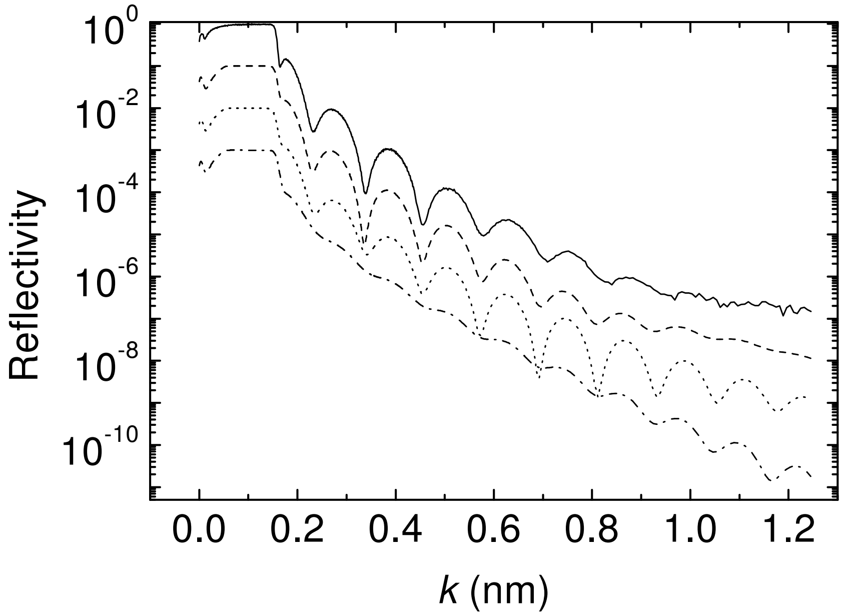

Figure 4.7: Experimental X-ray reflectivity of a nominal 25 nm thick carbon film on a Si substrate (solid line) and calculated reflectivities using a two-layer model (dashed line) and two different one-layer models (dotted and dashed-dotted, respectively).

subsequently calculated from the complex reflectance data by so-called Inverse Scattering (IS) methods that were already mentioned in section 3.3.4. Logarithmic dispersion relations are directly connected to the Kramers-Kronig relations that are well-known in optics. Kramers-Kronig relations are Hilbert transforms that connect the real and imaginary part of a susceptibility function whose response function satisfies the causality condition. In the time domain this means that the response comes after the action. In reflectivity it simply means that the scattering potential is zero outside the system to be studied, in other words, that the scattering object is finite. The Kramers-Kronig relations transform in logarithmic dispersion relations when the phase and amplitude are connected rather than the real and imaginary part of the susceptibility. It is noted that Kramers-Kronig relations are of no use in crystallography, because there the scattering object can be regarded, to a very good approximation, as being infinite. There is, however, apart from the finiteness of the scattering object, a second requirement for the LDR in order to be applied. The (analytically continued) complex reflectance R must not have zero's in the upper half of the complex plane (UHP). Some scattering potentials have a reflectance with zero's in the UHP, others have zeroless R. It is not clear what the physical reason is of this different behavior. These zero's give an additional phase factor to the phase determined by using the LDR; this factor can be calculated if the positions of the zero's is known. So in order to be able to apply the LDR directly, it must be known in advance whether the reflectance belonging to the SP has zero's in the UHP or not. This is of course impossible, because it is the SP itself that is to be determined using specular reflectivity. So at first sight LDR's are of little use in experimental reflectivity. Fortunately classes of SP's can be determined having zeroless R in the UHP. Therefore it must be known beforehand only *approximately* how the shape of the SP is in terms of layer thickness and/or density. Then the LDR can be used to calculate the phase. Of course this way of determining the phase cannot give an unambiguously unique SP, since although the *estimated* SP might be within the class of allowed SP's (with zeroless R in the UHP), the *real* SP might fall outside this class. It is nevertheless possible to use the LDR in certain cases as an aid to get a proper starting model for traditional fitting methods. Traditional fitting methods, *i.e.*, those based on Parrat's recursive algorithm, have the disadvantage that they become readily quite cumbersome, except for the very simple cases, *e.g.*, a single layer on a substrate.

The example that is given here demonstrates that the LDR is able to give a clue where the SP deviates from that of a single layer on a substrate [60]. Whereas it is was impossible to find a correct fit to the experimental data, the LDR gave immediately the hint how to parameterize the SP properly. This was possible because the system under study was a nominally 25 nm thick carbon film on silicon. Using this nominal value and the theoretical value of the density of carbon it could be anticipated that the SP of carbon on silicon was within the class of admissible SP's for zeroless R. Fig. 4.7 shows the experimental reflectivity (solid line) along with three different single and double layer models. The dashed-dotted line corresponds to the best fit assuming a single layer model while keeping the carbon density fixed at the theoretical value. It appears that the fringe contrast of the calculated reflectivity is much less than that of the experimental curve. The scattering potential from this model is shown as a dashed-dotted curve in Fig. 4.8. Then the carbon density was taken to be an independent variable in the fitting procedure. The reflectivity that corresponds to the best model from this fit is the dotted curve in Fig. 4.7, and the model itself the dotted line in Fig. 4.8. Now the calculated fringe contrast is much stronger, but is in fact too strong compared to the experimental contrast. Finally the calculated SP (solid line in Fig. 4.8) using the phase derived from the LDR was parameterized in terms of a two layer model and this was used in a traditional fitting procedure. The dashed reflectivity curve in Fig. 4.7 results and is in close agreement with the experimental data. The most important feature of the in this way derived SP is the density depleted zone at the film/substrate interface. This can be related to the low adherence of such a carbon film by the formation of hollow voids

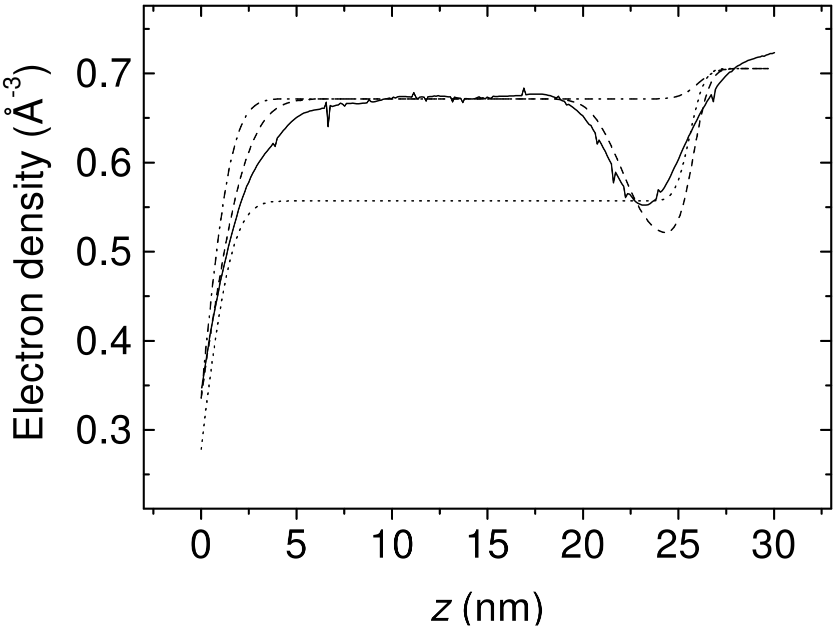

Figure 4.8: Electron density profiles corresponding to an *ab-initio* calculation using PIS methods (solid line), a two-layer model (dashed line), and two different one-layer models (dotted and dashed-dotted, respectively).

at the substrate/film interface (see, *e.g.*, ref. [61]). It is interesting to note that the plateau of the *ab-initio* determined SP (solid line in Fig. 4.8) is very close to the theoretical value (dashed-dotted line) whereas the value that is obtained after letting it free in the fitting procedure (first plateau of the dotted line) is very close to the minimal value of the *ab-initio* derived SP at the substrate/film interface.

The present method plays a complementary role to traditional fitting methods, in the sense that no unambiguously unique SP can be derived. The methods to derive un unambiguously unique SP using specular reflectivity data are under full development now (see also section 3.3.4), but they always require two different data collections to be done. At the moment only successful neutron experiments have been reported [37, 38].

4.4 Data reduction practice in X-ray reflectometry

Data reduction practice in X-ray reflectometry is described. The several approaches for applying certain corrections, such as background subtraction, geometrical effects and normalisation, are compared and discussed. Two widely employed setups, one with beam knife edge and one without, are compared with respect to a number of corrections to be applied.

4.4.1 Introduction

Grazing-incidence reflectometry using neutrons or X-rays is nowadays a well-established technique for the study of nano-scaled structural properties of thin films using high-intensity sources at synchrotrons or neutron reactors, but also using laboratory X-ray equipment thanks to the rapid development of new optical devices such as bent multilayers [5, 6, 10, 62]. A complete diffraction or diffusion study normally comprises four stages. The first stage concerns the setup of the experiment, *i.e.* the exact conditioning of the sample within the center of the goniometer and the selection of the proper data collection parameters, and subsequently the measurement itself. This step is followed by the data reduction, *i.e.* the conversion of the raw data files into one or more reduced files that are suitable to be compared with theory. This data reduction takes into account all possible corrections due to the experimental setup and the direct environment. The third step concerns the resolution of the so-called phase or inverse problem, which is due to the fact that only the squares of the amplitudes of the scattered waves are measures and not their amplitudes. Once a phase-model is found, the structure can be refined to result in a model which is maximally compatible with the experimental data.

Whilst these four steps are well-known and have been amply described in the fields of single-crystal [63] and powder diffractometry [64], they have been thus far nearly neglected in X-ray and neutron reflectometry. Most emphasis in this field has been paid to the solution of the phase problem, probably because it has some essential differences with that in single-crystal and powder diffractometry. Firstly because the latter diffusion techniques are kinematical in nature while the first is dynamic, but also - more importantly - because a thin film plus substrate system is considered to be semi-infinite, while single crystals are considered to be infinite, which makes that their diffusion pattern is discrete in contrast with that of the thin film plus substrate system which is continuous. This implies that structure solution methods developped for single-crystal or powder crystallography are not directly transferable to thin film reflectivity.

Experimental setup and data reduction for reflectivity experiments are in contrast not well discussed in the open literature, possibly because they are considered to be not too different from that used in single-crystal diffraction and especially powder diffraction [65]. Indeed, a normal well-aligned powder diffractometer could be used with some slight adaptions for a reflectivity experiment, but some details differ considerably from those in powder diffraction. The data reduction step is even more different than that in powder diffraction, but details on how this important step is done are nearly always lacking in studies reporting on reflectivity experiments. It appears that nearly each laboratory working in this field has developped their own methods and data reduction programs, without a common adopted practice, such as is used in the singel-crystal community. Only one frequently cited paper is known which reports on geometrical corrections for reflectivity analysis [20] but this concerns only one aspect of the data reduction process and this becomes only important when the correction extends beyond the angle of critical reflection.

This paper is an attempt to describe common data reduction practice in X-ray reflectometry using point detectors. Data reduction practice in neutron reflectometry is explicitly excluded, since the differences with the practice for X-rays are too large. Note, however, that some of the ideas developped here will be applicable as well for single-wavelength neutron reflectometry. Some words will be dedicated to data collection strategy, since that will influence obviously the way how the raw data are reduced.

4.4.2 Data collection strategy

An important difference with the practice in single-crystal and powder diffraction is the very large counting range in reflectometry; the latter spans 7 to 8 decades for well designed laboratory experiments and 8-10 decades for synchrotron measurements. The reason is that the reflectivity varies approximately with $1/q^4$, where $q = 4\pi \sin\theta/\lambda$ is the momentum transfer, and in order to measure the thickness of films of several nanometers thick a large momentum range must be measured with a large counting range, since only a limited number of widely-spaced fringes is encountered. Also in order to accurately measure the roughness parameters or to increase the accuracy of the thickness parameter of thicker samples a large momentum transfer is necessary. Therefore the data collection strategy in reflectivity is important in order to avoid that the total measurement time becomes prohibitively long. It is noted for what follows that this aspect is considered to be more important than designing the most optimal experiment based on counting statistics. The largest source of error in a diffusion experiment is in general not the counting variance, but rather the counter mis-positioning [66], or for multi-detector array experiments the non-integral number of steps between the detectors. A variable counting time and step width experiment is designed during a relatively fast pre-experiment in order to select the optimal experimental parameters. The optimal counting time for a certain angular value is such that at least 1000 counts for each measured point are collected. This assures that at least the counting variance is not the limiting factor in the overall accuracy of the experiments, since the experimental standard deviation for all points of the total interval is in this way lower than approximately 3% (based on Poisson statistics where the experimental standard deviation of N counts is $\sqrt{N}$ counts). Instead of a varying step time also attenuators of different thickness can be used: their insertion or redrawal can be automatic or manual and data collection software can or cannot automatically recalculate the corrected intensity. In the most general case both attenuators and variable step time will be used.

The step width should be chosen in such a way that all details in the reflectivity curve are sufficiently well resolved. A rule of thumb is that in order to resolve an interference (or Kiessig) fringe sufficiently well at least 8-10 points should be measured. Using less points will result in fringes that cannot be well modeled, more points results in redundant information. It is noted that the number of points per fringe that is taken may depend on the step counting time; a short step counting time requires more points to be measured of the fringe, whereas a high counting rate needs less points in order to model the fringe correctly [67]. The step width is allowed to vary for several reasons. Firstly the fringe spacing for a homogeneous single layer is not strictly constant throughout the measured data interval due to dynamic effects, *i.e.* due to refraction at the interfaces. Moreover, the fringes have a tendancy to attenuate or even disappear at high angles, which makes it possible to use there a larger step width. Thirdly the change in intensity is very abrupt around the critical angles(s) of total external reflection, which can only be accurately measured by taking a very small step width in that region. The choice of the step width is very delicate if more than one layer is present; it cannot be simply based on the width of some fringes in the reflectogram. Instead a very small step should be used to be able to resolve the details of overlapping of fringes due to the different thicknesses.

When the afore-mentioned points have been taken into account a multi-interval data file results which should be put on a common scale and possibly a common step width in order to be able to use the different fit and refinement programs that do not allow always to have a variable step width. Also different corrections should be applied in order to compare the experimental curve with the simulated curve.

4.4.3 Data reduction

The data reduction falls into several independant stages, some of which are closely connected with the way the measurements have been done and the exact experimental setup. Most of the stages are typical for X-ray reflectometry measurements.

4.4.3.1 Background determination

The determination of the background in reflectometry is completely different with respect to that in single-crystal or powder diffraction. In single-crystal diffraction it is nowadays usually done using learned-profile determinations, whereas in powder diffraction the background is considered to be an integral part of the scanned pattern and modeled using several mathematical functions such as Chebyschev series or cosine Fourier series. In reflectometry the background is measured separately (except when area detectors are used), since the measured signal in the specular condition consists of the true specular signal plus the background, where the background originates from different sources, such as detector noise, air scattering, or sample related diffuse scattering. Subtracting the background is important since it affects the values of the roughness parameters determined from the experiment. There are in general two methods to measure the background. The most popular method is probably to perform a so-called ”off-set” scan, *i.e.* the signal is measured just parallel to the specular ridge. In an angular-dispersive experiment the off-set scan consists in doing a so-called $\theta + \delta(\theta)/2\theta$ scan. Fig. 4.9(b) depicts how the scan is performed in momentum space: the scan subtends an angle of $\delta(\theta)$ with the specular scan. This shows immediately the disadvantage of this type of scan for background determination, because it is not strictly parallel to the specular ridge, but starts to deviate more and more at higher angles. The choice of $\delta(\theta)$ is of course also arbitrarily. It is in general determined by performing several rocking or transverse scans, *i.e.* keeping the detector fixed while rocking the sample through the specular ridge, and setting the optimal value for $\delta(\theta)$ as the point where the background is believed to start. The off-set scan is inevitably a low-intensity scan; in order to have sufficiently accuracy rather long counting rates should be employed. As a general rule the off-set scan takes as much time as the specular scan, but has less precision.

A second method for determining the background consists in performing rocking scans at regular points along the specular ridge (see Fig. 4.9(c)), fitting the rocking curves with e.g. a gaussian profile and using the thus determined background parameters for the correction of the measured signal in order to obtain the true specular signal. The true specular signal is subsequently used for data fitting. The advantage of this method over the off-set scan method is that there is not an arbitrary and fixed $\delta(\theta)$ parameter, and that the determination of the background level itself is more accurate since more than one point is taken to determine it. The disadvantage is that usually not for each data point on the specular ridge the rocking curve can be measured since this will be prohibitively long. Several points along the

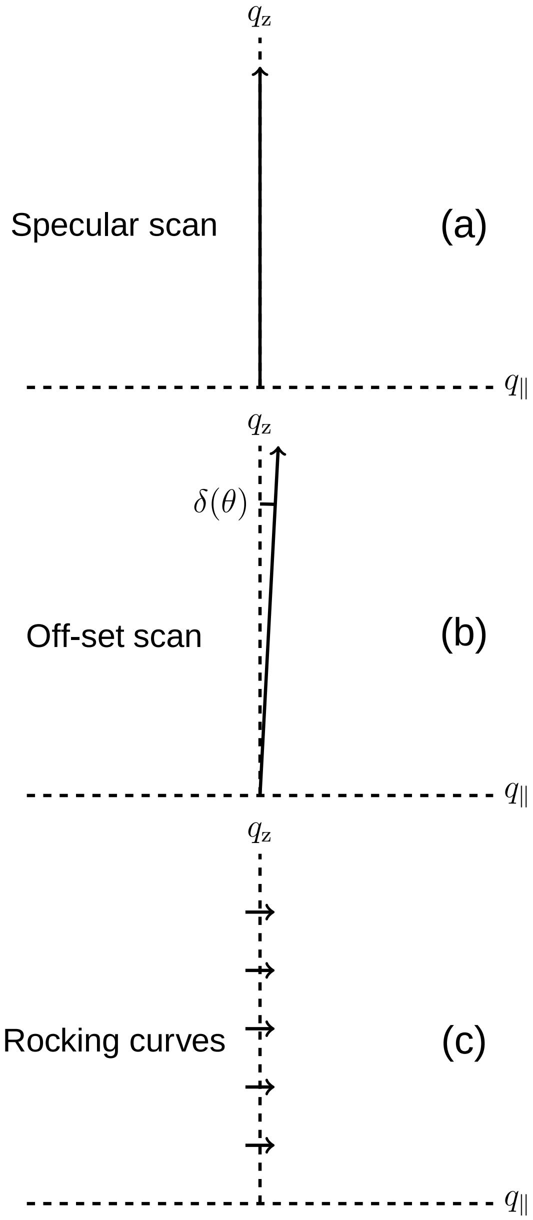

Figure 4.9: Scan directions in momentum space for specular scans (a), off-set scans (b), and rocking curves (c).

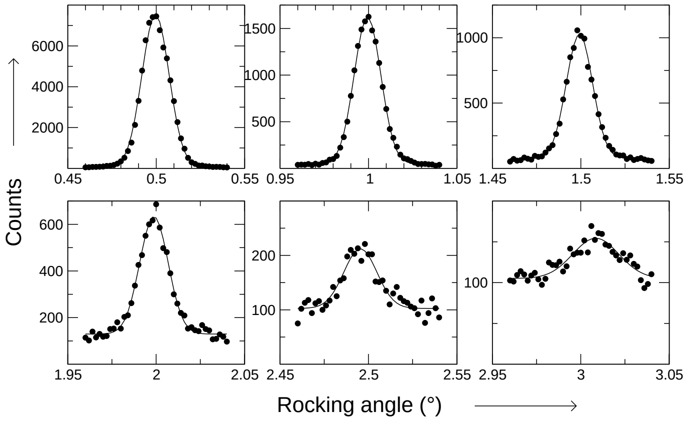

Figure 4.10: Rocking curves for background determinations along with the their fits (solid lines) using gaussian functions.

specular ridge are taken, such that the total duration of the background determination equals approximately the duration of the measurement of the specular signal.

In order to compare the two background determination methods measurements were carried out on a thin amorphous carbon layer obtained by Ionised Physical Vapour Deposition on a silicon (001) wafer at a pressure of 50 mTorr and a target RF power of 150 W; the nominal thickness was 50 Å, but turned out to be 88 Å after data fitting. Data were obtained using a Bruker D5000 diffractometer using graphite monochromatized Cu-$L_{3,2}$ radiation and a special reflectivity stage which consists essentially of the afore-mentioned beam-knife edge. The central slit was set at 20 μm. The data collection strategy was as outlined in section 4.4.2, but it has to be noted that the requirement of having at least 1000 counts per data point could not fully be maintained for the background determinations. The maximum counting time allowed by the software, 650 s, can be extended by measuring the same data point twice or thrice and then summing up the counts, but this is not always desired because the mechanical and thermal stability of the goniometer are not garantueed for such large counting times. The off-set scan was started at $2\theta = 0.50^\circ$ with an off-set of $\delta(\theta) = -0.03^\circ$ and the first rocking curve at $2\theta = 1.00^\circ$. Corrections below these values were extrapolated to zero. Fig. 4.10 shows that the fits to the rocking curves assuming a gaussian profile shape are good enough to obtain a rather accurate determination of the background level, even if the background variance is rather high. The off-set scan and the specular reflectivity scan are shown in Fig. 4.11; the off-set scan follows nicely the fringes in the specular scan and the two curves approach each other at high angles. Fig. 4.12 shows the background levels expressed as a fraction τ of the *measured* specular signal r_{meas} for the two methods. The true specular signal $r_{\text{spec,true}}$ is then simply obtained as $r_{\text{spec,true}} = r_{\text{meas}}(1 - \tau)$. Correction factors τ for those θ values for which no rocking curve were measured were determined by linear interpolation between the two neighbouring θ values for which the rocking curves were measured.

The background level determined from the off-set scan is in general below the level determined from the rocking curve fits and is somewhat noisy. This noise is not expected to be based on physical features, but solely due to the variance of the counts which is relatively high for low levels. The background as determined from the rocking curves is expected to be more accurate, because it is based on a fit of a number of points.

It is noted that this method of background subtraction will not work correctly if the background is peaked under the specular peak; this is for instance possible for long-range lateral correlations at liquid interfaces [68] or metallic

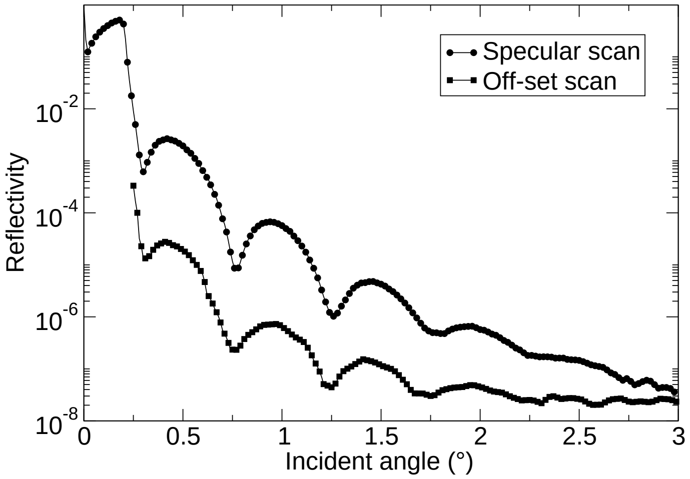

Figure 4.11: Experimental scan and off-set scan. The curves have *not* been shifted for the sake of clarity.

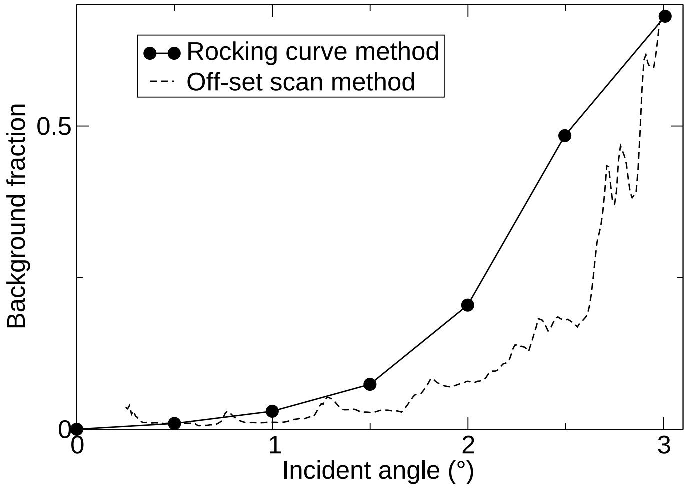

Figure 4.12: The background fraction of the total experimental signal for the off-sett method and the rocking curve method.

multilayers, where the correlation lengths ξ_i can be rather large and the Hurst parameters h_i rather small [69]. The only way to resolve this problem is to perform a combined analysis of the non-specular and specular scattering using a joint set of parameters.

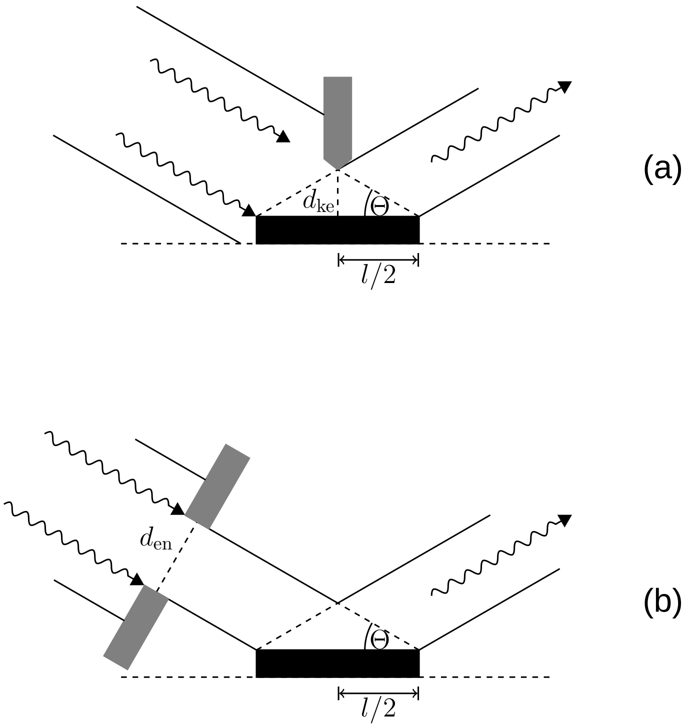

Figure 4.13: Schematic setups for reflectivity measurements with (a) and without (b) beam-knife edge.

4.4.3.2 Geometrical corrections

The geometrical corrections in the region of the plateau of total external reflection have been described by Gibaud *et al.* [20]. They give a method to correct for the effective beam height below the so-called spill-over angle $2\theta_{\mathrm{so}}$. The spill-over angle is defined as the angle for which the full beam height illuminates the complete (rectangular-shaped) sample in the scattering plane. Below $2\theta_{\mathrm{so}}$ only a part of the incident beam intensity is used, whereas beyond $2\theta_{\mathrm{so}}$ the beam footprint on the sample is smaller than the sample surface itself. A second correction is necessary because the presence of the sample modifies the intensity repartition of the direct beam, which makes that - viewed from the detector - the apparent center of the direct beam is no longer at $2\theta = 0$ but shifted by an amount of FWHM/4, where FWHM is the full width at half maximum of the direct beam.

The correction for the partially masked beam intensity below the spill-over angle is only valid for a configuration without beam-knife edge. Beam-knife edges are routinely used in the setups of several commercial reflectometers and have the function to reduce the air scattering and the beam footprint, so that on the one hand unwanted effects due to a possible substrate curvature are reduced, and on the other hand the spill-over angle is reduced so that the plateau of total external reflection becomes more visible. The slit that is defined by the beam-knife edge varies usually between 2-20 μm. Fig. 4.13(a) depicts the situation in the presence of a beam-knife edge and it follows that within a first approximation the spill-over angle is defined by $2\theta_{\rm so} = 2\arctan(2d_{\rm ke}/l)$, where $d_{\rm ke}$ is the slit defined by the beam-knife edge and the sample surface and l the length of the sample surface in the scattering plane. For comparison the classical geometry is given in (b) where the beam width is defined by an entrance slit. In this case the spill-over angle is given by $2\theta_{\rm so} = 2\arcsin(d_{\rm en}/l)$ where $d_{\rm en}$ is now the entrance slit height. The correction is, apart from a factor 2, thus practically the same, since at low angles $\tan\theta \sim \sin\theta$. When d and l are not appropriate $\theta_{\rm so}$ can be larger than the critical angle for total external reflection. Using typical parameters for a laboratory setup, $d_{\rm ke} = 15\mu$m, $d_{\rm en} = 50\mu$m, $l = 2$ cm, spill-over angles $\theta_{\rm so}$ of 0.085° and 0.143° are calculated for the beam-knife edge setup and the classical setup, respectively. The critical angle for silicon is for Cu radiation 0.22° , implicating that for many organic films with critical angles in general well below that of silicon it becomes important to apply the footprint correction especially in the case of a classical setup. Whenever the spill-over angle is lower than the critical angle it becomes less important to do a proper correction, since the phase of the reflectivity changes only very slightly (due to absorption), meaning that the information content is negligible.

Gibaud *et al.* [20] give expressions for the correction to be applied to the calculated reflectivity for the classical setup in the afore-mentioned linear approximation, but also using a non-linear approximation, which takes implicitly into account the divergence of the beam. Usually data fitting programs will not allow to apply such a correction to the calculated reflectivity, so that the inverse correction should be applied to the experimental curve in the linear approximation:

$$I_{\rm exp,corr}(2\theta) = I_{\rm exp}(2\theta)\theta_{\rm so}/\theta \qquad (4.1)$$

for both setups and where the approximation $\tan\theta \sim \sin\theta \sim \theta$ has been used. The correction has to be done below the spill-over angle $\theta_{\rm so}$. Whenever the corrected reflectivity becomes larger than 1.0 it is reset to 1.0. The spill-over angle can be calculated from the physical parametes d and l, but can also be estimated from the quasi-linear increase of the reflectivity below the critical angle (Baulès, 2006).

4.4.3.3 Normalisation of the counts

The reflectivity signal is defined as the ratio of the incident and the scattered photon flux. In order to be able to compare with theory, the data should thus be normalized to the incident flux. There are three ways to do this. The first method measures simply the incident flux without the sample and the same primary and secondary optics. While this seems to be the most appropriate method, it is not always practical, especially in the case of configurations where a beam knife edge is used to condition the beam. The best value which can be obtained is half the incident flux by measuring the intensity with the sample in place at zero angles, but it is found that alignment problems are so critical that the error is often 10% or larger. The second best option for normalisation is then to normalize to against the values found at the plateau of total external reflection. This plateau is usually much better defined than in a configuration without a beam knife edge. However, also this method is far from ideal, especially for highly absorbing samples which tend to level off the plateau of total external reflection. The last, and less recommended method, is to do an *ad-hoc* adjustment during data modeling and/or refinement [70].

4.4.3.4 Interval scaling and data binning

The scaling of the different intervals with respect to each other can be done in several ways, each of which is not necessarily worse or better than the other. The first method uses the different attenuation factors and the different step counting times to scale the data correctly with respect to each other. A second method remeasures one or several data points when a parameter as the attenuation factor or the step counting time has changed, and uses the counts of the overlapping data point(s) to determine the proper scale factor. The advantage over the first method is obviously that no book-keeping is needed for the physical parameters such as the attenuation factor and the step counting times. While the latter method is obviously identical to the first method when the counting statistics are sufficiently good, the method performs less well when the counting rate is too low. Therefore the local data routine employed by the authors [71] falls back to the first method whenever the counts of the overlapping points become lower than 1000.

In order to recalculate the reflectivity curve to a fixed or another step width, a second-order B-spline interpolation is used [72–74]. This works very well when the data collection strategy outlined in section 4.4.2 is used: the rebinned and original reflectivity curves are virtually indistinguishable.

4.4.3.5 Resolution function correction

The resolution function correction was described by Gibaud *et al.* [20] and is essentially a convolution of the calculated reflectivity with a Gaussian resolution function. Note that this correction is applied to the *calulated* reflectivity and not to the *experimental* one, because the latter would have to be deconvoluted which is mathematically much more difficult than the convolution operation. In some cases, however, deconvolution is needed rather than convolution, e.g. when *ab-initio* inversion procedures are tempted to solve for the density profile. A method was developped for deconvolving experimental reflectivity curves [75] that is based on a heuristic combination of zeroth-order Tikhonov regularisation [76] and the Lucy-Richardson algorithm [77, 78]. Essential for these methods is that the instrumental resolution function is known; this can either be calculated [21] or simply be approximated by measuring the profile of the direct beam. Note that in many cases the *apparent* resolution function is wider than the the experimental resolution function, since it may incorporate all kinds of other effects, such as those due to lateral inhomogenieties and wafer bending.

4.4.3.6 Other corrections

Other corrections are not specific to reflectometry, but have to be applied for high accuracy measurements. The dead-current correction, *i.e.* the detector counts due to electronic noise in the absence of sample and X-ray source, becomes important for long counting times and low scattered intensities. For the 12 years old Bruker NaI detector at the author's institute, this correction has remained virtually constant over the years at 0.14 counts per second, which represents for the longest counting time possible with the Diffrac^{plus} software [79], 650 seconds, 91 counts, which is non-negligible when countings are below 1000 counts. Some software packages apply a linearity correction when the detector starts to saturate, but is is thought to be better to avoid saturation by applying the necessary attenuators.

Bridou [80] has studied the effect of the bending of wafers on the reflectivity signal. This can be in particular a problem if too thin substrates are used which tend to induce a curvature due to internal constraints: in our experience silicon wafers thinner than 500 μm cause considerable problems. It is noted that the effect of small curvatures can be accounted for by the parameter that describes the instrumental resolution.

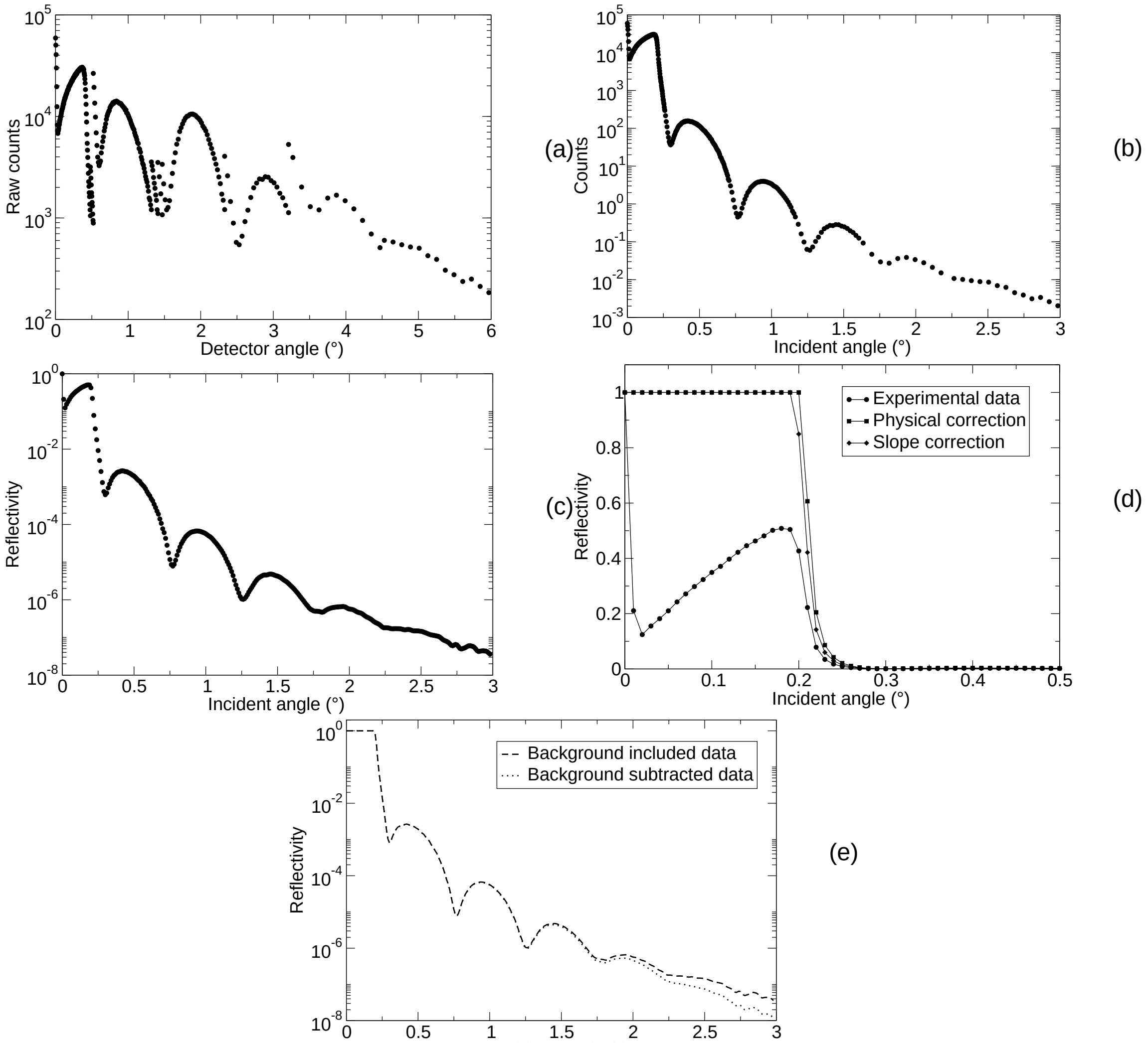

Figure 4.14: Data reduction steps: (a) raw data; (b) scaling; (c) binning and normalisation; (d) footprint correction; (e) background subtraction.

4.4.3.7 Example of corrections

The effects of the corrections to be applied are illustrated in Fig. 4.14 for the same sample as was used to illustrate the background correction. The upper figure shows the raw data before any correction. The first two intervals were measured with step times of 1 and 3 seconds, respectively, and with a copper foil with an attenuation factor of 29.8. The following seven intervals were measured without any attenuator and step times increasing from 1 second to 650 seconds. Raw counts varied in between 59166 and 184. In the second step data were scaled following the procedures described in section 4.4.3.4, which is shown in Fig. 4.14(b). The detector angle was changed as well, in this case to the incident angle, but it could have been the momentum transfer q_z as well, depending on the program to be used to analyse the data further. In addition the dead current correction was applied in this step. In the third step the data are normalized and binned to a constant step size, 0.01° in θ (Fig. 4.14(c)). Fig. 4.14(d) shows the results of the footprint correction using the physical parameters and the ratio determined by the quasi-linear slope between 0.02 and 0.16°. It is observed that the alignment was probably not perfect, because the shifted direct beam pattern is not clearly observed. It is noted that this can also be due to 'border' effects of a not well-cut substrate. The physical parameters used for the correction are $l = 4.8$ mm and $d = 0.02$ mm, yielding a spill-over angle of 0.573°, well beyond the critical angle. The spill-over angle determined from the slope is 0.398°. The drawback of either method is that absorption effects are not taken into account, which means that the fall in intensity at the critical angle is too abrupt; the reflectivity signal of even low absorbers, such as carbon, tends to fall very slowly at the plateau of total external reflection, rounding the "corner" more or less significantly, but in any case more than in Fig. 4.14(d). Fig. 4.14(e) shows finally the effects of the background subtraction determined using the rocking-curve method. As expected, the true specular signal differs only significantly at high momentum transfers, but this will consequentially influence the determination of the roughness parameters.

4.4.4 Conclusions

Data reduction procedures in X-ray reflectometry are not very complicated to apply if the geometry and the conditions of the experiment are well-known, but unfortunately these conditions and the way the data were reduced are not very often mentioned in the open literature. Commercial data reduction packages - often integrated in the data collection software - certainly reduce reflectivity data, but are not too specific on how it is done and it is feared that they are in particular weak with respect to some aspects, notably the background subtraction. Local data reduction software will often perform a large part of the corrections described above, but this software is usually badly documented and specific to a particular setup. A common set of descriptors for the data reduction process, such as is used in the Crystallographic Information Framework (CIF [81]), would certainly be helpful for a better documentation of the reflectivity experiment and the intermediate step - the data reduction - towards data that can be compared with theory. An initiative is under way to achieve such a common data format (rfCIF [82]).

4.5 Data analysis methods for X-ray and neutron specular reflectivity data

Data analysis methods for specular X-ray or neutron reflectivity are compared. The methods that have been developped over the year can be classified acccording to different types. The so-called classical methods are based on Parratt's or Abelès' formalism and rely on the minimization using more or less evolved Levenberg-Marquardt or simplex routines. A second class uses the same formalism, but optimizing is done with simulated annealing or genetic algorithms. The third class uses alternative expressions for the reflectivity, such as the Born Approximation or Distorted Born Approximation. This makes it more easy to directly invert the specular data, coupled or not with classical least-squares or iterative methods using overrelaxation or charge flipping techniques. The fourth class uses mathematical methods founded in scattering theory to determine the phase of the scattered waves, but have to be coupled in certain cases with (magnetic) reference layers. The strength and weakness of a number of these methods is evaluated on simulated and experimental data. It is shown that genetic algorithms are by far superior to traditional and advanced least-squares methods, but that they fail when the layers are less well defined. In the latter case the methods from the third class or the fourth class are the better choice, because they permit to obtain at least a first estimate of the density profile that can be refined using the classical methods of the first class. It is also shown that different analysis programs may calculate different reflectivities for a similar chemical system. One reason is that the representation of the layers is either described by chemical composition, or by scattering length or electronic densities, between which the conversion of the absorptive part is not straigtforward. The second important reason is that the routines that describe the convolution with the instrumental resolution function are not identical.

4.5.1 Introduction

The analysis of data from specular X-ray or neutron reflectivity experiments has been traditionally carried out by non-linear least-squares fitting using Parratt's recursive relation [11] or the equivalent optical matrix method - also called Abelès' method [83]. For this method the thin film is divided in a small number of parallel sublayers, for each of which parameters as the scattering density, thickness, and interfacial roughness can be varied until a cost function is minimised. The method is said to be model-*dependent*. It proves to become quite cumbersome once the number of sublayers becomes larger than, say, two. Even with two layers the starting parameters should be very close to the final ones to avoid the least-squares minimisation being trapped in a local minimum. Several methods have been developped to obtain a reasonable starting point, among which simulated annealing techniques, monte carlo techniques and genetic algorithms are mostly used. Although these methods could be of help for relatively simple problems, they fail in general when the density profile becomes too complicated, or, in other words, when the thin layer has to be divided in a number of slices in order to correctly describe the density profile.

To overcome these problems several new data analysis methods have been developed in recent years and have been applied to a few dozen of cases. Although neither of the methods claim to derive a unique profile, which is inherently impossible without any *a-priori* knowledge of the system, they do aim to extract in a model-*independent* way the density profile from the reflectivity data. It is shown hereafter that this is not completely true, except for one method. The main purpose of this paper is to compare the traditional and less-traditional analysis methods and to show in which circumstances they can be used and how the results should be judged. For that purpose the assumptions underlying the different methods should be well known. In addition a combination of a numerical and graphical agreement analysis is proposed similar to what is commonly used in powder diffractometry.

It should be noted that the phase recovery problem for a one-dimensional experiment such as specular reflectivity differs from that for two- or three-dimensional problems such as encountered in crystallography or astronomy. The basic difference is that in the 1D-case there may exist a multitude of phase sets corresponding to the same amplitude set, whereas in the 2D and the 3D case the resulting phase set is in general unique [84]; see also section 4.5.2.11).

Numerous papers have been devoted to solution of the phase problem in the analysis of X-ray or neutron reflectivity using a particular method, but only a very few mention different methods [5, 6, 9] in use. A real comparison to judge the strength and weakness of each method is, however, not made. This paper is an extension of a preliminary report [85] which aims to compare different analysis methods using simulated and experimental data.

4.5.2 Data analysis methods

In this section the methodology of four different categories of analysis methods will be explained and compared. The profile along the normal of the surface will be designated as the scattering length density profile (SLD) $\rho(z)$ in units Å^{-2} which has the advantage that it can be used for X-rays as well as neutrons. The relation between the scattering length density $\rho(z)$ and the electronic density $\rho_{\mathrm{e}}(z)$ is $\rho(z) = r_0 \rho_{\mathrm{e}}(z)$, where r_0 is the Thomson scattering length of the electron. As is well-known, the chemical composition should be known in order to calculate the mass density from the SLD or the electronic density; for the X-ray case the conversion formula is - neglecting dispersion effects:

$$\rho_{\mathrm{e}}(z) = N_{\mathrm{A}} \rho_{\mathrm{m}}(z) \frac{\sum c_j Z_j}{\sum c_j A_j} \tag{4.2}$$

where N_{A} is Avogadro's number, Z_j the number of electrons of element j, A_j the atomic weight of element j, and c_j the molar fracion of element j. Although in the following only examples for X-ray analysis are given, most of what is said applies as well for the neutron case. For a similar chemical system, the neutron SLD is in general 5 to 10 times smaller than the X-ray SLD, but this is from a computational point of view not important. Exceptions that are important for the way how the data are analyzed will occur whenever the neutron SLD becomes negative or when polarized neutrons are used.

4.5.2.1 Classical gradient methods

Parratt's recursive method [11] is the most widely used method to calculate the reflectivity and it is strictly identical to what is also called the optical matrix method [86] or Abelès method [83]. In this method the film is divided into one or more sublayers of varying thickness and scattering length density. To each sublayer, and also to the substrate, a parameter is added that describes the interfacial roughness. Both Parratt's recursive method as the optical matrix method are dynamical in nature, *i.e.* multiple reflections at the interfaces are explicitly taken into account. In addition the refraction effects occurring at the interfaces are also described. All programs from commercial suppliers of reflectometers incorporate this algorithm, and a number of free programs as well: *Parratt32* [87]; *Firefx4c* and *Wfiref3h* [88], *IMD* [89, 90], *SimuRX BAU06*.

Parratt's formula is given by:

$$R_j = \frac{F_{j+1} + R_{j+1} e^{2ik_{j+1}\Delta z_{j+1}}}{1 + F_{j+1} R_{j+1} e^{2ik_{j+1}\Delta z_{j+1}}}, \tag{4.3}$$

where Δz_j is the thickness of layer j, $k_j = n_j k = \sqrt{k^2 - 4\pi\rho_j}$ the z-component of the wave vector within layer j, k the free wave number ($2\pi/lambda$), and ρ_j the scattering length density within layer j and F_j the Fresnel coefficients for each individual layer j defined by:

$$F_j = \frac{k_{j-1} - k_j}{k_{j-1} + k_j} \tag{4.4}$$

If the k_j and Δz_j are given for $j = 1, 2, 3, ..., N$, R_j can be calculated for all j by starting at the layer adjacent to the substrate $j = N$. Note that in the first step ($j = N$) $R_{N+1} \equiv 0$ since there is only transmittance within in the substrate. Thus $R_N = F_{N+1} = (k_N - k_\mathrm{s})/(k_N + k_\mathrm{s})$, the Fresnel reflectance of the substrate. The reflectance of the complete system is then given by R_0. If the substrate/film interface is located at $z = 0$ and the thickness of the complete film is $d = N \sum \Delta_j$ (air/film interface at $z = -d$) then the reflectance becomes

$$R = R_0 \exp(-2ik_0 d). \tag{4.5}$$

The calculated reflectivity which is compared to the measured reflectivity - after data reduction, see Salah *et al.* [91] - is then given by its squared modulus $r = |R|^2$.

Whereas the algorithm gives the exact reflectivity for a stratified system, it is very cumbersome to apply in least-squares algorithms because of its high non-linearity. Another complicating factor is the very large dynamic range of a typical reflectivity experiment, spanning 5 - for neutrons - to 9 or 10 - for synchrotron measurements - decades. Its use for *fitting* reflectivity curves is, however, limited, because of the very large dynamic range of the reflectivity. The algorithms that are used for the least-squares are mostly of the Levenberg-Marquardt or Simplex type, and is normally only used for a very limited number of sublayers, except for the so-called multislice method (see section 4.5.2.4).

4.5.2.2 Genetic and simulated annealing algorithms

Since the afore-mentioned gradient-type algorithms appear to perform poorly for the reflectivity case other optimization algorithms such as the genetic algorithm have been proposed as an alternative for the analysis of reflectivity data [92–95]. The simulated annealing method has found as well applications in X-ray and neutron reflectivity [96–98]. Both algorithms are certainly not specific to reflectivity analysis, and will therefore not be discussed here in detail. The main advantage of the algorithms compared with traditional gradient methods is that they are not easily trapped into a local minimum. It was reported as well that the algorithms, although not easily trapped in secondary minima, rarely converge to the exact minimum because of its non-gradient nature. Both are usually followed by a classical gradient method.

4.5.2.3 Quasi model-independent methods

Whereas the methods discussed in the sections 4.5.2.1 and 4.5.2.2 are said to be model-*dependent*, since a starting model has to be provided that is more or less close to the final model, new methods have been developped that claim to be in a sense model-*independent*, since the starting model is normally very simple - a single layer with a constant density - and the methods are capable to determine gardient and other irregularities in the density profile that are impossible to find with the classical methods. In fact these methods are not real model independent methods, since certain pre-information, such as the total layer thickness and also the mean density are input to the routines.

4.5.2.4 Parameterizing the profile.

Parratt's formula is normally used with a very limited number of slices, each of which is characterized by a variable thickness, scattering length density, and interfacial roughness. Several groups have developped methods based on Parrat's formula that are in theory capable to describe more complicated density profiles, such as gradients. Pedersen & Hamley [4] have parameterized the scattering length density profile in either cubic splines or a series of sine and cosines. The coefficients of either series are determined during the least-squares procedure, which is modified by the addition of a Lagrangian multiplier in order to stabilize the convergence of the fit [99, 100]. Nearly the same algorithm was developped by Berk & Majkrzak [31] differing only in the details. Both methods rely on a fairly large number of coefficients to be fitting using robust mathematical methods and are in fact not too different from the multislice method developped by Ober [88] and which uses adaptive Lagrangian multipliers for an improved convergence coupled with the Levenberg-Marquardt algorithm. The latter method is very close to the original Parrat method, dividing the total film thickness in equally thick slices. The parameters to be refined are the electronic density of each slice and eventually one overall roughness parameter describing all interfacial roughnesses. The starting point is mostly the total layer thickness and the mean density which can be directly estimated from the reflectivity curves.

4.5.2.5 Box iteration using the Born approximation.

Box iteration is usually called 'box refinement', but to avoid confusion with refinement methods by non-linear least-squares we prefer 'iteration', since it is basically an iterative method. It has a history of more than 20 years and was originally used in one-dimensional diffraction experiments [101, 102]. It was proposed for reflectivity as well in 1996 by Li *et al.* [28] including a small, but important modification that is specific for the reflectivity experiment. This modification concerns the phase factor $iq.z$ for which it was argued that q should be taken as the (average) wave vector *inside* the film and not the free space wave vector. In the following years the box iteration method was several times proposed in slightly adapted form without any reference to the earlier work [29, 103, 104]. The work of Bengu *et al.* [104] incorporates the method in a sound mathematical framework and uses the final solution as input for a genetic algorithm to find alternative solutions. Amazingly, the method has aroused new interest in single-crystal diffraction as well under the name 'charge flipping' as an alternative structure solution method that is more *ab-inito* than the traditional direct methods, since *a-priori* chemical information is not used to recover the phases [105].

The principle of the box iteration is outlined in Fig. 4.15. The film or box of thickness d is divided in slices of thickness Δz corresponding to the experimental resolution π/q_{max}, where $q = 2k$ is the momentum transfer. An initial model $\rho_o(z)$ is taken for which the SLD is constant in each slice. The derivative of the SLD $\rho'_{exp}(z)$ thus takes only values at the air/film interface and the film/substrate interface. In the first step the complex reflectivity is calculated from this model using either the kinematical expression or Parratt's recursive formula. Then the Fourier space constraints

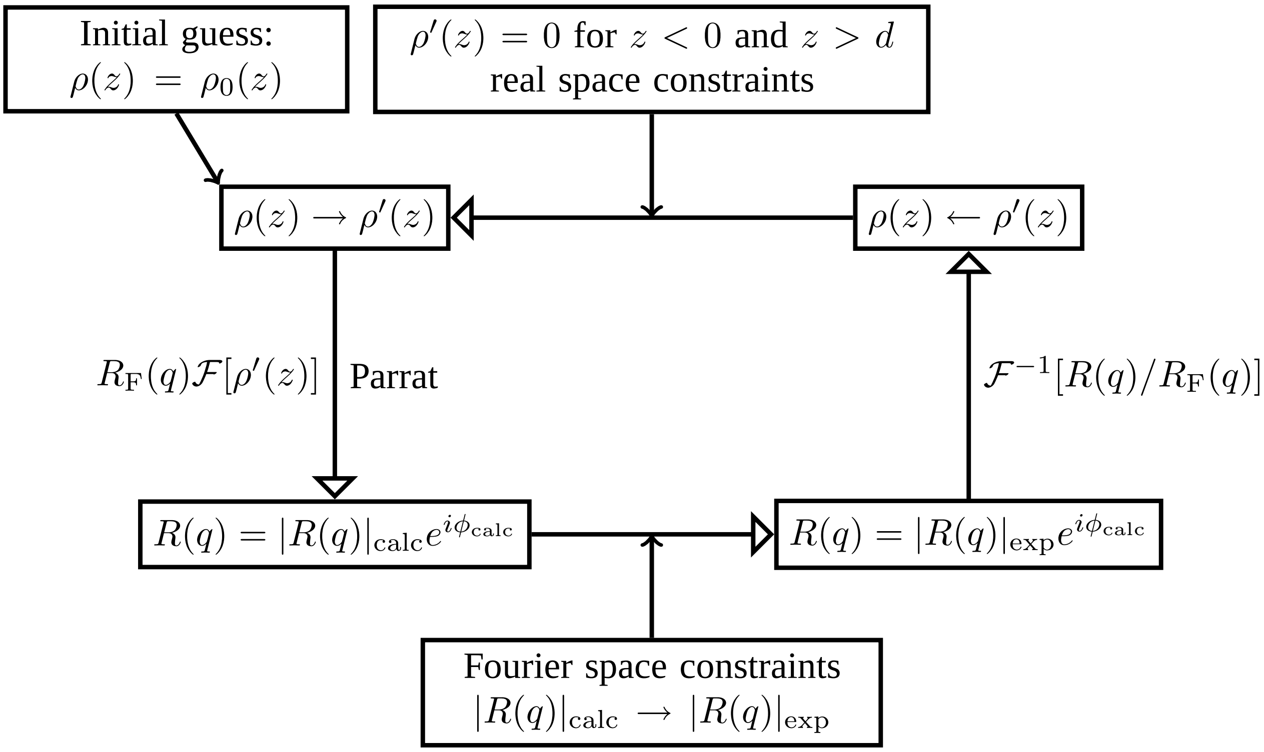

Figure 4.15: Scheme for the iterative box refinement method. The calculation of the reflectance is done either by the forward Fourier transform in the kinematical approximation or by Parratt's method. The real space constraint may or may not include overrelaxation or charge flipping constraints (see text).

are applied by setting the calculated modulus equal to the experimental modulus. A new profile $\rho'_{cal}(z)$ is calculated according to the Born Approximation (BA) expression

$$r(q) = r_{\mathrm{F}}(q)\left|\int \frac{d\rho}{dz} e^{iqz} dz\right|^2 \tag{4.6}$$

where $r_{\mathrm{F}}(q)$ is the Fresnel reflectivity of the substrate. $\rho'_{cal}(z)$ is accordingly set to a new $\rho'_{exp}(z)$ while applying the (real-space) box constraints, *i.e.*, $\rho'_{exp}(z) = 0$ for $z < 0$ and $z > d$. Bengu *et al.* (2001) use in this step scalar constants as overrelaxation parameters to the actual profile, which fulfill in a certain sense the same role as the flipping parameters in the Oszlányi & Süto algorithm. The iteration is continued until $\rho'_{exp}(z)$ does not change significantly anymore. At this stage the reflectivity is calculated using this model with Parrat's recursive expressions and compared with the experimental reflectivity. The program that was used in this study (program *BA*) was developped locally and necessites several parameters such as the maximum number of iterations, the SLD of the substrate and a mean value of that of the film, and finally an approximate value of the thickness; it is noted that the program does not use an overrelaxation or flipping parameter as proposed by Bengu *et al.* [104], and is closest to Sanyal's implementation [32]. There are no freely or commercially available implementations of the program known.

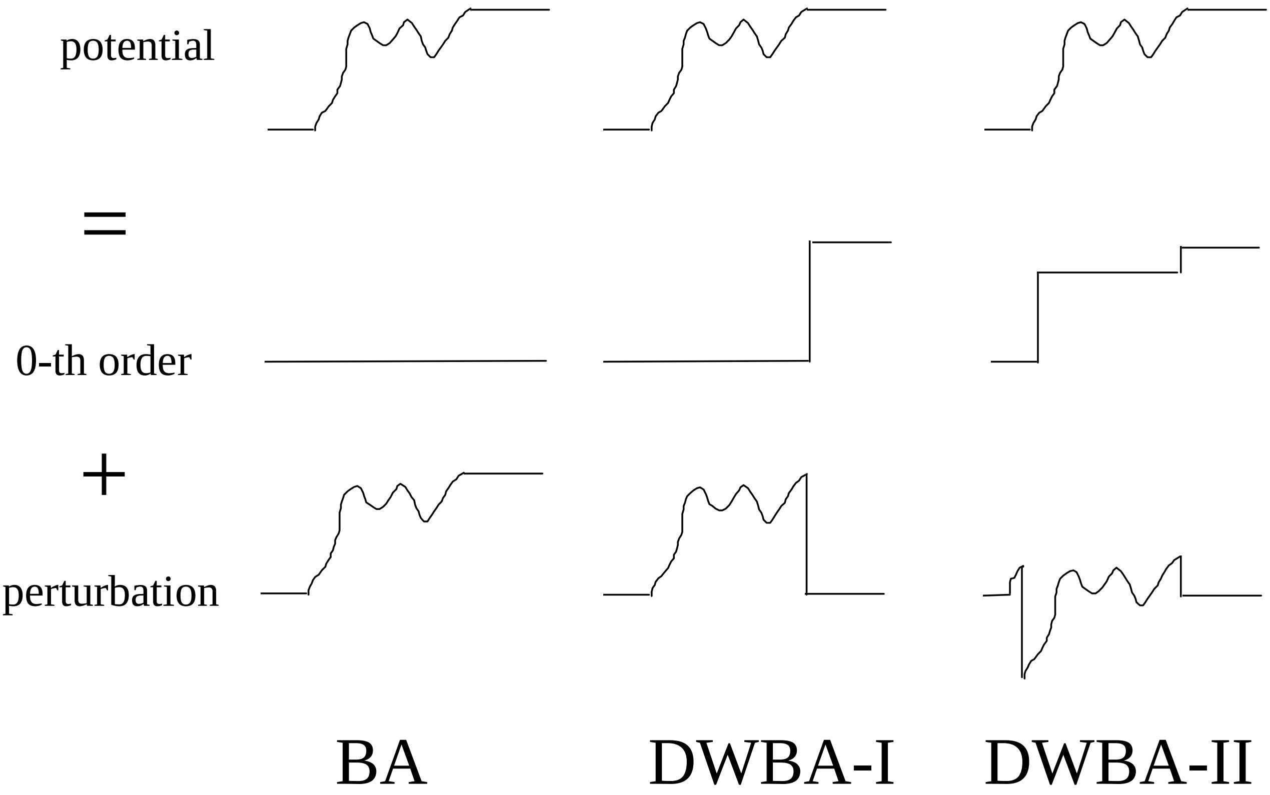

Figure 4.16: Born and distorted-wave Born Approximation as pertubations on a known potential. In the BA the perturbation can be considered as the potential itself (left); in the two different DWBA's the perturbation is either with respect to the substrate (DWBA-I; middle) or with respect to a substrate plus a known film (DWBA-II; right).

4.5.2.6 Least-squares with alternative expressions for the reflectivity.

The Born approximation treats the interaction potential as a perturbation on the potential in the absence of the sample [12]. Alternatively, the distorted-wave Born approximation (DWBA) can be utilized, in which a known reflectivity of a sharp surface is taken as the zero-order approximation and the difference between the corresponding potential and the actual potential as the perturbation. The fundamental difference between the BA and the two different DWBA's that are treated in this section is illustrated in Fig. 4.16.

Usually the known potential is that of the substrate, since the substrate and its Fresnel reflectivity are known exactly. The expression for the reflectance becomes then:

$$R = R_{\mathrm{F}} + \frac{2\pi}{ik}\int_{-d}^{0}(e^{ikz} + R_{\mathrm{F}}e^{-ikz})^2\rho(z)dz, \tag{4.7}$$

where R_F is the Fresnel reflectance of the substrate. The advantage of this formula is that it can be evaluated, like the BA expression (Eq. 4.6), for general scattering length density. It is in addition more accurate than the BA, especially in the vicinity of the critical angle. The disadvantage of Eq. 4.7 is that it can not easily be inverted, *i.e.*, calculating the SLD $\rho(z)$ when the reflectance R is known.

It is also possible to develop the DWBA by taking the potential for a thin film on a substrate as the zeroth order approximation. This approach was proposed by Sanyal *et al.* [32] and finds practical applications in experimental X-ray reflectivity. The expression for the reflectance is now:

$$R = iR_0 + \frac{2\pi r_0}{k}(a^2(k)\Delta\rho(q) + b^2(k)\Delta\rho^*(q)), \tag{4.8}$$

where $\Delta\rho(q)$ is the Fourier transform of $\Delta\rho(z)$ (and $\Delta\rho^*(q)$ its complex conjugate), the deviation with respect to the zeroth-order approximation, and R_0 the reflectance of the zeroth-order approximation. $a(k)$ and $b(k)$ are the transmittance and the reflectance in the film of constant density, respectively.

A method that is closely related to this general expansion method is based on an expansion of a variation of scattering length density with respect to a film of constant electron density. Quite often the assumption of a constant density gives a rather good fit to the experimental data, but details in the reflectivity indicate that the density $\rho(z)$ is not really constant, but that small variations $\Delta\rho(z)$ must exist with respect to an otherwise constant ρ_0. The overall scattering length density can thus be written as $\rho(z) = \rho_0 + \Delta\rho(z)$. The Fourier transform of the density variation $\Delta\rho(z)$ can then be written as:

$$\Delta\rho(q) = \int_{-\infty}^{\infty} \Delta\rho(z)e^{iq}dz. \tag{4.9}$$

The thin film is divided in N slices $\Delta\rho_j$ of thickness d, so that Eq. 4.9 is written as:

$$\Delta\rho(q) = \frac{i}{q}\Big\{\Big(\sum_{j=2}^{N}(\Delta\rho_j - \Delta\rho_{j-1})e^{iq(j-1)d}\Big) \qquad + \delta\rho_1 - \delta\rho_N e^{iqNd}\Big\}. \tag{4.10}$$

This expression is inserted in the formula for the specular reflectivity in the DWBA, *i.e.* the squared modulus of the DWBA reflectance (Eq. 4.8):

$$r(k) = |iR_0 + \frac{2\pi r_0}{k}(a^2(k)\Delta\rho(q) + b^2(k)\Delta\rho^*(q))|^2. \tag{4.11}$$

The coefficients $a(k)$ and $b(k)$ of the substrate plus supposed constant density film can be calculated using tabulated values of the dispersion correction parameters f'_j and f''_j. Expression 4.11 is then used, along with expression 4.10 to fit, after convolution with the instrumental resolution function, against the experimental data, using the $\Delta\rho_j$ as fit parameters. As a starting point all $\Delta\rho_j$ are taken to be zero. The resulting $\Delta\rho_j$ are accordingly used in Parrat's recursive relation (Eq. 4.3) to calculate the reflectivity that is to be compared with the experimental data. The number N of slices to be taken depend on the resolution of the experiment (see also section 4.5.2.5). The thickness of the layer L must be known approximately. The number of slices follows then by $N \approx \mathrm{nint}(2q_{max}L)$, where the function nint(x) gives the closest integer to x. Interfacial roughness of the film with constant density ρ_0 is not taken into account in deriving the two coefficients $a(k)$ and $b(k)$. The roughness redefines itself by proper values of the coefficients $\Delta\rho_j$. The method that was tested here follows closely the description given by Sanyal *et al.* [32]. It is noted that the implementations of the algorithm are rare and that it has been used in only a small number of cases [106–109]. The multi-purpose program *Maud* [110] has an implemention, whereas the implementation used in this study has been written locally (program *DWBA*); the latter has been integrated recently in *SimuRX* [70].

4.5.2.7 Methods using wavelet transforms.

It is well known that the properties of the Fourier transform can be used to extract certain information from the reflectivity curve. Using the Born approximation it is easily shown that the inverse Fourier transform of the reflectivity signal multiplied by q^4 is equal to the autocorrelation (or Patterson) function of the derivative of the density profile. From this function the thickness parameter(s) can be estimated, but it cannot be known in advance in which order the different layers appear. Smigiel & Cornet [111] used wavelet analysis to determine the order of the layers in a stack; Prudnikov *et al.* [112] analysed in detail the roughness parameters of a metallic multilayer with a wavelet approach, and Berk & Majkrzak [113] used wavelets for reconstructing a model-free interpretation of truncated phase-sensitive neutron reflectivity data. Wavelet analysis as a common approach to problems in X-ray or neutron reflectivity is, however, not available in free or commercial programs.

4.5.2.8 Direct phasing methods and non-fourier inversion

Direct phasing methods have been recently proposed in X-ray and neutron reflectometry. They are, as in crystallography, either based on an experimental determination of the phase, or on mathematical extraction. Once the phase set has been found, the complex reflectances have to be inverted to get the density profile. This is done either by simple Fourier inversion, assuming the Born approximation being valid or dynamically using either Gel'fand-Levitan-Marchenko integral equations [114] or layer-stripping methods [35]. They are thus ”more” model-independent than the quasi-independent methods discussed before, since no pre-information such as total layer thickness or mean density is used. Even information about the substrate, which is usually known, is not necessary. Both steps, phase extraction and inversion, have their mathematical limitations, but they will be discussed only briefly.

4.5.2.9 Mathematical determination of the phase using only one measurement.

A mathematical determination of the phase was proposed at about the same time by Klibanov & Sacks [57] and Clinton [58], but not tested on its experimental feasability. The method is based on the fact that $\rho(z)$ (and $\rho'(z)$) are causal functions, because the functions are equal to zero for $z < 0$. This makes it possible to relate the real and imaginary part of the susceptibility function, *i.e.* the complex reflectance $R(q)$, by a Hilbert Transform at the condition that $R(q)$ does not have zero's in the upper half of the complex plane (UHP). In other words, the phase can be in certain cases calculated from the amplitude set using a *logarithmic* Hilbert Transform. Which cases was approximately determined by Clinton [58] and later refined for the dynamical case by Van der Lee [75]. The latter paper also shows the experimental feasability of the method. Considering a layer with mean SLD ρ_{f} and thickness d that consists of N sublayers each having a fixed potential ρ_i, and a substrate having a potential $\rho_{\mathrm{s}} \equiv \rho_{N+1}$ the following inequalities should approximately hold for

$R(q)$ having no zeros in the UHP:

$$\rho_1 \lesssim \sum_{i=2}^{N+1} |\Delta\rho_i| \tag{4.12}$$

where $\Delta\rho_i = \rho_i - \rho_{i-1}$. If in addition $\rho_\mathrm{f} < \rho_\mathrm{s}$ holds, then the following relation should hold as well:

$$d \lesssim d_\mathrm{crit} = \frac{\rho_\mathrm{f}}{\sqrt{4\pi\rho_\mathrm{s}}\Delta\rho_\mathrm{s}} \tag{4.13}$$

Since it can not been known in advance whether the foregoing two inequalities hold or not, this phase determining method can not be considered being truly *ab-initio*. However, chemical preknowledge on the system should help to decide whether the method can applied or not. If so, the method gives a truly model-independent profile, since no fitting parameters whatsoever are used, not even the knowledge of the substrate potential. A program, *LDR*, was developped [115] to determine the SLD in a two step procedure: in the first step the phase of each reflectivity data point is determined by evaluation of the logarithmic Hilbert integral and in the second step the complex reflectance is inverted using the layer-stripping method.

One other attempt has been reported to determine the phase by mathematical means and only one measurement, *viz.*, by Berk and Majkrzak [116], who showed that it is possible to deduce the phase in a unique way using thin films having symmetric potentials. Most potentials are, however, not symmetric, but special preparation methods can be used to make them more the less symmetric [37, 39].

4.5.2.10 Mathematical determination of the phase using several measurements.

Much theoretical and experimental work has been devoted by the groups of Lipperheide and Berk & Majkrzak to the determination the phase by measuring more than one reflectivity curve using neutrons while changing the physical state of a component of the system. Initially the work concentrated on the use of magnetic reference layers [37, 117, 118], but later extended to a variation of the surrounding medium, either fronting or backing [39]. The latter method has been succesfully applied to a number of systems, such as hybrid bilayer membrane systems [119] or polymeric lipid bilayers [120]. Aktosun & Sacks [121, 122] have proposed an alternative two-measurement method using a reference layer which can be used with neutrons as well as X-rays - thus without changing the magnetic polarization state of the layer - but its experimental feasability has never been demonstrated.

4.5.2.11 Experimental determination of the phase by anomalous reflectivity or neutron contrast variation measurements.

Several efforts have been reported to determine the phase by experimental means using anomalous reflectivity experiments [40, 123, 124]. The element-specific nature of anomalous scattering is exploited to derive the density profiles specific to that element. The idea is in principle the same as that used in the contrast variation technique in neutron reflectivity where specific elements can be traced by changing their isotopic occurrence [6, 125]. It is noted that these methods are based, like those in section 4.5.2.10, on the measurement of two different reflectivity curves, but that these in this section normally involve the Born approximation for the analysis, and that the theory is not dynamically exploited.

4.5.3 Results

In this section different algorithms will be compared to find the density profile that is most compatible with the experimental data after data reduction. The trial-and-error method will be excluded from the comparaison, although it would be interesting to investigate the influence of the researcher on the final result using this method. Note that this is rather the topic of a round robin and it is mentioned elsewhere [126]. Simulated data as well as experimental data are used for the tests.

4.5.3.1 Program used

Least-squares routines are used in the four different programs to be compared, from which the first three are free for academic users, *viz.* *IMD* [89, 90], *Parratt32* [87], *Wfiref3h* [88], *LEPTOS* [127], and Motofit [128]. The programs differ in their representation of the reflectivity data and the parameters. *IMD* represents the reflectivity data *versus* angle, either normal or grazing incidence, in degrees, milli-degrees or radians; with *Parrat32* data should be represented in momentum transfer units q_z (Å^{-1}), whereas *Wfiref3h* gives the possibility to import a variety of different representations, and it internally converts in q_z (Å^{-1}). The sample parameters are given either in electron densities (*Wfiref3h*), scattering length densities (*Parratt32* and *Motofit*) or in mass densities (*IMD* and *LEPTOS*). *IMD* gives the additional possibility to fit on the refractive index n, which allows to fit absorption coefficients as well, an option that is absent in *LEPTOS*. The way how the least-squares routines are implemented are also different. *IMD* gives the possibility to refine using either a Marquardt (CURVEFIT) or a Levenberg-Marquardt (MINPACK-1) algorithm. The algorithm used in *Parratt32* is a simplified one dimensional Newton-Raphson method [130], whereas *Wfiref3h* employs a Levenberg-Marquardt algorithm modified with a dynamical Lagrangian multiplier. *LEPTOS* gives the possibility of four different fitting methods, one based on the Levenberg-Marquardt algorithm, a second one on the simplex algorithm, a third one is a simulated annealing algorithm, and the last one is a genetic algorithm. It is noted that the multi-purpose program *MAUD* [110] has also different algorithms for fitting reflectivity data, *i.e.* apart from the classical method it implements as well the DWBA method and a genetic algorithm. In order to simplify the fits, usually default options were used in the different algorithms. If not, and this applies especially to the optimization boundaries, this is explicitly stated in the following. Table 4.7 gives a non-exhaustive overview of the features of the different programs and methods used in the tests. Several algorithms described in the sections 4.5.2.5, 4.5.2.6, and 4.5.2.9 have been tested using the programs *BA*, *DWBA*, and *LDR*, respectively.

In order to compare the performance of the fits for the experimental data an agreement factor similar to the one used in powder diffractometry was used, but on a logarithmic scale to account for the very large dynamic intensity range.

$$wR = \sqrt{\frac{\sum_i w_i(\log_{10} r_{\mathrm{exp},i} - \log_{10} r_{\mathrm{cal},i})^2}{(\sum_i w_i \log_{10} r_{\mathrm{exp},i})^2}} \tag{4.14}$$

The weighting factors taken in this comparative study were taken $w_i = 1$. In addition a difference curve was constructed as is commonly used in powder diffractograms in order to trace the deficiencies of the model. Depending on the fit and the particularities of the experimental data, the difference curve was traced as either

$$\Delta = \log_{10} r_{\mathrm{exp}} - \log_{10} r_{\mathrm{cal}} \tag{4.15}$$

Table 4.1: Parameters for simulated data[a]

Layer	Re(SLD) (10^{-5}Å^{-2})	Im(SLD) (10^{-7}Å^{-2})	thickness (Å)	roughness (Å)
thin layer (”Si” at 1 gcm^{-3})	0.861	1.99	200	10.00
substrate Si	2.01	4.65		5.00
thick layer (”C” at 1.302 gcm^{-3})	1.11	1.66	3484	1.60
substrate Si	2.01	4.65		9.28

---

[a] for the first sample no gaussian broadening was applied for instrumental resolution effects, in the second case a resolution of 0.001 Å^{-1}.

see e.g. section 4.5.3.4, or it was constructed as for the data in section 4.5.3.5:

$$\Delta = \log_{10} q^4 r_{\text{exp}} - \log_{10} q^4 r_{\text{cal}} \tag{4.16}$$

4.5.3.2 Simulated data.

The simulated data were generated using *Parratt32* following the parameters in Table 4.1. The real and the imaginary components of the nominal scattering length density $\rho = \rho' + i\rho''$ were calculated with help of the NIST Scattering Length Density calculator [129]. The conversion of ρ to the units used in *Wfiref3h*, *viz.* the electronic density ρ_e and the linear absorption coefficient μ_l, was done with $\rho_e = \rho'/r_0$ and $\mu_l = 2\lambda\rho''$. In addition curves were simulated with additional random noise: the noise was linearly varied between 3% at the beginning to 25% at the end of the simulated interval. This can be considered as realistic noise, although in a well-defined experiment the noise can be kept constant and certainly lower than 25% by choosing variable step counting times [91].

The robustness of the algorithms was tested by varying either one of the parameters, while keeping the other parameters fixed at their model values, or by freeing all parameters at once. The substrate SLD was in all cases kept constant. In this case the radius of convergence of the algorithms could be determined in a number of cases. The radius of convergence in multi-dimensional parameter space was somewhat arbitrarily defined as:

$$\tau = \sqrt{\sum_i (\frac{p_i - p_{\text{im}}}{p_{\text{im}}})^2} \tag{4.17}$$

where the p_i define the initial parameters of the model to be fitted, and the p_{im} the model parameters that were used to generate the reflectivity curve to be fitted. For a four-parameter fit, as is the case for a single layer plus substrate system (one density, one thickness, and two roughness values), this means that in order to obtain a certain radius τ all parameters can be taken either $(\tau/2) * 100\%$ larger or smaller than the nominal value. More complicated combinations can be taken ofcourse, but this was normally not done for the sake of simplicity. Classical algorithms based on gradient techniques perform relatively poor having low radii of convergence. The simulated annealing (SA) technique appears

Table 4.2: Multi-parameter fits for the ”thin layer” using different algorithms. [a]

τ	d	ρ	σ_1	σ_2	GA1	GA2[b]	SA[c]	S’plex [d]	*F’4c*	*P32*	*IMD*
0.4	240.0 $\binom{0}{480}$	1.20 $\binom{0}{2.40}$	12.0 $\binom{0}{24}$	8.0 $\binom{0}{16.0}$	yes	yes	yes	yes	yes	yes	no
0.5	250.0 $\binom{0}{500}$	1.25 $\binom{0}{2.50}$	12.5 $\binom{0}{25}$	7.5 $\binom{0}{25.0}$	yes	yes	yes	yes	yes	yes	no
0.5	150.0 $\binom{0}{500}$	0.75 $\binom{0}{1.50}$	7.5 $\binom{0}{15}$	3.75 $\binom{0}{7.5}$	yes	yes	yes	yes	yes	no	no
0.6	260.0 $\binom{0}{520}$	1.30 $\binom{0}{2.60}$	13.0 $\binom{0}{26}$	7.0 $\binom{0}{14.0}$	yes	yes	yes	yes	yes	yes	no
1.0	300.0 $\binom{0}{600}$	1.50 $\binom{0}{3.00}$	15.0 $\binom{0}{30}$	7.5 $\binom{0}{15.0}$	yes	yes	yes	yes	no	yes	no
2.5	450.0 $\binom{0}{900}$	2.25 $\binom{0}{4.50}$	22.5 $\binom{0}{45}$	11.25 $\binom{0}{22.5}$	yes	yes	yes	no	no	no	no
7.0	900.0 $\binom{0}{900}$	4.50 $\binom{0}{9.0}$	45.0 $\binom{0}{90}$	22.5 $\binom{0}{45.0}$	yes	yes	yes	no	no	no	no
10.0	1200 $\binom{0}{2400}$	6.00 $\binom{0}{12.0}$	60.0 $\binom{0}{120}$	30.0 $\binom{0}{60.0}$	yes	no	no	no	no	no	no
10.0	1200 $\binom{150}{1250}$	6.00 $\binom{0.5}{6.5}$	60.0 $\binom{5}{65}$	30.0 $\binom{0}{60.0}$	yes	yes	no	no	no	no	no
15.0	1700 $\binom{0}{3400}$	8.50 $\binom{0}{17.0}$	85.0 $\binom{0}{170}$	42.5 $\binom{0}{90.0}$	yes	no	no	no	no	no	no
15.0	1700 $\binom{150}{1750}$	8.50 $\binom{0.5}{9.0}$	85.0 $\binom{5}{90}$	42.5 $\binom{0}{47.5}$	yes	yes	no	no	no	no	no

---

[a] GA1: Genetic algorithm from *Motofit*; GA2: Genetic algorithm from *LEPTOS*; SA: Simulated annealing algorithm *LEPTOS*; S’plex: Simplex algorithm from *LEPTOS*; *F’4c*: modified Levenberg-Marquardt from Ober (2001); *P32*: Simplex algorithm from *Parratt32*; *IMD* Levenberg-Marquardt from *IMD*. ’yes’ means that the nominal parameters were succesfully recovered; ’no’ means the opposite. The values between parentheses give the lower and upper bounds of the fit for each parameter in the case of the *LEPTOS* and *Motofit* optimizations.

[b] Simplex post-processing was necessary for τ=7, 10, and 15.

[c] Simplex post-processing for τ=7 and upper thickness bound 730 Å for τ=2.5

[d] The upper limits for the thickness values in the simplex optimization were 460, 470, 250, 470, and 500 Å for τ = 0.4, 0.5, 0.5, 0.6, and 1.0, respectively.

to be intermediate between the genetic algorithm and the gradient techniques: the lower and upper bound need to be defined more carefully, *i.e.* more restricted, in most cases. Another disadvantage is that the SA optimization takes considerably more time than the GA’s.

Thin layer. Extended tests were performed using seven different algorithms implemented in five different programs. From the results in Table 4.2 it is clear that the genetic algorithms are by far superior to the other algorithms. The absence or presence of noise does not seem to influence the performances of the algorithms; for all optimizations the outcomes were exactly similar in the case of noise-free and noisy data. The GA’s always find the nominal value, regardles the starting value, when the other parameters are kept fixed at their nominal values. For the gradient methods there is a certain radius of convergence even for one-parameter optimizations. For example, *Firefx4c* has a convergence interval in between 170 Å and 225 Å for a nominal value of 200 Å; in the case of the simplex method from *Parratt32* this is in between 152 and 230 Å. This corresponds to convergence radii of at maximum 0.25. The convergence interval for the thickness has the tendency to become smaller when the density becomes higher. The density and roughness convergence intervals and radii are in general much higher than that for the thickness. This means that in order to do a least-squares or other gradient fit, at least the thickness should be known with some confidence. Luckily the thickness from a monolayer can be estimated with some precision from either the fringe spacing or the Patterson function; this makes that the gradient methods can still be used for simple cases (uniform layers). For the multi-parameter optimizations the SA technique tends to need tighter parameter bounds then the genetic algorithms, whereas the simplex method as implemented in *LEPTOS* needs a tighter bound for the thickness, even at low τ-values, the latter being not necessary for the simplex method from *Parratt32*.

Table 4.3: Multi-parameter fits for the ”thick layer” using different algorithms.

τ	d	ρ	σ_1	σ_2	GA1	GA2
0.5	$435.5 \binom{0}{500}$	$1.66 \binom{0}{2.33}$	$0.2 \binom{0}{4}$	$1.16 \binom{0}{4}$	no	yes
0.5	$400.0 \binom{0}{400}$	$1.79 \binom{0}{2.33}$	$0.2 \binom{0}{4}$	$1.16 \binom{0}{4}$	no	yes
0.5	$261.3 \binom{0}{400}$	$1.00 \binom{0}{2.33}$	$0.12 \binom{0}{4}$	$0.70 \binom{0}{4}$	yes	yes
0.25	$391.9 \binom{0}{400}$	$1.49 \binom{0}{2.33}$	$0.22 \binom{0}{4}$	$1.04 \binom{0}{4}$	yes	yes
0.25	$304.9 \binom{0}{400}$	$1.16 \binom{0}{2.33}$	$0.14 \binom{0}{4}$	$0.81 \binom{0}{4}$	yes	yes
1.33	$367.7 \binom{300}{400}$	$1.25 \binom{1}{1.50}$	$0.50 \binom{0}{2}$	$0.50 \binom{0}{2}$	yes	yes

Thick layer. Classical gradient techniques appear to perform very poorly in the case of a thick layer. Therefore only the results of the genetic algorithms will be discussed in this section. The key parameter for the genetic algorithm in order to have success for the thick layer fit is the upper bound of the thickness. The initial values of the roughness and the density parameters can be set more the less arbitrarily (while keeping the other parameters fixed at their nominal values), but in order to find the nominal thickness value the upper bound is critical. Setting the upper bound at 5000 Å gives only succes if the initial thickness is not farther than 10% of the nominal value. When lowering the upper bound to about 4500 Å (the maximal thickness that can be measured with the D5000 diffractometer) the succes rate increases slightly. With an upper bound of around 4000 Å the GA is capable to find the nominal thickness from an arbitrarily initial value.

For the multi-parameter optimizations the succes rate of the GA for the thick layer is significantly lower than in the case of the thin layer. The radius of convergence τ for the noise-free data seems to be in between 0.25 and 0.50. Table 4.3 gives the succes rate for a number of tests with a different initial set of parameters. Interestingly, with an upper bound of 4000 Å the algorithm is not always capable to find the solution, although some of the final parameters are very close to their nominal values. For example, the optimization of the parameters in the second line of Table 4.3 results in good parameters for the thickness and the substrate roughness, but very bad values for the surface roughness and the density. Of course the succes rate can be improved by a more judicious choice of the lower and upper bounds of the parameters. This can be done by manual fitting, or by an initial estimation of the thickness from the fringe spacing. Even then, however, the GA is not particular powerful in finding the right solution without human intervention. The thickness estimated from 10 fringes amounts to 3677 Å, reasonable starting values for the roughnesses are 5 Å, whereas a reasonable starting value for the density is 1.25 gcm^{-3} with bounds of 1.0 and 1.5 gcm^{-3}, respectively, if it is known at beforehand that the nominal example is based on a experimental example (see also section 4.5.3.6) of a thin polyaniline film. These ”intelligent” starting values (Table 4.3, last line) are not sufficient to find the ”answer” using the GA implemented in *LEPTOS*. The clue is shown in Fig. 4.17; the fringes are particularly well modeled in a large q-range with the final set of parameters, but the first intensity drop at the critical angle of the polyaniline film is very badly modeled. The difference curve immediately shows the structural problem which can be remedied by manual adjustment of the parameters. Restarting the GA from this point does not help to escape from this local miminum, but it is noted that restarting from the values in table 4.3 ($\Delta = 1.33$) eventually lead to the nominal solution. Restarting using the other GA from the same point did not work either. The origin of the problem is that all methods use one cost function which is not equally sensitive to the different parameters in different parts of the reflectogram. A solution would be to use hybrid cost functions, that are linear in the region of the critical angles and logarithmic for larger angles.

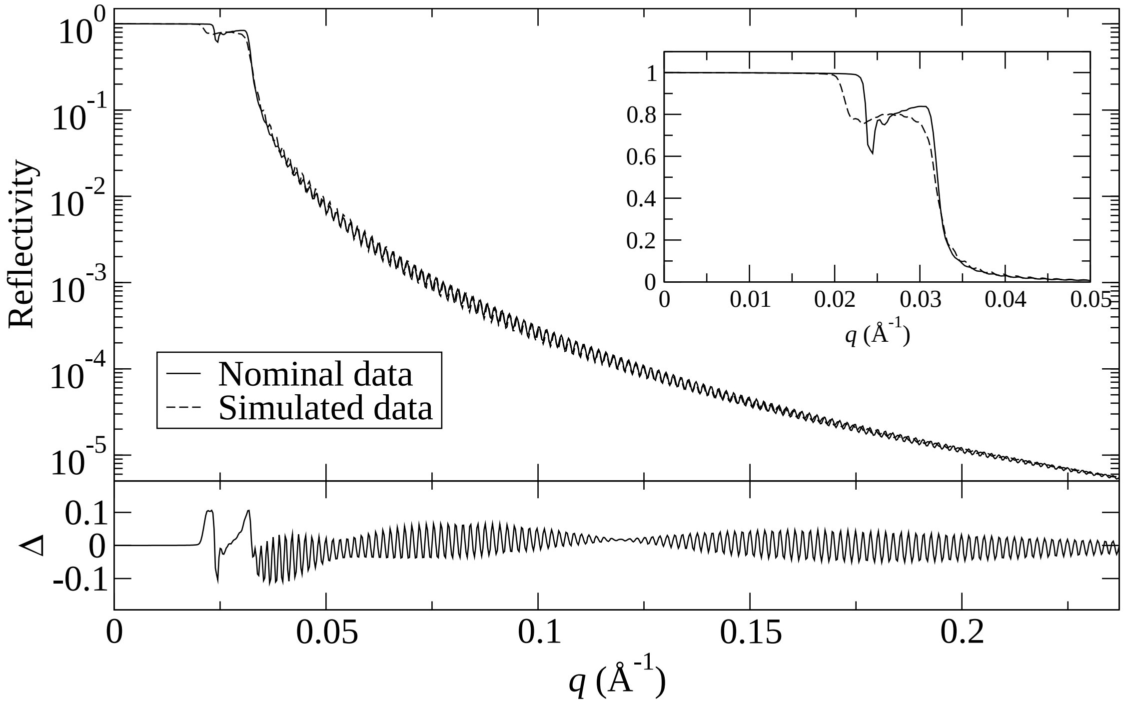

Figure 4.17: Result of the optimization using 'intelligent' starting values for the genetic algorithm (GA1). The inset shows the reflectivity curves in the neighborhood of the critical angles on a linear scale. The lower graph shows the logarithmic difference curve.

4.5.3.3 Experimental data

4.5.3.4 Graphite layer.

The first experimental example, obtained on a thin amorphous carbon layer elaborated by Ionised Physical Vapour Deposition, shows the problems that can arise when the multi-dimensional χ^2 surface is rather flat with relatively shallow minima. Table 4.4 compiles several of the results obtained using different programs; the spread in the parameters is for several programs rather large, showing that the reflectivity curve is rather insensitive to a variation of the different programs. All algorithms, except *IMD*, converge to sensible solutions using the same starting values indicated in the footnotes of Table 4.4. The GA implemented in the *LEPTOS* program is capable to find different local minima using the same starting set of parameters, whereas the GA implemented in *Motofit* always optimizes to the same final set of parameters. The two roughness parameters are found to cluster either around 4 Å or around 8 Å. The gradient-based optimization programs show a similar behaviour: although *Parratt32* and *Ober* converge to a reasonable solution, the final parameter set is rather different.

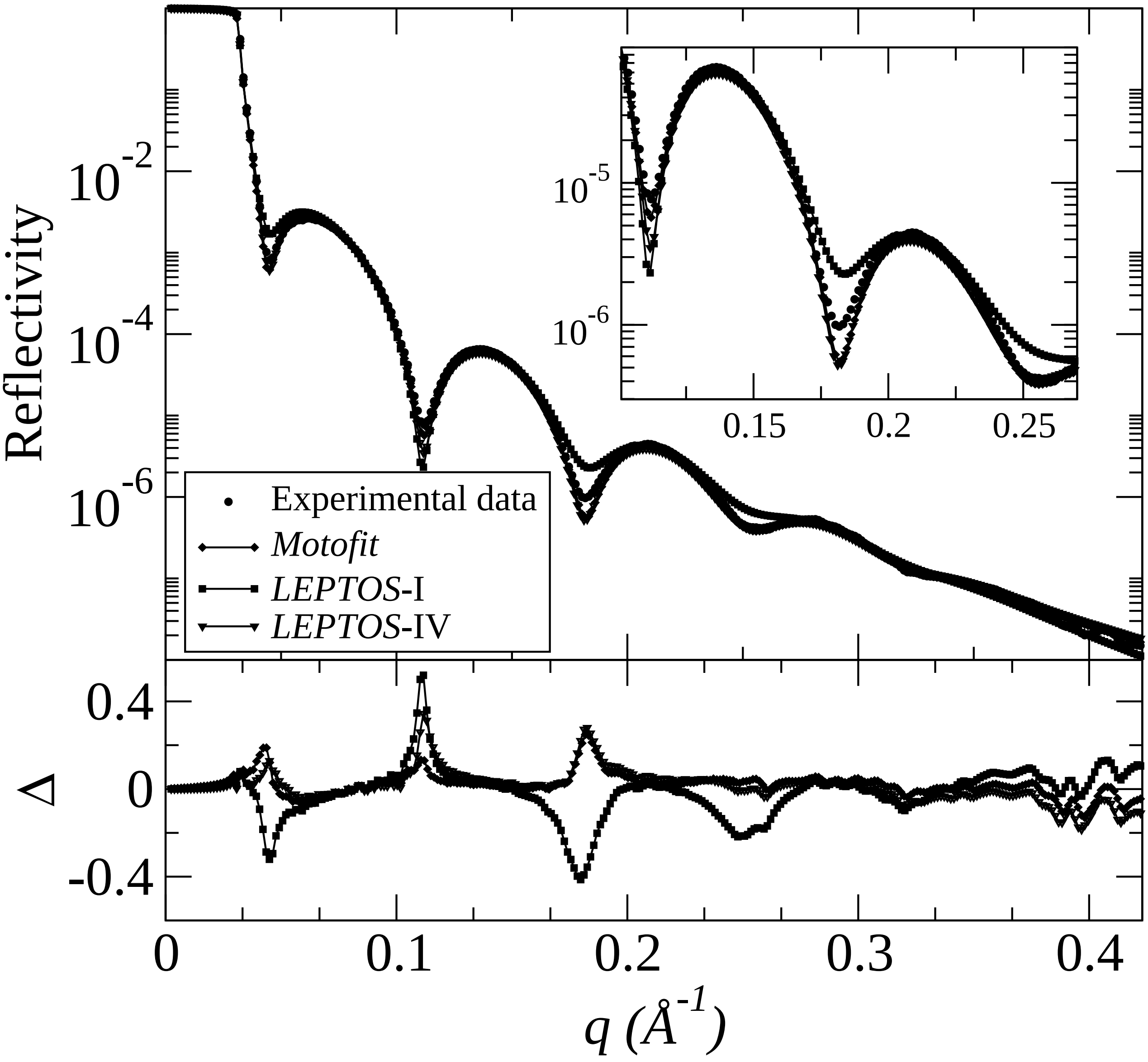

Figure 4.18: Experimental and calculated reflectivity curves for the amorphous carbon layer resulting from optimizations using different programs. The inset is a zoom of the main graph. The lower part gives the difference curves according to Eq. 4.15

Table 4.4: Simulation results for the IPVD carbon layer.[a]

Program	d (Å)	ρ (10^{-5}Å^{-2})	σ_1 (Å)	σ_2 (Å)	wR
IMD[b]	88.0	1.05	4.50	7.67	0.031
LEPTOS-I[c]	86.7	0.93	4.53	9.38	0.020
LEPTOS-II[d]	87.0	1.06	8.48	4.54	0.017
LEPTOS-III[e]	86.4	1.01	4.75	8.12	0.019
LEPTOS-IV[f]	87.6	1.34	9.07	3.75	0.014
LEPTOS-V[g]	87.5	1.07	4.35	9.15	0.037
LEPTOS-VI[h]	87.3	0.97	4.12	8.75	0.033
Motofit	87.3	1.33	8.71	3.86	0.010
Parratt32	87.1	1.32	8.70	3.89	0.014
Ober	87.1	1.22	5.02	7.07	0.037

---

[a] All optimizations were obtained using the following start values and boundaries: $d100=\left(\begin{smallmatrix}50\\150\end{smallmatrix}\right)$; $\rho=1.5\left(\begin{smallmatrix}1.0\\2.0\end{smallmatrix}\right)$; $\sigma_1=5\left(\begin{smallmatrix}0\\20\end{smallmatrix}\right)$;$\sigma_2=5\left(\begin{smallmatrix}0\\20\end{smallmatrix}\right)$. The substrate values are those as in Table 4.1. No instrumental smearing was applied.

[b] The parameters were obtained by manual adjustment.

[c] This result was obtained three times using the GA.

[d] This result was obtained four times using the GA.

[e] This result was obtained twice using the GA.

[f] This result was obtained twice using the GA.

[g] This result was obtained twice using the SA algorithm.

[h] This result was obtained twice using the SA algorithm.

Since the final set of parameters is not conclusive, it is up to the user to make the final decision which set of parameters is most compatible with the experimental data. This decision is not only made on basis of the best χ^2 or wR value and simply a visual inspection of the resulting fits, but also on chemical pre-knowledge of the investigated system. The latter could include measurements of a series of samples prepared under sligtly different conditions. The best parameters could then be those that are coherent with other samples in the series. Fig. 4.18 shows that although the positions of the minima and maxima of the Kiessig fringes are very well fitted, there is a relatively poor fit of the intensity of the minima. It is not certain whether this is due to a wrong set of parameters for a single, homogeneous layer, or whether a second thin layer is present. A better fit can indeed obtained with a slightly less dense layer inserted at the silicon/bulk interface. This is immediately suggested by an *ab-initio* calculation using the program *LDR*. This method can be used, since the condition of Eq. 4.13 is satisfied. Elsewhere it was already shown that carbon layers deposited using cathodic sputtering also present low density layers at the silicon/bulk interface [75].

4.5.3.5 Cadherin monolayers.

A not so easy to fit reflectivity data set is the one obtained using synchrotron data on two-dimensional assemblies of C-cadherins on water [131]. Cadherins are transmembrane proteins involved in cell adhesion; X-ray reflectivity experiments were carried out in order to locate the binding of a short fragment of cadherin on the full-length protein. The data were originally analyzed using *Firefx4c* [88], since classical analysis methods did not give satisfactory results. Fig. 4.19 presents the experimental data. It is a typical example where the original curve does not show many details

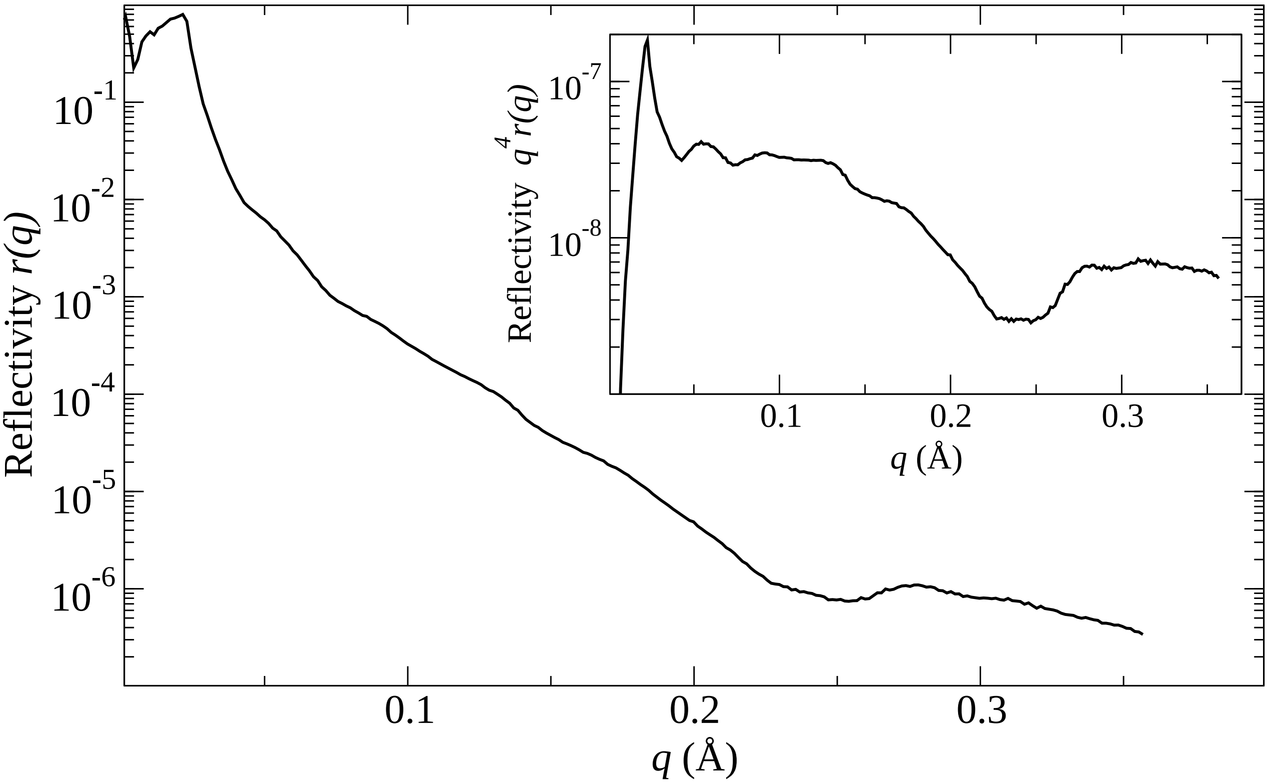

Figure 4.19: Experimental synchrotron reflectivity data of C-cadherin on water. The inset shows the same data, but with the reflectivity multiplied by q^4.

and where it is advantageous to represent the curve as $q^4 r(q)$ *versus* q to highlight the low-angle modulations. These oscillations are indispendable to estimate the total thickness of the film, which is - including the thickness estimated from the high-angle oscillations - about 197 Å. It is noted that the Patterson function of the measured reflectivity gives three weak peaks of approximately the same intensity at 80, 125, and 175 Å, which is not of much help to get initial estimates for the thicknesses. The multislice method *Firefx4c* needs the total thickness as input value, which was taken to be 200 Å from the manual estimation, the number of slices, which is set at 20 to give a slice thickness of 10 Å each, the substrate electronic density, and an initial guess for the slice density which is set to be 20% higher than the substrate density. The resulting SLD profile is shown in Fig. 4.21. For the *ab-initio* phasing method (program *LDR* [115] no input values are required; the resulting SLD profile follows very closely the one obtained using the multi-slice method. The spurious point in the profile is due to inherent instabilities in the inversion step. In view of the SLD profiles obtained, it is reasonable to suppose that it can be at least approximated by a two-layer model, in which the thin top layer corresponds to the lipid monolayer and the thick intermediate layer corresponds to the protein.

The input parameters for the genetic algorithm in *Motofit* and for the different fitting functions in *LEPTOS* were taken to be 175 and 25 Å (the 175/25 starting point) for the two sublayers and as in the multi-slice method equal densities of 20 % higher than that of the H_2O substrate. All three roughness parameters were set at 4 Å. Since in *LEPTOS* the densities have to be given as mass densities represented by a chemical formula, the slabs were defined as hypothetical amorphous carbon layers of varying densities. The absorption coefficients (imaginary parts of the SLD) were fixed in

Table 4.5: wR values and final fit parameters for the cadherin mononolayer reflectivity data using the different programs. [b]

program	M.-S.	GA	S'plex	DWBA	BA	LDR
wR	0.0023	0.0084	0.0107	0.0053	0.0054	0.0132

program	d_1 (Å)	d_2 (Å)	ρ_1 (10^{-5}Å^{-2})	ρ_2 (10^{-5}Å^{-2})	σ_1 (Å)	σ_2 (Å)	σ_3 (Å)
GA	27.7	144.1	1.32	1.04	4.75	0.23	7.12
S'plex	28.4	152.9	1.39	1.12	4.97	0.02	2.99

---

[a] wR is defined in Eq. 4.14; they are calculated starting from q=0.027Å^{-2}. d_1, d_2, ρ_1, and ρ_2 refer to the top layer (1) and the bulk layer (2), respectively. The σ_i are from the air/protein interface (1) towards the bulk/substrate interface (3). GA refers to the genetic algorithm as implemented in *Motofit*, and S'plex to the Simplex routine in *LEPTOS*.

[b] wR is defined in Eq. 4.14; they are calculated starting from q=0.027Å^{-2}. d_1, d_2, ρ_1, and ρ_2 refer to the top layer (1) and the bulk layer (2), respectively. The σ_i are from the air/protein interface (1) towards the bulk/substrate interface (3). GA refers to the genetic algorithm as implemented in *Motofit*, and S'plex to the Simplex routine in *LEPTOS*.

the other programs, since *LEPTOS* does not allow the refinement of the absorption. The parameters in both *Motofit* and *LEPTOS* were constrained between 0.0 and twice the starting value, except for the roughness parameters which were allowed to vary between 0 and 30 Å. The resulting profile (Fig. 4.21) is again not far from the two other profiles and coincides in addition with the high apparent substrate-film roughness. The pre-knowledge of the thickness values and the order in which the layers appear, is important, but not primordial for the genetic algorithm in *Motofit* in order to find a reasonable solution that is compatible with the multi-slice and the *ab-initio* methods.

In order to test the behaviour of the genetic algorithm a different starting point was chosen with two equal thickness values at 100 Å (the 100/100 starting point). In addition the optimizations were repeated several times against $\log r(q)$ or $q^4 r(q)$ as Convergence (at 0.05%) was always reached within the first 200 generations. It was found that optimizing against $q^4 r(q)$ always produced a solution in reasonable agreement with those of the two other methods, but differing notably in the value of the substrate/film thickness. On the other hand, optimizing against $\log r(q)$ produced in approximately 20% of the cases with both of the starting points an alternative solution with two very thin layers of about 25 Å. Refining the genetically optimized solutions using the Levenberg-Marquardt algorithm always yielded unphysical solutions with extremely high substrate/film roughness values and much too high thickness values.

Optimizations with both the genetic algorithm and the simulated annealing implemented in *LEPTOS* were much less succesful than the genetic algorithm in *Motofit*. In fact the two methods never gave a succesful solution in 5 consecutive runs, but only unphysical profiles with moderate fits. Surprisingly, the Levenberg-Marquardt and the Simplex algorithms performed very well within *LEPTOS*; the Simplex algorithm converged to the right solution for both the 100/100 and the 175/25 starting point, whereas the LM algorithm gave the right solution for the 175/25 starting point. It is noted that neither *IMD*, nor *Parratt32*, was capable to converge to a good fit between experimental and calculated reflectivity using the same starting points.

The DWBA and BA optimizations gave correct solutions after only a short calculation time with fits that are comparable with that of the multislice-method. This is maybe not surprising although the mathematics underlying the three methods are very different. In all three cases, however, the total film thickness is divided into the same number of sub-slices compatible with the resolution of the experiment.

Fig. 4.20 gives the results of the optimizations as $q^4 \log r$ *versus* q plots, since with this representation the details of the fits are most easily visible. The lower part of the figure gives the difference curves. The most perfect fit is given by the multi-slice method, whereas the DWBA and BA methods yield problems at very high angles. It is noted that the different programs do not treat the reflectivity below the critical angle in the same way, so that the differences in that region are very important; they have been omitted in the lower part of Fig. 4.20 and also in the calculation of the residual factors. The structural information resides, not in that region, so that the influence of a wrong fitting at very low angles is marginal. The LDR method, the only method without any adjustable parameters, should give in theory a perfect fit - $wR \equiv 0$ -, which is however not the case. This is due to the fact that the phasing procedure is inevitably truncated, because of the limited resolution of the experiment, and also because the inversion procedure is inherently ill-conditioned. The methods that use only two sub-layers for the optimization, *i.e.* the genetic algorithm and the simplex method, have deficiencies in the entire q-range. Table 4.5 gives the different parameters found for these two fits and Figure 4.21 gives the resulting density profiles for all methods. It is seen that the all methods give qualitatively the same density profile, *i.e.* a rather thin, but dense top-layer, and a much thicker but less dense bulk layer. The methods havinRefractiveindexcomplexqg given very different profiles and worse fits are omitted from the discussion. Note that the Simplex method gives much denser top and bulk layers than all other methods. The fact, however, that a number of very dissimilar algorithms give approximately the same profile, gives confidence that the actual profile is qualitatively correct.

4.5.3.6 Thick polyaniline layers.

Thick polyaniline layers for ammonia sensor purposes have been elaborated and characterized by different techniques, amongst them X-ray reflectivity; detailed results will be presented elsewhere (Mérian *et al.*, 2007). The example has been chosen because it represents a ”thick” sample compared to the foregoing examples, which appears to be more difficultly analysed using automatic fitting routines than the thin samples. Optimizations using idealized data based on the best fit performed with *LEPTOS* have been discussed in section 4.5.3.2. The genetic algorithms do not appear to have much difficulty in finding the best solution using the ”intelligent” start values discussed in section 4.5.3.2. It is however not at all possible to use these start values using the classical programs; manual adjustment until the calculated and the experimental curves nearly coincide is necessary before optimization using a gradient method becomes possible.

It is interesting to see what the spread in parameters is using the different approaches using the same experimental file. The fits were performed - depending on the program - by a course optimization using a GA or by manual adjustment, followed by gradient optimization. Table 4.6 summarizes the fit parameters using the different programs. The thickness and the SLD parameters are determined with high confidence, whereas there is some more spread in the values of the roughness parameters. Although an ”automatic” fit appears to be a bit more difficult than for the thin carbon layer, the final parameter dispersion is less important than in the case of the thin layer.

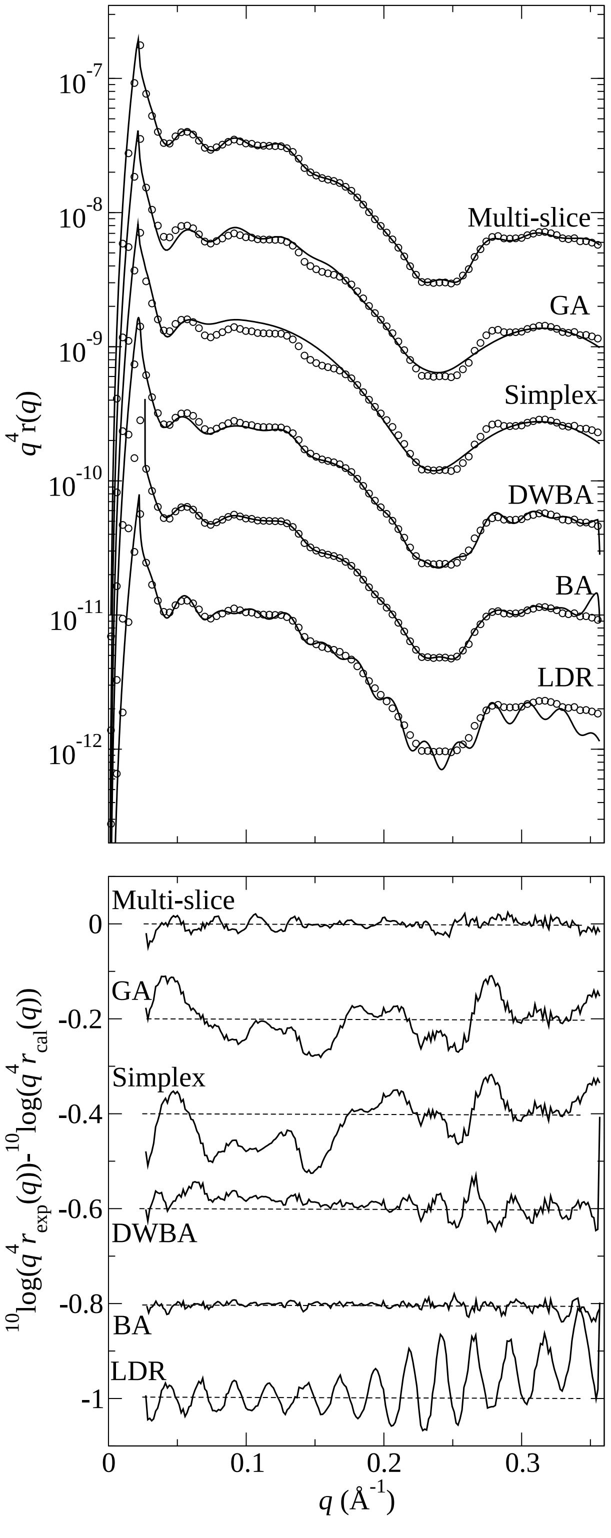

Figure 4.20: Best fits for the cadherin reflectivity data using 6 different algorithms. The upper part gives the experimental data as small open circles and the simulated data as solid lines. The different fits are shifted by a factor of 5 for the sake of clarity. The lower part of the figure gives the logarithmic difference curves for the six fits in the same order. They are each shifted by a factor of 0.2. The dashed horizontal line represent the zero-line for each difference curve.
©*A. van der Lee (IEM)*

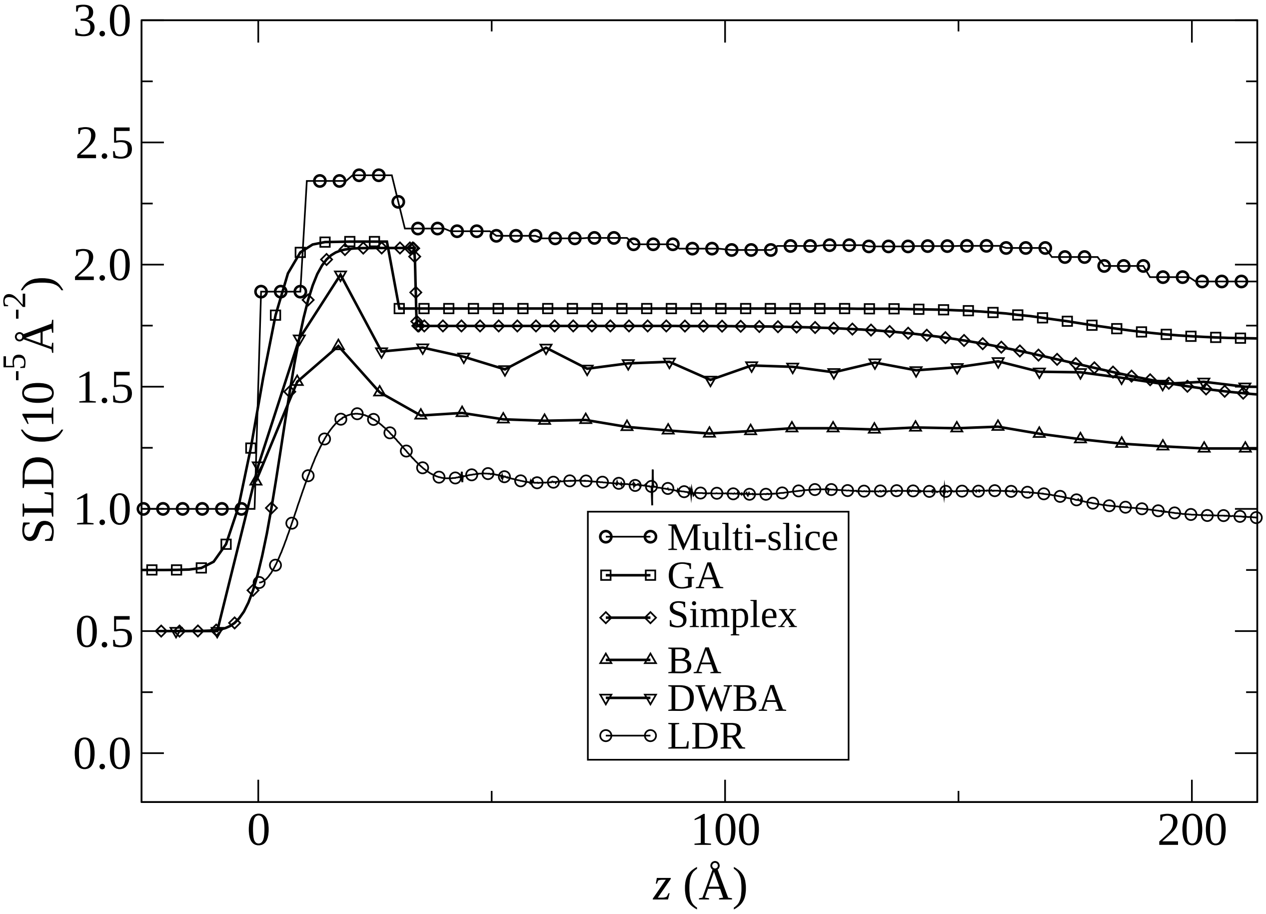

Figure 4.21: Scattering length density profiles obtained using three different methods. The profiles have been shifted by 10^{-6} Å^{-2} for the sake of clarity. Note that the spurious point in the *ab-initio* profile is not due to the phasing procedure, but rather to the dynamical inversion (layer-stripping) algorithm.

4.5.4 Discussion

The question what the best fitting method is, is rather delicate, since it appears that neither method which have been tested here gives a ”best” profile, for an unknown system. From a methodological point of view it seems that the phase determination methods proposed by Majkrzak & Berk or Aktosun & Sacks are by far preferable, since they give the ultimate solution to the phase problem in scattering. There are, however, several disadvantages to their method, which makes it difficult to apply it routinely. The first is that either a very well-known reference layer, or a variation of the surrounding medium is needed. In many cases it can be questioned whether the presence of a reference layer or another fronting medium does not alter the actuel system to be studied. Secondly, once the phase has been found, the complex reflectances must be inverted, which can be done either by the inverse Fourier transform in the Born approximation, or dynamically by the layer-stripping method. In either case information is lost: for the Fourier transform because data are truncated and the Born approximation is not valid in the vicinity of the critical angle, and for the layer-stripping method, because it is inherently ill-conditioned, which makes it difficult to apply for thicker films. In addition, its results

Table 4.6: Final fit parameters for the "thick" polyaniline sample using the different programs. [a]

program	d (Å)	ρ (10^{-5}Å^{-2})	σ_1 (Å)	σ_2 (Å)
LEPTOS[b]	3484	1.11	1.60	9.28
Motofit[c]	3484	1.12	2.75	8.19
Parratt32[d]	3485	1.13	2.81	8.61
IMD[e]	3490	1.12	1.51	9.85

---

[a] The absorption was kept constant in all programs at $1.66.10^{-8}$, calculated from the *LEPTOS* density and composition ("amorphous carbon") and converted by the SLD calculator (NIST, 2007); the programs from Ober (2001) could not be used for these fits, since the number of calculated points is limited at 200, which is not sufficient to describe in sufficient detail the Kiessig fringes.

[b] ρ converted using NIST SLD calculator.

[c] GA followed by LM.

[d] The intial parameters had to be set very close to the final solution.

[e] The initial parameters were set at those found by *LEPTOS* and then refined using the LM algorothm; ρ converted using NIST SLD calculator.

deteriore when absorption becomes important.

The experimenter thus wants to have as much information from single measurement methods as possible. The methods discussed in this paper have all their advantages and shortcomings, but some guidelines can be given anyhow. It appears that the genetic algorithm is in particular well adapted to optimization problems in the field of reflectivity. The exact implementation of the algorithm, however, seems to have an influence on especially experimental data. The two genetic algorithms tested here perform equally well for calculated data without noise and relatively thin layers, but for experimental data and also for thick layers the one performs better than the other. Surprisingly, the genetic algorithm can be trapped into local minima, although the capability to escape from local minima is normally considered to be one of the strong points of the GA. Classical methods, such as the Levenberg-Marquardt or Simplex method are less well adapted for these problems, although a particular implementation of the Simplex method yielded surprisingly good results in the case of experimental data. The simulated-annealing algorithm was disappointing for experimental data.

The problem that the experimenter initially faces is how many layers he or she should take to fit the data correctly. As was demonstrated in the case of the cadherin layers, the answer is not always readily provided by the Patterson function, but should be guessed by a judicious analysis of the data and chemical or physical pre-knowledge of the system. In case of doubt, four methods are in particular helpful, *i.e.* the multi-slice, the DWBA, the BA, and in certain cases, the LDR method. They have the ability to detect either small modulations on an otherwise constant SLD, or to detect large low-contrast bulk layers as was demonstrated in section 4.5.3.3. Even when the final profile is noisy, as is especially the case with the DWBA approach, then still these approaches can give an idea how to model the system better with a limited number of slices. The analysis can then be finalized using classical analysis techniques, such as the Levenberg-Marquardt or Simplex method.

For not so straightforward problems the use of different algorithms can be an advantage to ascertain that the resulting profile is at least qualitatively correct. It is important, however, to remember that in reflectometry two or even more different profiles can give the same reflectivity curve. This is easy to show using the BA (see also Lu *et al.*, 1996).

Table 4.7 summarizes the main characteristics of the different programs. For manual fitting *LEPTOS* and *IMD* are superior to the other programs, since they have particularly well defined graphical user interfaces The GA implemented

Table 4.7: Features of the used programs.[a]

program	*IMD*	*LEPTOS*	*Motofit*	*Parrat32*	*Firefx4c*
data format	(θ, r)	$(2\theta, r)$ or (q, r)	(q <TAB> r)	(q <TAB> r <TAB> e)[b]	(q, r), (θ, r)
algorithms	LM	LM, simplex, GA, SA	LM, GA	Simplex	modified LM
speed of algorithm[c]	f	f,f,f,s	f,f(s)[d]	m	m
manual adjustment[e]	e	e	c	c	c
absorption refinement	yes	no	yes	yes	yes
composition refinement	yes	no	no	no	no
analytical function	no	no	no[f]	yes	no
density representation	mass, n	mass	SLD	SLD	electronic
geometric correction	no	no	no	no	no
initial thickness estimation	by fringe spacing	none	Patterson/fringe spacing	none	none
weighting methods	different	one	different	different	different
off-specular calculations/fitting	yes	no	no	no	no
roughness models	more	1	1	1	1
offset and scaling	yes	yes	no	no	no
free	yes	no	yes	yes	yes

---

[a] The programs *LDR*, *DWBA*, and *BA* do not possess a graphical user interface and are too different from a mathematical point of view (because they are not based on a simple slab model with adjustable parameters for each slab).

[b] e denotes the standard deviation

[c] f: fast; m: medium; e: slow

[d] slow when data are convoluted using user-supplied resolution values

[e] e: easy; c: cumbersome

[f] This can in principle be done, but built-in functions are not available

in *Motofit* seems to be the best performing minimizing algorithm . Every program has its own features that make it difficult to compare it to other progams. *Motofit* is customizable in the sense that the source code is free and that user modules can be added. Interestingly, most programs produce in most of the cases equal reflectivity curves using equal model parameters, although a comparison between *LEPTOS* that uses chemical compositions and internally tabulated absorption coefficients and programs where complex SLD's are used is not always easy. Another factor that can create differences in the reflectivity curves is the way how the instrumental resolution function is convoluted with the calculated curve and another parameter that can influence the curves differently is the exact roughness model.

Software traceability is indeed an important issue in metrology; Bowen and Deslattes already suggested [132] that different approximations, but also simply programming errors could lead to different calculated diffraction or reflectivity curves. Fig. 4.22 shows that this is indeed the case: the parameters used for the calculation are again inspired by the thick polyaniline sample, see Table 4.1. The resolution function was taken to be equal to a gaussian function with a half width of 0.001 $Å^{-1}$. The calculation method in *Parratt32* is not specified ("constant resolution at q_z=0"). For *Motofit* a point-to-point gaussian convolution was used with a constant resolution of 0.001 $Å^{-1}$. For *LEPTOS* and *IMD* optimal values of the resolution function were sought by comparing the amplitudes of the fringes with those calculated by *Parrat32*, since convolving at constant q is evidently not identical to convolving at constant θ. For *LEPTOS* $\Delta 2\theta = 0.008^{\circ}$ was used; for *IMD* $\Delta\theta = 0.004^{\circ}$. Fig. 4.22 shows the reflectivity in the vicinity of the critical angles; the Kiessig fringes are nearly identically calculated. It is shown that the two programs that use chemical compositions to define the layer, *viz. LEPTOS* and *IMD*, yield practically the same reflectivities. On the other hand, the programs that use SLD's for the specification of the layer, *viz. Parratt32* and *Motofit* are rather different, meaning that the "conversion" of the chemical composition into SLD values using the NIST SLD calculator is not correct; different sources of absorption coefficients are apparently used. The difference between the *Parratt32* and *Motofit* curves stems obviously from a different implementation of the

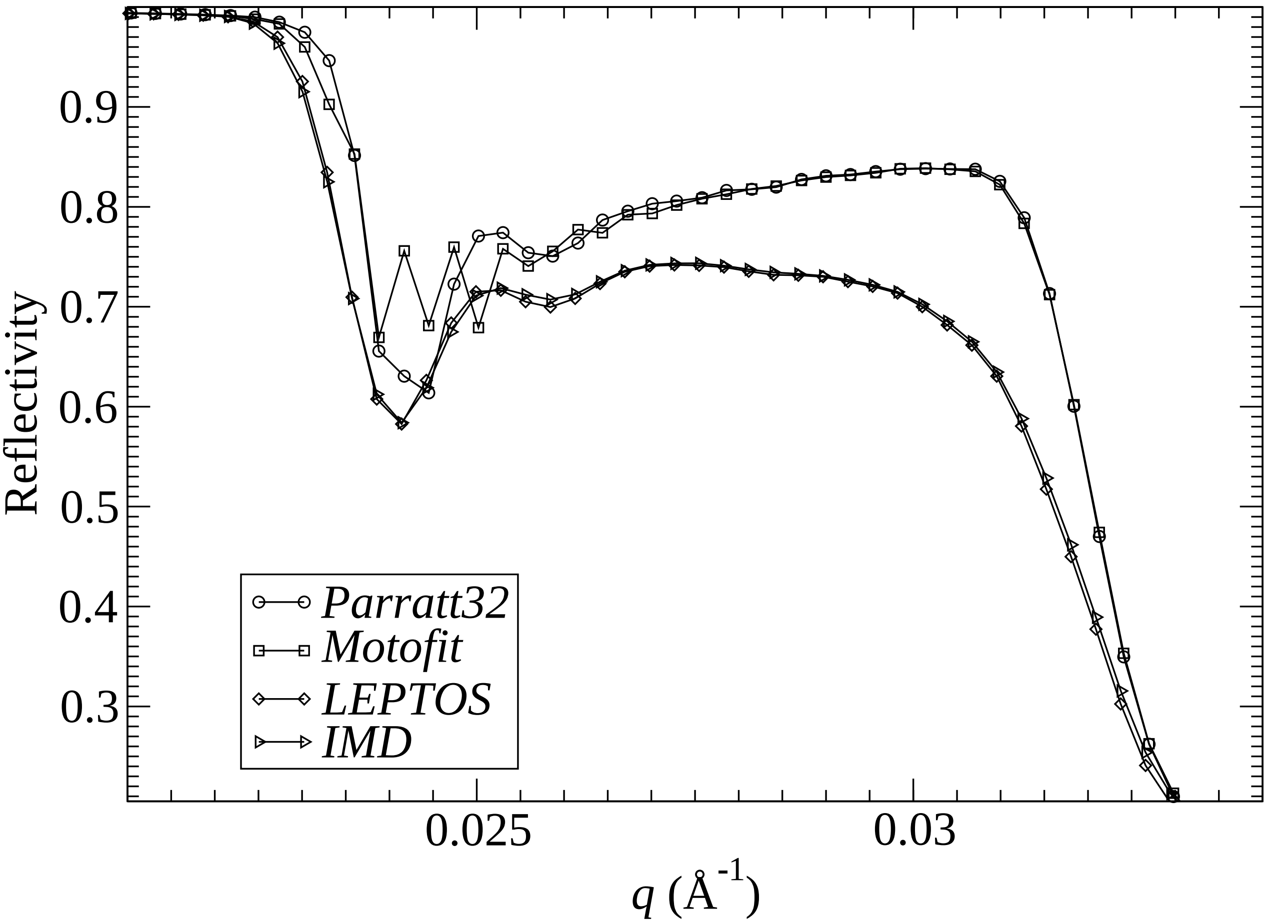

Figure 4.22: Theoretical reflectivity curves for the ”thick” polyaniline layer, calculated using different programs.

convolution subroutine.

4.5.5 Conclusion

Fitting methods for reflectivity data based on a variety of mathematical techniques have been described and compared with respect to their performance in a variety of situations using simulated data with and without noise, and using experimental data. The genetic algorithm is superior to all other methods - in the absence or the presence of more or less significant noise - when the system to be modeled is simple and relatively thin, *i.e.* one or two well-defined and homogeneous layers. Relatively thick films are rather difficult to model even with the GA, as long as the cost function is not adaptable. Human intervention remains necessary in these cases, to account for the different sensitivity of the different parameters in different q-ranges. In contrast, alternative methods, such as the iterative BA method, the least-squares DWBA or multi-slice methods, or the *ab-initio* LDR method become the priviliged methods as soon the genetic algorithm does not give a satisfactory fit or physical model. The latter methods could give at least an idea how the system can be modeled with a limited number of layers, or hints to the existence of density gradients. Once this information has been acquired, the fit can be finalized by classical gradient methods such as the Levenberg-Marquardt or the Simplex method. It was found as well that the exact implementation of a particular method can have an influence on the performance. The use of different programs is thus advised if one particular program fails to give a satisfactory fit. Unfortunately no program suite exist that couples the different fit techniques that have been described here; in particular the BA, DWBA, and LDR analysis methods are not easily accessible for the non-programmer. It can be expected, however, that especially the BA method will attract new interest for reflectivity analysis in view of the success of the analogous charge flipping method in single-crystal and powder diffraction.

It was found that the different programs do not calculate the same reflectivity for especially thicker samples, where the calculated reflectivity has to be convolved with an instrumental resolution function, but also when absorption is involved. The reason in the latter case is that in some programs the absorption parameters are not directly visible, because the layers are specified in terms of their chemical composition. It is preferable that the layers are specified in terms of their complex scattering length density (or eventually electronic density) so that this source of confusion at least can be avoided.

Acknowledgements O. Briot (Groupe d'Étude de Semiconducteurs, Montpellier) is thanked for giving the possibility to work with the Bruker *Leptos* software. J.-F. Legrand (Institut Charles Sadron, Strasbourg) has kindly put at our disposal the synchrotron data of the reflectivity experiments on the cadherin monolayers and T. Mérian and D. Debarnot have synthesized the polyaniline layers (Laboratoire Polymères - Colloïdes - Interfaces, Le Mans) and given permission to use the data for this study.

4.6 Chemical information from single-wavelength X-ray reflectivity data

The possibilities for extracting chemical composition-related information from a single-wavelength X-ray reflectometry experiment are investigated. It is shown that the X-ray absorption of certain elements is sufficient to cause a significant effect on the reflectivity curve, which can be in turn exploited to determine its abundance in the thin film. The limitations are discussed using simulated data and the methodology is applied for the determination of the iodine concentration in thin polyaniline films. More generally the method appears to be very sensitive for the non-destructive determination of the weight percentage of metal nanoparticles in thin polymer films.

4.6.1 Introduction

X-ray reflectivity is commonly used to determine the electron density profile across a thin film. Since the interaction of the incident X-ray photons with the electrons of the thin film is dominantly elastic, information about the chemical nature of the thin film structure can hardly be obtained. In single-crystal X-ray diffraction chemical sensitive information is usually obtained by an (automatic) inspection of the electron density map: the height of the electron density maximum is proportional to the atomic number Z, where the interpretation is assisted by the distance between different maxima which are often characteristic for bond distances between atoms of the same or different type. This kind of interpretation can hardly be applied in the case of X-ray reflectometry, although the electron density is - like in single crystal diffraction - directly related to the chemical composition of the film (neglecting absorption):

$$\rho_{\mathrm{e}} = N_{\mathrm{A}}\rho_{\mathrm{m}}\frac{\sum c_j(Z_j + f'_j)}{\sum c_j A_j}, \tag{4.18}$$

where N_{A} is Avogadro's number, ρ_{m} the mass density, Z_j and A_j the atomic number and mass for element j, respectively, c_j the atomic proportion of element j, and f'_j the dispersion correction of element j. It is clear that Eq. 4.18 cannot be solved, since although Z_j, A_j, and f'_j are obviously known for given j, j itself, c_j and ρ_{m} are basically the unknown parameters for one known parameter, ρ_{e}, supposing that the phase problem of X-ray reflectivity has been conveniently solved. In practice of course, chemical information may be partly or entirely present, and if entirely, Eq. 4.18 gives a means to calculate the mass density from the electronic density. Partial information usually means that either one or more c_j coefficients and/or the mass density ρ_{m} are not known exactly, for instance in the case of chemical or physical deposition techniques where the exact composition is not exactly controlled, in thin layers where interdiffusion processes take place, or in porous layers, where the mass density of the entire layer does obviously not correspond to that of the bulk material.

The most obvious way to determine chemical sensitive information from X-ray reflectivity data is by exploiting the phenomenon of X-ray absorption, which is very element specific. The photoelectric absorption in the X-ray range of wavelengths is accounted for by an imaginary term in the expression for the refractive index:

$$n = 1.0 - \delta + i\beta = 1.0 - \frac{\lambda^2 r_0}{2\pi}N_{\mathrm{A}}\rho_{\mathrm{m}}\frac{\sum c_j(Z_j + f'_j - if''_j)}{\sum c_j A_j}, \tag{4.19}$$

where λ is the wavelength and r_0 the Thomson length of the free electron. It is recalled that the imaginary component of the anomalous dispersion scattering factor f''_j is directly related - outside the absorption threshold regions - to the atomic photoabsorption cross section σ_{pe} ($= 2r_0\lambda f''_j$), but usually the mass attenuation coefficient $\mu_{\mathrm{m},j} = N_{\mathrm{A}}\sigma_{\mathrm{pe},j}/A_j$ is tabulated [133], which gives thus for f''_j:

$$f''_j = \frac{\mu_{\mathrm{m},j}A_j}{2N_{\mathrm{A}}r_0\lambda}, \tag{4.20}$$

yielding for the absorption contribution β to the refractive index:

$$\beta = \frac{\mu_{\mathrm{l}}\lambda}{4\pi} = \frac{\lambda\rho_{\mathrm{m}}}{4\pi}\frac{\sum c_j A_j \mu_{\mathrm{m},j}}{\sum c_j A_j} \tag{4.21}$$

where μ_{l} is the linear absorption coefficient of the multi-element compound. Typical values for δ are around 10^{-6}, whereas for β these are around 10^{-8}, thus about 100 times smaller. It is noted that both f'_j and f''_j depend on the energy wavelength, especially in the vicinity of absorption edges. The wavelength dependence of f'_j is used in anomalous X-ray reflectivity experiments, where from two experiments at different wavelengths, one near the edge and the other away from the edge, the concentration profile of the absorbing element can be determined [123, 124, 134].

In this report we discuss how the value of f''_j can be used to determine the unknown atomic concentration c_Z of a known species Z in an otherwise known compound $A_xB_y\cdots Z_c$ using a single-wavelength X-ray reflectivity experiment. Some work in this direction has already been done [106], but that was aimed more at an accurate determination of the mass density for a partially unknown composition. Here we outline the practical aspects of the methodology and we will discuss as well its limitations.

4.6.2 Methodology

From Eq. 4.18 and 4.19 it is clear that in the presence of absorption the electron density is a complex quantity $\rho_\mathrm{e} = \rho'_\mathrm{e} + i\rho''_\mathrm{e}$ where the real and imaginary parts can be defined as:

$$\rho'_\mathrm{e} = N_\mathrm{A}\rho_\mathrm{m}\frac{\sum c_j(Z_j + f'_j)}{\sum c_j A_j}, \quad \rho''_\mathrm{e} = N_\mathrm{A}\rho_\mathrm{m}\frac{\sum c_j f''_j}{\sum c_j A_j}. \tag{4.22}$$

Defining $Z_j^\mathrm{eff} = Z_j + f'_j$ as the effective atomic number of element j, we obtain from Eq's 4.20 and 4.22:

$$\frac{\rho''_\mathrm{e}}{\rho'_\mathrm{e}} = \frac{\sum c_j A_j \mu_{\mathrm{m},j}}{2\lambda r_0 N_\mathrm{A} \sum c_j Z_j^\mathrm{eff}}. \tag{4.23}$$

Supposing that we have an N-element compound, for which the atomic fraction for $N-1$ elements is known, then we can extract the atomic fraction c_Z of the Nth element Z from Eq. 4.23 as follows:

$$c_Z = \frac{2\lambda\rho''_\mathrm{e} r_0 N_\mathrm{A} \sum_{j=1}^{N-1} c_j Z_j^\mathrm{eff} - \rho'_\mathrm{e} \sum_{j=1}^{N-1} c_j A_j \mu_{\mathrm{m},j}}{\rho'_\mathrm{e} A_Z \mu_{\mathrm{m},Z} - 2\lambda\rho''_\mathrm{e} r_0 N_\mathrm{A} Z_Z^\mathrm{eff}}. \tag{4.24}$$

Note that Eq. 4.24 does not contain ρ_m, which is unknown, and that the two parameters to be determined from the experiment are ρ'_e and ρ''_e. The other parameters in Eq. 4.24 are tabulated.

4.6.3 Results

We tested Eq. 4.24 on polyaniline doped with iodine. Polyaniline is a widely studied conducting polymer which has numerous applications such as its use as electrochromic smart windows, electrically conductive transparent foils, conductive high performance fibers, and its protection against electrostatic discharges. Here polyaniline coatings are used as optical sensors that measure absorbance change under gas adsorption [135]. More precisely, polyaniline thin films are doped with iodine to make them sensitive to ammonia gas. X-ray reflectivity was used to characterize the thin polyaniline films before and after iodine treatment. Details about the preparation of the thin films, the iodine treatment, and further physico-chemical characterization will be given elsewhere.

The X-ray reflectivity measurements were carried out on a Bruker D5000 diffractometer equipped with a special reflectivity stage, which limits the beam footprint on the sample with a knife-edge in the center of the goniometer and which was typically set at 15 μ above the sample surface. Graphite monochromatized Cu-$K\alpha$ radiation was used ($\lambda = 1.5405$ Å) and the data were reduced following the procedures described elsewhere [91]. A number of different samples deposited on silicon was investigated according to different reactor parameters for the plasma polymerization process. Fig. 4.23 gives the reduced experimental reflectivity curves for each sample before and after iodine treatment.

Table 4.8: Parameters used for the fits and the calculations using Eq. 4.24

element j	Z_j	f'_j	A_j	$\mu_{m,j}$ (cm^{2}g^{-1})	c_j
C	6	0.018	12.011	4.51	12
H	1	0.000	1.008	0.391	8
N	7	0.031	14.01	7.44	2
I	53	-0.326	126.9	288.0	c_I

Table 4.9: Fit results for four different polyaniline films before and after iodine treatment ('I'-suffix)

sample	d (Å)	ρ'_e (eÅ^{-3})	ρ''_e (10^{-2}eÅ^{-3})	σ_1 (Å)	σ_2 (Å)	c_I
TM70a	3484	0.391	0.07	2.7	8.2	-
TM70c	2854	0.395	0.07	4.1	7.4	-
TM70d	3523	0.390	0.07	10.1	2.5	-
TM70e	1639	0.405	0.09	5.2	9.0	-
TM70aI	3484	0.59	2.3	7.2	8.5	0.73
TM70cI	2854	0.60	2.4	6.4	8.4	0.74
TM70dI	3523	0.52	2.1	9.4	4.5	0.77
TM70eI	1639	0.58	2.1	10.5	8.8	0.65

It is clear - in view of the drastic changes around the critical angle - that the treatment has a large impact on the densities of the film. Moreover, the interfacial roughness increases, which makes the Kiessig fringes disappear. The latter could also be due to the introduction of lateral inhomogeneities during the iodine treatment. The analysis of the curves was done using *PARRATT32* [87] and *MOTOFIT* [128] using the parameters in Table 4.8 and resulting in fit parameters compiled in Table 4.9. The thickness of the thin film after iodine treatment was kept the same as found before treatment, although in reality there may be some swelling. The determined c_I values are in reasonable agreement with those determined from XPS (0.89 and 0.35 for a and e, respectively), but the accuracy could be higher if the surface quality of the iodine-treated samples had been better.

Since the effect of photoabsorption on the refractive index is expected to be approximately 100 times smaller than that of Thomson scattering, the need for accurate data can be very stringent for a precise determination of ρ''_e. This is especially true if the electron density of the film to be investigated is larger than that of the substrate, but the necessity for accurate data can be relaxed slightly if the electron density of the film is smaller than that of the substrate. In the latter case the x-ray path length through the film is drastically lengthened because of the very grazing angles, which enhances the absorption of the X-rays inside the film and at the same time the effect on the observed reflectivity. We show here by various simulated examples which reliability can be given to the determination of the iodine concentration in the last section, in which cases the method has potential applications, and also when the use of Eq. 4.24 reaches its limits.

The first example is similar to that of the foregoing section. Fig. 4.24 gives the calculated reflectivity for a 750 Å thin polyaniline-like film on Si, that of an iodine-doped film, $c_I = 0.4$, and that of a similarly doped film, but with

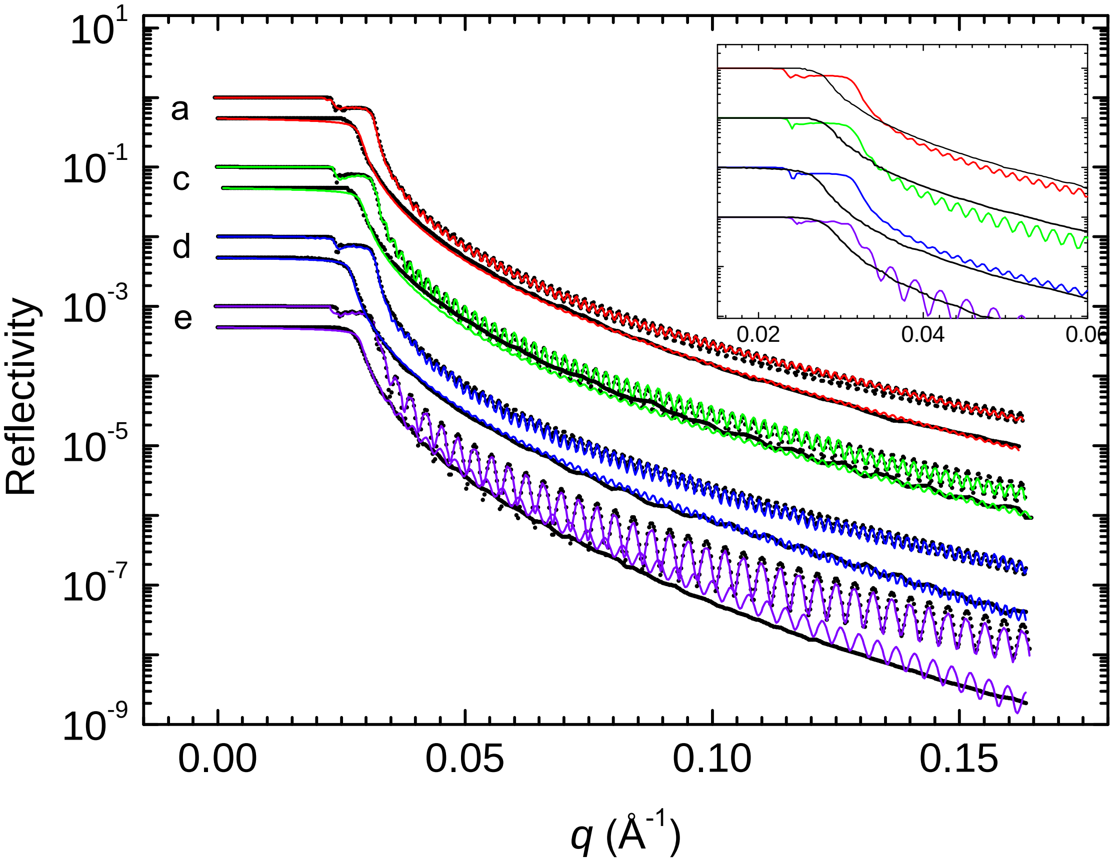

Figure 4.23: Experimental reflectivity for four different polyaniline film before and after iodine treatment. The suffixes 'a-e' refer to the four different samples in Table 4.9. The lower curve for each sample is the one which was treated with iodine. The simulated curves (full lines) overlay the experimental curves (small dots). The curves have been shifted for clarity. The inset shows the experimental reflectivity (full lines) around the critical angle for the four samples in the same order as in the main graph, but with the non-treated and treated samples non-shifted.

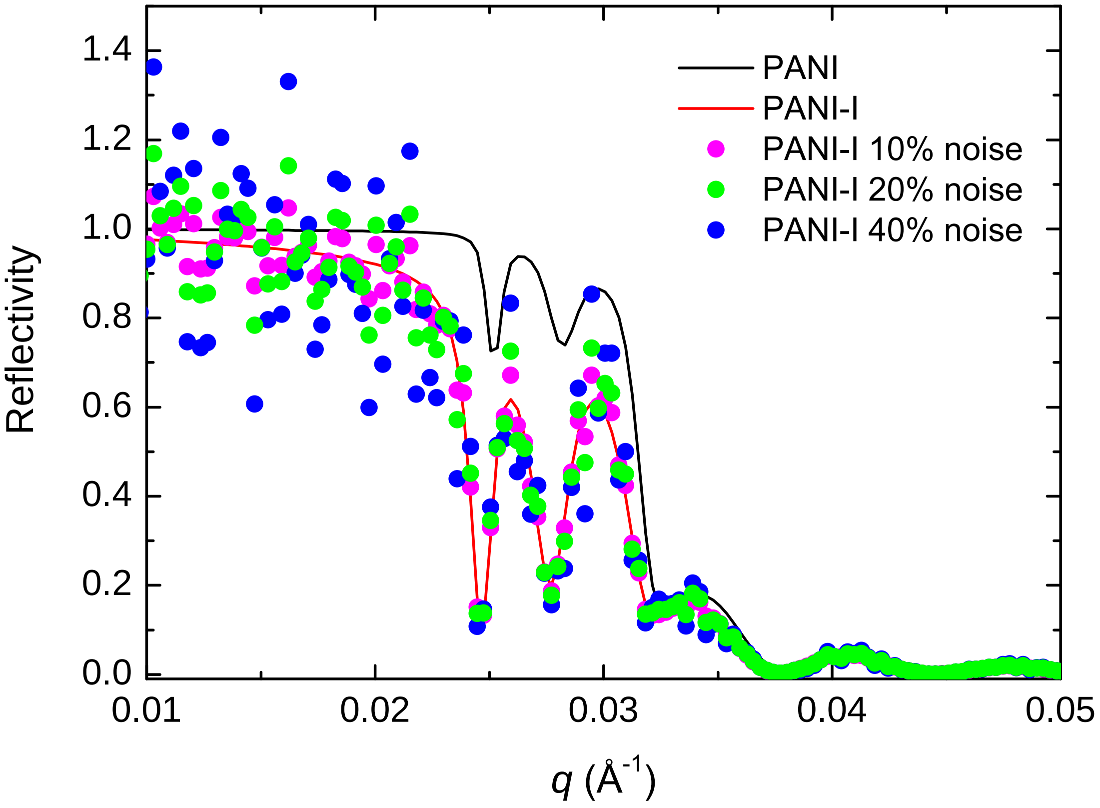

Figure 4.24: Simulated reflectivity for a 750 Å thick polyaniline film, with and without iodine, and with and without added gaussian noise

various levels of added gaussian noise. The very large impact of the iodine-doping on the reflectivity is clearly visible in the angular range between the critical angle of the film and that of the substrate. This facilitates the determination of the imaginary component of the electron density, and thus the iodine concentration via Eq. 4.24, even in the presence of severe noise. Noiselevels up to 40% were added, but the final iodine concentration never deviated more than 5% from the nominal one. For the highest noiselevels it was necessary to use a genetic algorithm for minimizing the cost function, especially when all film parameters were optimized at once. The starting parameters for the optimization were taken as those for the Si-substrate and with a thickness value deviating up to 5% from its nominal value.

The second example concerns the intermixing of Si and Ge inside a film, *e.g.* at the interfaces of a Si/Ge/Si/Ge multilayer. We suppose for simplicity that there is a single homogeneous layer with nominal concentration $Si_{0.4}Ge_{0.6}$. The fits were performed on data calculated from the nominal values (200 Å $Si_{0.4}Ge_{0.6}$ on Si with 2 Å surface roughness and 5 Å interfacial roughness) with and without different percentages of gaussian noise added. The starting points were

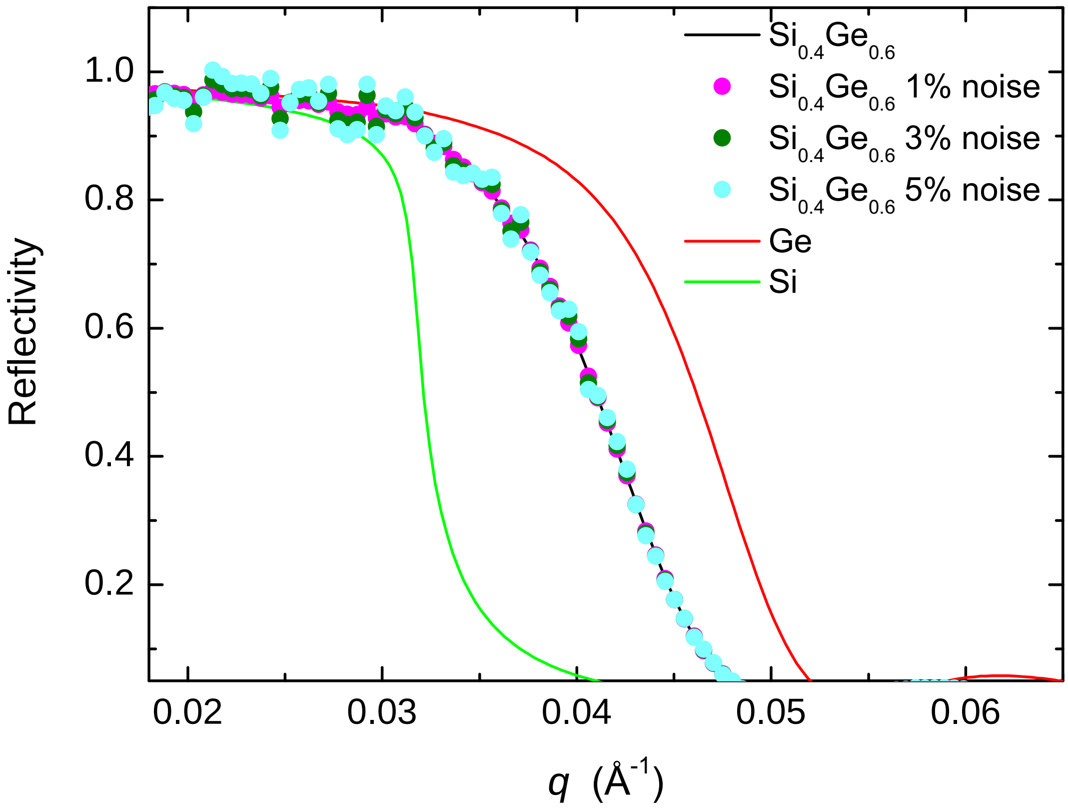

Figure 4.25: Simulated reflectivity for a 200 Å thick $Si_{0.4}Ge_{0.6}$ film, with without added gaussian noise. The curves of Si and Ge films have been added for reference.

either pure Si or pure Ge ($\rho_{\mathrm{e}} = 0.71 + 0.017i$ and $1.37 + 0.039i$ (eÅ^{-3}), respectively). The values of c_{Ge} (with respect to $c_{\mathrm{Si}} = 0.4$) obtained for noise percentages of 0, 1, 3, and 5% are 0.60, 0.54, 0.43, and 0.35, respectively. Inspection of Fig. 4.25 shows that the shape of the reflectivity curve for pure Si, $Si_{0.4}Ge_{0.6}$, and pure Ge hardly changes, except for a lateral shift due to the enhanced electron density, inhibiting an accurate determination of ρ''_{e}.

Note that a better result could have been obtained by application of Vegard's law using only ρ'_{e} and the known values of ρ'_{e}(Si) and ρ'_{e}(Ge) in the crystalline state [136]. The present method (Eq. 4.24) is, however, more general, and can also be applied in cases where Vegard's law is broken or simply not applicable.

The methodology proposed in this report is at its best when the effects of photoabsorption in the thin layer are at maximum, *i.e.* when the X-rays penetrate into the thin film, but are not yet absorbed in the substrate. These conditions are met when the electron density of the thin film ($\rho'_{\mathrm{e},f}$) is lower than that of the substrate ($\rho'_{\mathrm{e},s}$), and the scatterer Z a rather heavy element. An accurate determination of ρ''_{e} is then possible and consequently of the atomic proportion c_{Z}.

When $\rho'_{\mathrm{e},f} > \rho'_{\mathrm{e},s}$ the effect on the reflectivity is much less, and unless the accuracy of the data is very good a reliable estimation of c_{Z} is not possible. Evidently, from Eq. 4.24, if $2\lambda\rho''_{\mathrm{e}} r_0 N_{\mathrm{A}} Z_Z^{\mathrm{eff}} \rightarrow \rho'_{\mathrm{e}} A_Z \mu_{\mathrm{m},Z}$ then $c_Z \rightarrow \infty$, thus for large c_Z the determination becomes rapidly less accurate, which is in line with the observation that $\rho'_{\mathrm{e},f} < \rho'_{\mathrm{e},s}$ and Z not a light element.

Potential applications of the method involve the non-destructive weight percentage determination of metal nanoparticles in thin polymer films. Polyaniline is effectively one of the most frequently used polymeric matrices for dispersing metal particles, since it offers uniformity, adherence and chemical stability, but other polymers can also be employed to embed metal particles of different nature and size.

Another technique that can be used to determine the weight percentage of metal nanoparticles is X-ray fluorescence; the main disadvantage of this method is that a careful calibration using standards is required for reliable quantitative estimation, which is not necessary in the case of X-ray reflectometry since in that case the elemental physical properties of the metals are used. Another way to determine the metal weight percentage is to burn softly the polymer matrix so that only the metal residue remains. The obvious drawback of the latter method is that it is destructive. The accurate alignment of the goniometer seems to be the main obstacle in X-ray reflectometry, as well as the appropriate data reduction procedure [91]. The proper normalization of the scattered photon flux against the incoming flux is evidently crucial for a reliable estimation, and it seems at the same time benificial to reduce at most the beam footprint on the sample, *e.g.* with a knife edge, since that will give a proper plateau of total external reflection before the onset of the critical angle of the film.

It is noted that the method proposed in this report only applies to X-ray reflectometry, since the absorption of neutrons is mostly negliable compared to that of X-rays. Other methods making use of isotopic labelling and/or polarized neutrons exist in neutron reflectometry for extracting chemical sensitive information [137, 138].

In summary we propose an alternative method for the selective determination of the proportion of chemical elements in thin films which is based on the photoabsorption of grazing incidence X-rays in the vicinity of the critical angle(s) of total external reflection. The method only works conveniently for films with a lower electron density than that of substrate. Since the data need only to be collected up to approximately three times the critical angle of total external reflection, the total measurement time is, using standard laboratory equipement, in the order of several minutes.

Bibliography

No comprehensive text books on reflectivity exist that cover both the theory and the experimental side. There are, however, several review papers that treat very well the fundamentals of specular reflectivity. Especially the references [2] and [5] could serve as thorough introductions to the topic. Much of the theory in this reader is based on this work. Many experimental cases are treated by Ref. [7]. X-ray physics is very well treated in [10]. The numbers after the citation refer to the page number in this document where the reference was cited.

[1] Penfold J., Physica B **173** (1991) 1. 10

[2] Als-Nielsen J., Jacquemin D., Kjaer K., Leveiller F., Lahav M., and Leiserowitz L., Phys. Rep. **246** (1994) 251. 111

[3] Hamley I. W. and Pedersen J. S., J. Appl. Crystallogr. **27** (1994) 29. 26

[4] Pedersen J. S. and Hamley I. W., J. Appl. Crystallogr. **27** (1994) 36. 52, 80

[5] Zhou X.L. and Chen S. H., Phys. Rep. **257** (1995) 223. 21, 66, 78, 111

[6] Lu J. R., Lee E. M., and Thomas R. K., Acta Cryst. A **52** (1996) 11. 66, 78, 85

[7] Chason E. and Mayer T.M., Crit. Rev. Sol. State and Mat. Sci. **22** (1997) 1. 111

[8] Tolan M. and Press W., Z. Kristallogr **13** (1998) 213.

[9] Lovell M. R. and Robertson R.M, Curr. Opin. Colloid Interface Sci.. **4** (1999) 197. 78

[10] Als-Nielsen, J. & McMorrow, D. (2001). Elements of Modern X-ray Physics, Wiley & Sons Ltd, Chichester. 10, 66, 111

[11] Parratt L. G., Phys. Rev. **95** (1954) 359. 22, 77, 78

[12] Sears V. F., Phys. Rev. B **48** (1993) 17477. 27, 82

[13] De Haan V. O., van Well A. A., Adenwalla S., and Felcher G. P., Phys. Rev. B. **52** (1995) 10831. 29

[14] Majkrzak C. F. and Berk N. F., Phys. Rev. B **52** (1995) 10827.

[15] Kasper J., Leeb H., and Lipperheide R., Phys. Rev. Lett. (1998) 2614.

[16] Aktosun T. and Sacks P. E., Appl. Math. Rep. No. AM99-03, Iowa State University (1999). 29

[17] Sinha S. K., Sirota E. B., Garoff S., and Stanley H. B., Phys. Rev. B **38** (1988) 2297. 30, 40, 41

[18] Sinha S. K., J. Phys. III France **3** (1994) 1543. 30

[19] Kiessig H., Ann. Phys. **10** (1931) 769. 36

[20] Gibaud A., Vignaud G., and Sinha S. K., Acta Cryst. A **49** (1993) 642. 37, 66, 72, 73, 74

[21] Bouwman W. and Pedersen J. S., J. Appl. Crystallogr. **29** (1996) 152. 37, 74

[22] Wu W.-L., Wallace W. E., Lin E. K., Lynn G. W., Glinka Ch. J., Todd Ryan E., and Ho H.-M., J. Appl. Phys. **87** (2000) 1193. 38

[23] Névot L. and Croce P., Rev. Phys. Appl. **15** (1980) 761. 40

[24] Palasantzas G. and Krim J., Phys. Rev. B **48** (1993) 2873. 41

[25] Filies O., Böling, Grewer K., Lekki J., Lekka M., Stachura Z., and Cleff B., Appl. Surf. Sci. **141** (1999) 357. 41

[26] Hink W. and Petzold W., Z. Angew. Phys. **10** (1958) 135. 48

[27] Segmüller A., Thin Solid Films **18** (1973) 287. 48

[28] M. Li, M. O. Möller, and G. Landwehr, J. Appl. Phys. **80** (1996) 2788. 51, 80

[29] Sanyal M. K., Hazra S., Basu J. K., and Datta A., Phys. Rev. B **58** (1998), 4258. 80

[30] Banerjee S., Raghavan G., and Sanyal M.K., J. Appl. Phys. **85** (1999) 7135. 51

[31] Berk N. F. and Majkrzak C. F., Phys. Rev. B **51** (1995) 11296. 52, 80

[32] Sanyal M. K., Basu J. K., Datta A., and Banerjee S., Europhys. Lett. **36** (1996) 265. 52, 81, 83, 84

[33] Aktosun T. and Sacks P., SIAM J. Appl. Math. **60** (2000) 1340. 53

[34] Aktosun T. and Sacks P., Inverse Problems **16** (2000) 821. 53

[35] Sacks P. E., Wave Motion **18** (1993) 21. 53, 84

[36] Lipperheide R., Reiss G., Leeb H., Fiedeldey H., and Sofianos S. A., Phys. Rev. B **51** (1995) 11032. 53

[37] Majkrzak C. F., Berk N. F., Duna J., Satija S. K., Karim A., Pedulla J., and Deslattes R. D., Physica B (Utrecht) **241-243** (1998) 1101. 53, 65, 85

[38] Schreyer A., Majkrzak C. F., Berk N. F., Grüll H., and Han C. C., preprint, J. Chem. Phys. Sol. (1999). 53, 65

[39] Majkrzak C. F. and Berk N. F., Phys. Rev. B **58** (1998) 15416. 53, 85

[40] Sanyal M. K., Sinha S. K., Gibaud A. , Huang K. G., Carvalho B. L., Rafailovich M., Sokolov J., Zhao X., and Zhao W., Europhys. Lett. **21** (1993) 691. 53, 85

[41] Lee D. R., Park Y. J., Park S. H., Jeong Y. H., Lee, K.-B., Ishimatsu N., Hashizume H., and Hosoito N., Physica B **248** (1998) 146. 53, 54

[42] Proceedings of SXNS-4, Physica B **221** (1996); Proceedings of SXNS-5, Physica B **248** (1998); Proceedings of SXNS-6, Physica B, to be published (2000). 57

[43] Penfold J., Staples E. J., Tucker I., and Thompson L.J., Langmuir **13** (1997) 6638. 57

[44] Penfold J., Staples E. J., Tucker I., Thompson L.J., and Thomas R. K., Physica B **248** (1998) 223. 57

[45] Fragneto G., Thomas R. K., Rennie, A. R., and Penfold J., Science **267** (1995) 657. 57

[46] Vignaud G., Gibaud A., Grübel, Joly A., Ausseré, Legrand J. F., and Gallot Y., Physica B **248** (1998) 250. 57

[47] Russell T. P., Physica B **221** (1996), 267. 57

[48] Edwards K. A., Howes P. B., Macdonald J. E., Hibma T., Bootsma T., James M. A., Physica B **221** (1996) 201. 57

[49] Heslinga D. R., Weitering H. H., Van der Werf D. P., Klapwijk T. M., and Hibma T., Phys. Rev. Lett. (1990) 1589. 57

[50] Lee C.-H., Lee H.-Y., Liang K. S., and Wu T. B., Physica B **248** (1998) 109. 58

[51] Findeisen E., Feidenhans'l R., Vigild M. E., Clausen K. N., Hansen Bindslev J., Bentzon M. D., and Goff J. P., J. Appl. Phys. **76** (1994) 4636.

[52] Van der Lee A., Durand J., Cot D., and Vázquez L., J. Phys. IV France **9** (1999) 157. 58

[53] Munkholm A., Brennan S., and Carr E. C., J. Appl. Phys. **82** (1997) 2944. 59

[54] Kellerman B. K., Chason E., Adams D. P., Mayer T. M., and White J. M., Surf. Sci. **375** (1997) 331. 60

[55] Vallée C., Goullet A., Granier A., Van der Lee A., Durand J., and Marlière C., accepted for publication in J. Non-Crystalline Sol. (2000). 60, 62

[56] Roualdes S., Hovnanian N., Van der Lee A., Sanchez J., and Durand J., J. Phys. IV France **9** (1999) 1147. 62

[57] Klibanov M. V. and Sacks P. E., J. Math. Phys. **33** (1992) 3813. 62, 84

[58] Clinton W. L. , Phys. Rev. B **48** (1993) 1.

[59] Van der Lee A., Eur. Phys. J. B **13** (2000) 755. 84

[60] Van der Lee A., Physica B **283** (2000) 273. 62

[61] Sun Y., Miyatso T., Wigmore J. K., Sonoda N., and Watani Y., J. Appl. Phys. **82** (1996) 152. 64

[62] Daillant, J. & Gibaud, A. (eds.) (1999). X-ray and Neutron reflectivity: Principles and Applications, Springer. 65

[63] Giacovazzo, G. (ed.) (1994). Fundamentals of Crystallography, IUCr, Oxford University Press. 66

[64] Bish, D. L. & Post, J. E. (eds.) (1989). Modern Powder Diffraction, Min. Soc. Am. 66

[65] Hill R. J. (1995). in: The Rietveld Method, Ed. R. A. Young, IUCr, Oxford University Press, 61-101. 66

[66] Lehmann, M. S., Christensen, A. N., Fjellväg, H., Feidenhansl, R., and Nielsen, M. (1987). *J. Appl. Phys.* **20**, 123-129. 66

[67] Will, G., Bellotto, M., Parrish, W., and Hart, M. (1988). *J. Appl. Phys.* **2**, 394-401. 67

[68] Daillant, J. & Alba, M. (2000). *Rep. Prog. Phys.* **63**, 1725-1777. 67

[69] Stettner, J., Schwalowsky, L., Seeck, O. H., Tolan, M., Press W., Schwarz, C. & Von Känel, H. (1996), *Phys. Rev.* B**53**, 1398-1412. 70

[70] Baulès, P. (2006), SimuRX: software for reduction and fitting of reflectivity data, CEMES, Toulouse 71

[71] Van der Lee, A. (1997). Local data reduction program, non-published. 73, 84

[72] De Boor, C. (1977). *SIAM J. Numerical Analysis* **14**, 441-472. 74

[73] De Boor, C. (1979). A Practical Guide to Splines, Applied Mathematics Series **27**, Springer 74

[74] Amos, D. E. (1980), module DBINTK from package CMLIB http://gams.nist.gov/

[75] Van der Lee, A. (2000). *Eur. Phys. J.* B **13**, 755-763. 74

[76] Tikhonov A. & Arsénine, V. (1976). Méthodes de résolution de problèmes mal posés. MIR, Moscou. 74, 84, 92

[77] Richardson, W. H. (1972). *J. Opt. Soc. Am.* **62**, 55-63. 74

[78] Lucy, L. B. (1974). *Astron. J.* **79**, 745-753. 74

[79] Diffrac^{plus}, version 2.0, release 2000: EditDQL, version 2.4, Bruker AXS, GmbH, 1994-1999. 74

[80] Bridou, F. (1994). *J. Phys. III France* **4**, 1513-1522. 74

[81] Hall, S. and McMahon, B. (2005). Acta Cryst. A61, C132. 74

[82] Van der Lee, A. & Brown, I. D. (2006). *J. Appl. Cryst.* **39**, 468. 76

[83] Abelès, F. (1950), *Annales de Physique* **5**, 596-640. 76

[84] Klibanov, M. V., Sacks, P. & Tikhonravov, A. V. (1995). *Inverse Problems* **11**, 1-28. 77, 78

[85] Van der Lee, A. (2002). *J. Phys. IV France* **12**, Pr6/255-Pr6/263. 78

[86] Born, M. & Wolf, E. (1980). Principles of Optics, Pergamon, London, 6th Ed. 78

[87] Braun, C. (1997). Parrat32 program for reflectivity analysis, version 1.5, HMI Berlin. 78

[88] Ober, R. (2001). *Firefx4c* program for multislice reflectivity analysis; *Wfiref3h* program for classical reflectivity analysis, Académie de France. 78, 86, 104

[89] Windt, D. L. (1998). *Comput. Phys.* **12**, 360-370. 78, 80, 86, 92

[90] Windt. D. L. (2005). IMD4.1 fit program: http://www.rxollc.com/idl/. 78, 86

[91] Salah, F., Harzallah, B. & Van der Lee, A. (2007). *J. Appl. Cryst.* **40**, 813-819. 78, 86

[92] Dane, A. D., Veldhuis, A., De Boer, D. K. G., Leenaers, A. J. G. & Buidens, L. M. C. (1998). *Physica* B**253**, 254-268. 79, 87, 103, 108

[93] Ulyanenkov, A., Omote, K. & Harade, J. (2000). *Physica* B**283**, 237-241. 79

[94] Politsch E. (2001). *J. Appl. Cryst.* **34**, 239-251.

[95] Šimek, D., Rafaja, D. & Kub, J. (2001). *Mat. Struct.* **8**, 16-21.

[96] Kunz, K., Reiter, J., Götzelmann & Stamm, M. (1993). *Macromolecules* **26**, 4316-4323. 79

[97] Luokkala, B. B., Garoff, S. & Suter, R. M. (2000). *Phys. Rev.* E**62**, 2405-2415. 79

[98] Laub, C. F. & Kuhl, T. L. (2006). *J. Chem. Phys.* **125**, 244702/1-8.

[99] Arfken, G. (1970). Mathematical methods for physicists, Academic Press, Inc, New York. 79

[100] Glatter, O. (1977). *J. Appl. Cryst.* **10**, 415-422. 80

[101] Makowski, L. (1981). *J. Appl. Crystallogr.* **14**, 160-168. 80

[102] Skita, V. , Filipkowski, M., Garito, A. F. & Blasie, J. K. (1986). *Phys. Rev. B* **34**, 5826-5837. 80

[103] Zimmermann, K.-M., Tolan, M., Weber, R., Stettner, J., Doerr, A. K. & Press, W. (2000). *Phys. Rev. B* **62**, 10377-10382. 80

[104] Bengu, E., Salud, M. & Marks, L. D. (2001). *Phys. Rev. B* **63**, 195414-1,6. 80

[105] Oszlányi, G. & Süto, A. (2004). *Acta Crystallogr.* A**60**, 134-141. 80, 81

[106] Van der Lee, A. (2001). *Langmuir* **17**, 7664-7669. 80

[107] Banerjee, S., Gibaud, A., Chateigner, D., Ferrari, S. & Fanciulli, M. (2002). *J. Appl. Phys.* **91**, 540-542. 84, 103

[108] Van der Lee, A., Durand, J., Blin, D., Holliger, P. & Martin, F. (2004). *Eur. Phys. J.* B**39**, 273-277.

[109] Banerjee, S., Ferrari, S., Piagge, R. & Spandoni S. (2004). *Appl. Phys. Lett.* **84**, 3798-3800.

[110] Lutterotti, L. (2007). *Maud* - Materials Analysis Using Diffraction. (http://www.ing.unitn.it/m̃aud/) 84

[111] Smigiel, E. & Cornet, A. (2000). *J. Phys. D: Appl. Phys.* **33** 1757-1763. 84, 86

[112] Prudnikov, I. R., Deslattes, R. D. & Matyi, R. D. (2001). *J. Appl. Phys.* **90**, 3338-3346. 84

[113] Berk, N. F. & Majkrzak, C. F. (2003). *Langmuir* **19**, 7811-7817. 84

[114] Chadan, K. & Sabatier, P. (1989). Inverse Problems in Quantum Scattering Theory, Springer-Verlag, New York. 84

[115] Van der Lee, A. (1999). *LDR*: program for *ab-initio* phasing and inverting of reflectivity data, Montpellier. 84

[116] Berk, N. F. & Majkrzak, C. F. (1996). *J. Phys. Soc. Jpn* **65**, Suppl. A, 107-112. 85, 93

[117] Majkrzak, C. F. & Berk, N. F. (1996). *Physica* B **221**, 520-523. 85

[118] Leeb, H., Kasper, J. & Lipperheide R. (1998). *Phys. Lett.* A **239**, 147-152. 85

[119] Majkrzak, C. F., Berk, N. F., Krueger, S., Dura, J. A., Tarek, M., Tobias, D., Silin, V., Meuse, C. W., Woodward, J. & Plant, A. L. (2000). *Biophys J.* **79**, 3330-3340. 85

[120] Perez-Salas, U. A., Faucher, K. M. , Majkrzak, C. F., Berk, N. F., Krueger, S. & Chaikof, E. L. (2003). *Langmuir* **19**, 7688-7694. 85

[121] Aktosun, T. & Sacks, P. E., (1998). *Inverse Problems* **14**, 211-224. 85

[122] Aktosun, T. & Sacks, P. E., (2000). *Inverse Problems* **16**, 821-838. 85

[123] Banerjee, S., Park, Y. J., Lee, D. R., Jeong, Y. H., Lee, K.-B, Yoon, S. B., Choi, H. M., Park, J.-C, Roh, J. S. & Sanyal, M. K. (1998). *Appl. Surf. Sci.*, 41-45. 85

[124] Vaknin, D., Krüger, P. & Lösche, M. (2003). *Phys. Rev. Lett.* **90**, 178102-1/4. 85, 102

[125] Vaknin, D., Als-Nielsen, J, Piepenstock, M. & Lösche M. (1991). *Biophys. J.* **60**, 1545-1552. 85, 102

[126] Colombi, P., Agnihotri, D. K., Asadchikov, V. E., Bontempi, E., Bowen, D. K., Chang, C.-H, Depero, L. E., Farnworth, M., Fujimoto, T., Gibaud, A., Jergel, M., Krumrey, M., Lafford, T. A., Lamperti, A., Ma, T., Matyi, R. J., Meduna, M., Milita, S., Sakurai, K., Shabel'nikov, L., Ulyanenkov, A., Van der Lee, A. & Wiemer, C., *J. Appl. Cryst.* **40**, 143-152. 85

[127] Bruker AXS, INC (2005). *LEPTOS*, Analytical software for HRXRD, XRR, XRDS, and GISAXS, Madison, USA. 86

[128] Nelson, A. (2006), *J. Appl. Cryst.* **39**, 273-276. 86

[129] NIST (2007), Scattering Length Density Calculator, NIST Center for Neutron Research, http://www.ncnr.nist.gov/resources/sldcalc.html. 86, 104

[130] Press, W., Flannery, B., Teukolsky, S., & Vetterling, W. (1986). Numerical Recipes, Cambridge Univ Press, Cambridge. 87

[131] Martel, L., Johnson, C., Boutet, S., Al-Kurdi, R., Konovalov, O., Robinson, I. & Legrand, J.-F. (2002). *J. Phys.* IV **12**, 365-378. 86

[132] Bowen, D. K. & Deslattes, R. D. (2001). In: CP550. *Characterization and Metrology for ULSI Technology: 2000 International Conference*. Eds. Seiler, D. G. Diebold, A. C., Shaffner, T. J., McDonald, R., Bullis, W. M., Smith, P. J. & Secula, E. M., AIP, 570-579. 92

[133] Creagh, D. C., and McAuley, W. J., X-ray dispersion corrections (Kluwer, International Union of Crystallography, Chester, UK, 1995), vol. C: Mathematical, physical and chemical tables of International Tables for Crystallography, chap. 4.2.6 99

[134] Park, C., Fenter, P. A., Sturchio, N. C., and Regalbuto, J. R., *Phys. Rev. Lett.* **94**, 076104 (2005). 102

[135] Airoudj, A., Debarnot, D., Beche, B., and Poncin-Epaillard, F., *Anal. Chim. Acta* **626**, 44 (2008). 102

[136] Banerjee, S., Sanyal, M. K., Datta, A., Kanakaraju, S., and S. Mohan, *Phys. Rev. B* **54**, 16377 (1996). 103

[137] Marsh, R. J., Jones, R. A. L., Sferrazza, M., and Penfold, J., *J. Coll. Interface Sci.* **218**, 347 (1999). 107

[138] Grüll, H., Schreyer, A., Berk, N. F., Majkrzak, C. F., and Han, C. C., *Europhys. Lett.* **50**, 107 (2000). 108

Glossary of symbols

The following gives a glossary of symbols, followed by their definition, sometimes in terms of other sumbols, and finally the most commonly used unities in which the quantity represented by the symbol is expressed (if appropriate) within square brackets. 108

$\psi(k,z)$	wave function
λ	wavelength of incident beam [nm]
θ	angle of incidence, *i.e.*, angle between incident beam and surface
θ_{c}, k_{c}	critical angle (wave number) of total reflection
k_0	amplitude of the incident wave vector ($= 2\pi/\lambda$) [nm^{-1}]
k	the wave number, *i.e.*, the vertical component of the k-vector ($= k_0 \sin\theta$) [nm^{-1}]
q	momentum transfer of the reflectivity process ($q = 2k = 4\pi \sin\theta/\lambda$) [nm^{-1}]
z	coordinate perpendicular to the surface of the material [nm]
$V(z)$	scattering potential [nm^{-2}]
$n(z)$	complex refractive index ($n(z) = 1.0 - \delta + i\beta$)
ϵ	complex dielectric constant ($\epsilon = \epsilon' + i\epsilon'' = 1.0 - 2\delta + 2i\beta$)
r_0	Thomson scattering length of the electron ($= 2.82 \times 10^{-6}$ nm)
ρ_{n}	number density: number of atoms per unit volume [nm^{-3}]
ρ_{e}	electron number density: number of electrons per unit volume [nm^{-3}]
ρ_{m}	mass density [gcm^{-3}]
ρ	scattering length density [nm^{-2}]
Z	atomic number
A	atomic mass [g per N_{A} atoms]
N_{A}	number of Avogadro ($= 6.02205 \times 10^{23}$ mol^{-1})
f'	real part of the dispersion correction to Z
f''	imaginary part of the dispersion correction to Z
i	imaginary number: i=$\sqrt{-1}$ (in mathematical formula's)
σ_{pe}	atomic photoabsorption cross section [barns/atom; 1 barn = 10^{-24}cm^{-2}]
μ_{m}	mass absorption coefficient [cm^{2}g^{-1}]
μ_{l}	linear absorption coefficient: $\mu_{\mathrm{l}} = \rho_{\mathrm{n}} \sum c_j \sigma_{\mathrm{pe},j} = \rho_{\mathrm{m}} \sum c_j A_j \mu_{\mathrm{m},j} / \sum c_j A_j$ [cm^{-1}]
b	neutron scattering length [cm]
Λ	penetration depth [nm]

R	reflectance or reflection coefficient
T	transmittance or transmission coefficient
r	reflectivity $r = \|R\|^2$
F	structure factor
$\mathcal{F}$	Fourier transform operator
σ	roughness parameter [nm]
σ_v	gaussian width of instrumental profile function
σ_λ	gaussian width due to wavelength distribution
σ_c	gaussian width due to collimation effects
σ_pe	atomic photoabsorption cross section
d	layer thickness [nm]

Index